



MODELING AND PARAMETER ESTIMATION IN FLEXIBLE RISER-BEND
STIFFENER TOP CONNECTION

Yangye He

Tese de Doutorado apresentada ao Programa de Pós-graduação em Engenharia Oceânica, COPPE, da Universidade Federal do Rio de Janeiro, como parte dos requisitos necessários à obtenção do título de Doutor em Engenharia Oceânica.

Orientadores: Murilo Augusto Vaz
Marcelo Caire

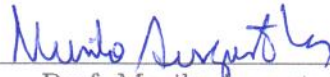
Rio de Janeiro
Outubro de 2019

MODELING AND PARAMETER ESTIMATION IN FLEXIBLE RISER-BEND
STIFFENER TOP CONNECTION

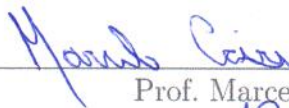
Yangye He

TESE SUBMETIDA AO CORPO DOCENTE DO INSTITUTO ALBERTO LUIZ
COIMBRA DE PÓS-GRADUAÇÃO E PESQUISA DE ENGENHARIA (COPPE)
DA UNIVERSIDADE FEDERAL DO RIO DE JANEIRO COMO PARTE DOS
REQUISITOS NECESSÁRIOS PARA A OBTENÇÃO DO GRAU DE DOUTOR
EM CIÊNCIAS EM ENGENHARIA OCEÂNICA.

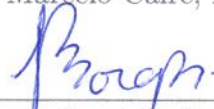
Examinada por:



Prof. Murilo Augusto Vaz, Ph.D.



Prof. Marcelo Caire, D.Sc



Prof.^a Lavinia Maria Sanabio Alves Borges, D.Sc.



Prof. Ney Roitman, D.Sc.



Prof. Clóvis de Arruda Martins, D.Sc.

RIO DE JANEIRO, RJ – BRASIL
OUTUBRO DE 2019

He, Yangye

Modeling and parameter estimation in flexible riser-bend stiffener top connection/Yangye He. – Rio de Janeiro: UFRJ/COPPE, 2019.

XVI, 96 p.: il.; 29, 7cm.

Orientadores: Murilo Augusto Vaz

Marcelo Caire

Tese (doutorado) – UFRJ/COPPE/Programa de Engenharia Oceânica, 2019.

Referências Bibliográficas: p. 89 – 96.

1. Conexão de topo de riser. 2. Enrijecedor à flexão. 3. Distribuição de curvatura. 4. Estimativa de parâmetros. 5. Teste de flexão. 6. Medições baseadas em imagem. I. Vaz, Murilo Augusto *et al.* II. Universidade Federal do Rio de Janeiro, COPPE, Programa de Engenharia Oceânica. III. Título.

*Seeking truth from facts.
To my family*

Agradecimentos

Thank Prof. Murilo Augusto Vaz for the guidance of my doctoral course and research, frequently meetings and inspirations in my research topic, cooperations of journal and conference paper publications, and opportunities in the Shell-Brazil project workshops in Brazil and Norway. Thank Prof. Marcelo Caire for the technical guidance and supporting, and rigorous manner in our publications and project reports. Thanks for David Hernandez's help in the ocean structure laboratory (NEO) in UFRJ.

Acknowledge financial supports of my doctoral study in COPPE/UFRJ by Coordination for the Improvement of Higher Education Personnel (CAPES), National Council of Scientific and Technological Development (CNPq), and Brazilian Industrial Research and Innovation Company (EMBRAPPII).

I would also like to thank Prof. Duan Menglan, Prof. An Chen (CUPB) and Prof. Su Jian for the suggestions and encouragements of my doctoral study. I appreciate Prof. Fu Guangming and Dr. Duan Qingfeng picked me up in the airport when I arrived in Rio and the following help during doctoral studies.

Thanks for my colleagues' accompany in NEO, Liu Junpeng, Li Xiaotian, Lu Hailong, Wei Rongzhi, Victor, Miguel, Aynor et al. Thanks for the Chinese students' four years accompany in COPPE/UFRJ, Liu Bingqi, Yi Huanggao, Gu Jian, Yang Jiankun, Wang Yuxi, Cheng Huarong et al.

I am grateful to my friends in UFRJ, Juliana, Antonio, Andreza, Juana, Nathalia, Nicolle, Thais, Clarissa and Edmilson, for warmly and friendly teaching me Portuguese, Brazilian culture and Bible.

Thanks my parents and sister for the continued love, encouragements and strong support all the time.

Resumo da Tese apresentada à COPPE/UFRJ como parte dos requisitos necessários para a obtenção do grau de Doutor em Ciências (D.Sc.)

MODELAGEM E ESTIMATIVA DE PARÂMETROS DA CONEXÃO DE TOPO DE RISER FLEXÍVEL/ENRIJECEDOR À FLEXÃO

Yangye He

Outubro/2019

Orientadores: Murilo Augusto Vaz

Marcelo Caire

Programa: Engenharia Oceânica

A conexão de topo do riser flexível é uma região crítica para a (re) avaliação de vida à fadiga devido à grande variação de tração/curvatura e incertezas de modelagem. O efeito do enrijecedor à flexão na distribuição de curvatura traz incertezas inerentes. Neste trabalho, um modelo de flexão de viga de grandes deslocamentos é desenvolvido para representar a conexão de topo do riser com enrijecedor à flexão e com interface de I-tube considerando os comportamentos de flexão não linear do riser e enrijecedor à flexão sujeito a uma tração de topo com um ângulo de rotação. A formulação matemática correspondente, com condições de contorno em múltiplos pontos, é numericamente resolvida por um procedimento iterativo em Mathematica. Resposta da deflexão do sistema riser/enrijecedor e avaliações paramétricas do comprimento do I-tube e do raio de curvatura da luva são analisadas em um estudo de caso, incluindo a curvatura da extremidade final e forças de contato do riser com enrijecedor à flexão e luva. Uma abordagem proposta de monitoramento composta por girômetros instalados ao longo do comprimento do riser/enrijecedor à flexão combinado com o algoritmo de Levenberg-Marquardt (L-M), é numericamente investigada para estimar a tração efetiva desconhecida e a resposta elástica do poliuretano no sistema riser com enrijecedor à flexão. Uma investigação preliminar de viabilidade é implementada em um estudo de caso com os dados de girômetros numericamente gerados pelas simulações de Monte Carlo. O número e localizações de sensores, condições de carga e modelo de topo podem influenciar significativamente as estimativas. Além disso, um teste de flexão em real escala do riser/enrijecedor à flexão utilizando medições baseadas em imagem é apresentado com alguns parâmetros desconhecidos. A análise inversa, usando o algoritmo L-M, é empregada no sistema de teste de flexão com um modelo direto de elementos finitos e medições de configuração para estimar os parâmetros de tração e de material de poliuretano, o que indica que a abordagem proposta é confiável para estimar os parâmetros na conexão da parte topo do riser.

Abstract of Thesis presented to COPPE/UFRJ as a partial fulfillment of the requirements for the degree of Doctor of Science (D.Sc.)

MODELING AND PARAMETER ESTIMATION IN FLEXIBLE RISER-BEND
STIFFENER TOP CONNECTION

Yangye He

October/2019

Advisors: Murilo Augusto Vaz
Marcelo Caire

Department: Ocean Engineering

The flexible riser top connection is a critical region for fatigue lifetime (re)assessment due to large tension/curvature variation and modeling uncertainties. Both the bend stiffener effect on the curvature distribution and top tension time series could be its inherent uncertainties. In this work, a large deflection beam bending model is developed to represent the flexible riser-bend stiffener top connection with I-tube interface, considering the nonlinear bending behaviors of riser and bend stiffener subjected to a top tension with a rotated angle. The corresponding mathematical formulation with multipoint boundary conditions is numerically solved by an iterative procedure in Mathematica. Large deflection response of the top connection and parametric assessments of I-tube length and sleeve curved radius are analyzed in a case study, including the end-fitting curvature and contact forces of riser with bend stiffener and sleeve. A proposed monitoring approach composed by gyrometers installed along the riser/bend stiffener length combined with the Levenberg-Marquardt (L-M) algorithm, is investigated in riser/bend stiffener system to numerically estimate the unknown top tension and polyurethane elastic response. A preliminary feasibility investigation is implemented in a case study with the gyrometer data numerically generated by Monte Carlo simulations. The sensor number and arrangement, loading conditions and direct top connection model may significantly influence the estimations. Furthermore, a full-scale bending-tension test of riser/bend stiffener with the image-based measurements is presented with unknown material response. The inverse analysis using L-M algorithm is employed in the bending-tension test system combined with a direct finite element model and configuration measurements to simultaneously estimate top tension and polyurethane material parameters, which indicates that the proposed approach is reliable for parameter estimation in the riser top connection.

Contents

List of Figures	xi
List of Tables	xv
1 Introduction	1
1.1 Flexible riser-bend stiffener top connection	2
1.1.1 Flexible pipe cross section and end fitting	2
1.1.2 I-tube bellmouth	4
1.1.3 Bend stiffener	4
1.2 Objective and methodology	5
1.3 Organization of the thesis	7
2 Literature Review	9
2.1 Analysis of flexible riser-bend stiffener top connection	9
2.2 Monitoring techniques in the riser top	10
2.3 Inverse problem methodology	12
2.4 Bending test of flexible pipe	13
2.5 Experimental measurements	14
2.6 Summary	14
3 Modeling of Flexible Riser-Bend stiffener Top Connection	16
3.1 Mathematical formulation	16
3.1.1 Geometrical relations	17
3.1.2 Equilibrium of internal forces and moments	18
3.1.3 Constitutive relations and pure bending formulation	19
3.1.4 Governing equations	21
3.1.5 Geometrical compatibility	24
3.1.6 Multipoint boundary conditions	25
3.2 Numerical solution procedure	26
3.3 Case study	28
3.3.1 Large deflection assessment of top connection with I-tube in- terface	30

3.3.2	Sleeve geometry influence	33
3.3.3	I-tube length influence	37
3.4	Conclusions	39
4	Inverse Problem Methodology in Riser/Bend Stiffener System	40
4.1	Direct analytical model of riser/bend stiffener system	40
4.2	Inverse parameter estimation methodology	42
4.2.1	Levenberg-Marquardt (L-M) methodology	42
4.2.2	Computational Algorithm	43
4.3	Case Study	45
4.3.1	Gyrometer data - numerical simulation procedure	46
4.3.2	Inverse method based on linear elastic model	46
4.3.3	Inverse method based on nonlinear elastic model	50
4.4	Conclusions	59
5	Parameter Estimation in Riser/Bend Stiffener System with Optical Measurements	60
5.1	Bending-tension test of riser/bend stiffener with optical measurements	61
5.1.1	Bending-tension test of riser/bend stiffener	61
5.1.2	Optical technique for configuration measurements of riser/bend stiffener	61
5.1.3	Data analysis of optical measurements	65
5.2	Finite element model of riser/bend stiffener test	66
5.2.1	Finite element model	67
5.2.2	Hyperelastic behavior of polyurethane	67
5.2.3	Mesh sensitivity analysis	69
5.3	Inverse problem methodology	70
5.3.1	Levenberg-Marquardt algorithm	70
5.3.2	Inverse analysis for the riser/bend stiffener system	72
5.4	Parameter estimation with optical measurements	74
5.4.1	Estimation of material parameters	74
5.4.2	Estimation of material parameters and top tension	76
5.4.3	Estimation of material parameters and constrained top tension	77
5.4.4	Riser curvature distribution	81
5.5	Conclusions	81
6	Conclusion and Suggestions	84
6.1	Main original contributions	84
6.2	Main conclusions	85
6.3	Suggestions for Future work	88

List of Figures

1.1	Flexible risers supported by the FPSO top mounted turret [1].	2
1.2	Schematic of typical flexible riser cross section [2].	3
1.3	End fitting of an unbounded flexible pipe [2].	3
1.4	Riser-bend stiffener top connection with I-tube interface [3].	4
1.5	A proposed methodology for riser top connection lifetime assessment.	6
1.6	Overview of the organization structures of the thesis.	7
3.1	(a) Riser-bend stiffener top connection system with I-tube interface beam model; (b) Infinitesimal element; (c) Bend stiffener cross-section.	17
3.2	Nonlinear bending moment and curvature relationship of flexible riser.	19
3.3	Nominal stress versus nominal strain for the tensile test and nonlinear elastic model ($E_q=20.19$ MPa and $q=0.4738$).	20
3.4	Schematic of the riser-bend stiffener top connection model: (a) Configuration of the extended riser section in the I-tube area; (b) Contact force of the riser with the sleeve; (c) Configuration of riser/bend stiffener section.	22
3.5	Flowchart of numerical solution procedure for flexible riser-bend stiffener top connection system.	27
3.6	Riser-bend stiffener top connection with I-tube interface system schematic drawing.	29
3.7	Geometry of the riser/bend stiffener section.	29
3.8	Top connection response for loading (450 kN, 10°): (a) Configuration; (b) Angle; (c) Curvature; (d) Bending moment; (e) Shear force and (f) Tension distributions.	31
3.9	Top connection response for loading (1200 kN, 15°): (a) Configuration; (b) Angle; (c) Curvature; (d) Bending moment; (e) Shear force and (f) Tension distributions.	32
3.10	Contact force distribution along riser/sleeve and riser/bend stiffener sections.	33
3.11	Initial contact angle and end-fitting curvature versus curved sleeve radius.	35

3.12	Sleeve geometry influence in the curvature distribution.	36
3.13	I-tube length influence in the curvature distribution ($L_1 = 2, 4, 6, 8$ m).	38
3.14	Initial curvature versus I-tube length (Curved sleeve radius $R_{AB} = 8$ m).	38
4.1	A bend stiffener system with N monitoring points.	41
4.2	Flowchart of Levenberg-Marquardt computational algorithm.	44
4.3	Geometric parameters of the bend stiffener system with nine sensors.	46
4.4	Parameters estimation procedure for the riser/bend stiffener system.	47
4.5	Nominal stress vs. nominal strain of nonlinear elastic model and inverse method calculation envelope (simulated sensor data + linear elastic model) of Young's modulus for two loading conditions ($F = 125, 500$ kN, $\phi_L=10^\circ$).	48
4.6	Angle distribution of nonlinear elastic model and inverse method calculation envelope (simulated sensor data + linear elastic model) for two loading conditions ($F = 125, 500$ kN, $\phi_L=10^\circ$).	48
4.7	Curvature distribution of nonlinear elastic model and inverse method calculation envelope (simulated sensor data + linear elastic model) for two loading conditions ($F = 125, 500$ kN, $\phi_L=10^\circ$).	49
4.8	Maximum strain distribution of nonlinear elastic model and inverse method calculation envelope (simulated sensor data + linear elastic model) for two loading conditions ($F = 125, 500$ kN, $\phi_L=10^\circ$).	49
4.9	Probability distribution of estimated top tension F_e^{NLE} for arrangements A3 and A5.	51
4.10	Probability distribution of material parameter $E_{q,e}^{NLE}$ for arrangements A3 and A5.	52
4.11	Probability distribution of material parameter q_e^{NLE} for arrangements A3 and A5.	52
4.12	Estimated material curve envelope for arrangements A3 and A5.	52
4.13	Top tension influence on the sensitivity coefficients ($\phi_L=10^\circ$).	53
4.14	Angle distribution of nonlinear elastic model, sensors range and inverse method calculation envelope (simulated sensor data + nonlinear elastic model) with 4 sensors (A3) for two loading conditions ($F = 125, 500$ kN, $\phi_L=10^\circ$).	54
4.15	Curvature distribution of nonlinear elastic model and inverse method calculation envelope (simulated sensor data + nonlinear elastic model) with 4 sensors (A3) for two loading conditions ($F = 125, 500$ kN, $\phi_L=10^\circ$).	54

4.16	Tip angle influence ($\phi_L = 2, 4, 10, 20, 30^\circ$) on the sensitivity coefficients ($F = 125$ kN).	55
4.17	Angle distribution of nonlinear elastic model, sensors range and inverse method calculation envelope (simulated sensor data + nonlinear elastic model) with 4 sensors (A3) for two loading conditions ($\phi_L = 2, 30^\circ$, $F = 125$ kN).	56
4.18	Curvature distribution of nonlinear elastic model and inverse method calculation envelope (simulated sensor data + nonlinear elastic model) with 4 sensors (A3) for two loading conditions ($\phi_L = 2, 30^\circ$, $F = 125$ kN).	56
4.19	Tip angle influence on the mean and standard deviation values of the estimated top tension F_e^{NLE} ($F = 125$ kN) with 4 sensors (A3).	57
4.20	Tip angle influence on the mean and standard deviation values of the estimated material parameter $E_{q,e}^{NLE}$ ($F = 125$ kN) with 4 sensors (A3).	57
4.21	Tip angle influence on the mean and standard deviation values of the estimated material parameter q_e^{NLE} ($F = 125$ kN) with 4 sensors (A3).	57
5.1	The vertical rig for the bending-tension test of riser/bend stiffener (NEO, COPPE/UFRJ).	62
5.2	(a) Schematic of optical monitoring device arrangement and (b) region of interest of the bend stiffener camera in the scene.	63
5.3	Image processing for bend stiffener and riser targets.	64
5.4	21 and 17 target measurements on the bend stiffener and riser central axes respectively and mean values of measurements in each position for five tests.	66
5.5	Simplified finite element model for the bending-tension test of the riser/bend stiffener system (Mesh 0.05 m).	68
5.6	Configurations of the FEM models of the riser/bend stiffener with two mesh sizes for loading conditions (a) (1200 kN, 15°) and (b) (1500 kN, 15°).	69
5.7	Flowchart of L-M algorithm for the parameter estimation in the riser/bend stiffener system with optical measurements.	71
5.8	The simulated measurements of 8 targets in the bend stiffener region with 8 noise levels.	73
5.9	Configuration measurements of 8 targets on the bend stiffener central axis and mean values of measurements in each position for five tests.	74
5.10	Nominal strain-stress relations by estimated material parameters for two hyperelastic models of polyurethane.	75

5.11	Final summation of squared residuals of five tests and mean data for three types of parameter estimations.	78
5.12	Estimated error of tension of five tests and mean data for two types of parameter estimations.	78
5.13	Nominal strain-stress relation by estimated material parameters of bend stiffener in the material and constrained tension estimation case.	79
5.14	Configurations of riser and bend stiffener of measurements and FEM model for five tests and mean data.	80
5.15	Curvature distributions of riser and bend stiffener.	81

List of Tables

3.1	Top connection system geometrical and loading parameters	26
3.2	Sleeve radius influence in the top connection response (450 kN, 10°) .	34
3.3	Sleeve radius influence in the top connection response (1200 kN, 15°)	34
3.4	I-tube length influence in the top connection response (450 kN, 10°) .	37
3.5	I-tube length influence in the top connection response (1200 kN, 15°)	37
4.1	The mean and standard deviation values of top tension F_e and Young's modulus E_e estimation by linear material model for two loading cases ($F = 125, 500$ kN, $\phi_L=10^\circ$)	47
4.2	Sensor arrangement definition and sensitivity coefficient matrix ($F =125$ kN, $\phi_L=10^\circ$)	51
4.3	Sensor arrangement effect on the mean and standard deviation values of estimated top tension and material parameters ($F = 125$ kN, $\phi_L=10^\circ$, $E_q =20.19$ MPa and $q=0.4738$)	51
4.4	Top tension influence on the mean and standard deviation values of estimated top tension and material parameters ($\phi_L=10^\circ$) with 4 sensors (A3)	54
4.5	Number of sensors influence - Comparison of top tension and material parameters mean and standard deviation for arrangements A3 and A5 ($\phi_L=2^\circ, 3^\circ, 4^\circ$ and 5° , $F = 125$ kN)	58
4.6	Small tip angle influence on the mean and standard deviation values of estimated top tension with known material parameters ($F = 125$ kN) and 4 sensors (A3)	59
5.1	Optical monitoring system hardware	63
5.2	Rotation angle, tension and internal pressure of riser at the maximum rotation for five tests	66
5.3	Component densities ρ of riser/bend stiffener system	67
5.4	Material coefficients of the hyperelastic models of polyurethane	69
5.5	Mesh sensitivity analysis for the FEM model of the riser/bend stiffener system	69

5.6	The estimated parameters $(F_e, E_{q,e}, q_e)$ of the riser/bend stiffener system for the simulated measurements with 8 noise levels for exact parameters (1200 kN, 15 MPa, 0.7)	73
5.7	The estimated material parameters $(E_{q,e}, q_e)$ of bend stiffener polyurethane	75
5.8	Estimated parameters $(F_e, E_{q,e}, q_e)$ of riser/bend stiffener system . . .	76
5.9	Estimated material parameters and constrained tension $(F_e, E_{q,e}, q_e)$ of riser/bend stiffener system	77

Chapter 1

Introduction

Since early 1970's, the flexible risers have been widely applied in offshore oil fields to connect the floating production systems (FPSO) and subsea facilities, especially in harsh and deep environments. There are more than 3500 dynamic unbounded flexible risers in worldwide operation in 2016 [4], such as offshore Brazil, West Africa, North Sea and Gulf of Mexico oil fields. The flexible pipe can meet field specification: ultra deepwater up to 3000 m, higher temperatures up to 170°C, and higher pressures up to 70 MPa, 90 MPa and 120 MPa respectively for 10", 8" and 6" internal diameters (ID) on dynamic riser applications [5]. Flexible pipes are also used in the shallow and medium water depth compared to the rigid steel flowlines ranging from 2" to 22" ID. In addition, there are applications of flexible flowlines on the seabed and jumpers with a considerable number and kilometers.

A flexible riser is generally made up of several different layers for specific field development requirements. Simple flexible pipes consist only of 4 layers for water transport with medium pressure, while the most complex flexible pipes may have up to 19 layers. The main components are leakproof thermoplastic barriers and corrosion resistant steel wires. The helically wound steel wires give the structure its high pressure resistance and excellent bending characteristics, which provides the flexibility and superior dynamic behavior. For example, a typical 8" ID flexible pipe can be bent safely to a radius of 2 m or less. Flexibility makes it possible to spool the pipe on a reel or in a carousel for the efficient and quick transportation and installation. The average laying speed is commonly 500 m/h as the flexible pipe comes in a continuous length [5]. Flexible pipe has a better corrosion resistance than steel pipe as its steel wires are not in direct contact with the conveyed fluid. Advantages of flexible pipe make it gaining more popularity, including superior dynamic behavior, prefabrication, storage in long lengths on reels, reduced transport and installation costs, and suitability for use with compliant structures.

The riser top connection is a critical area for the dynamic behavior and fatigue life assessments of the flexible risers, which sustains the highest tensions and often

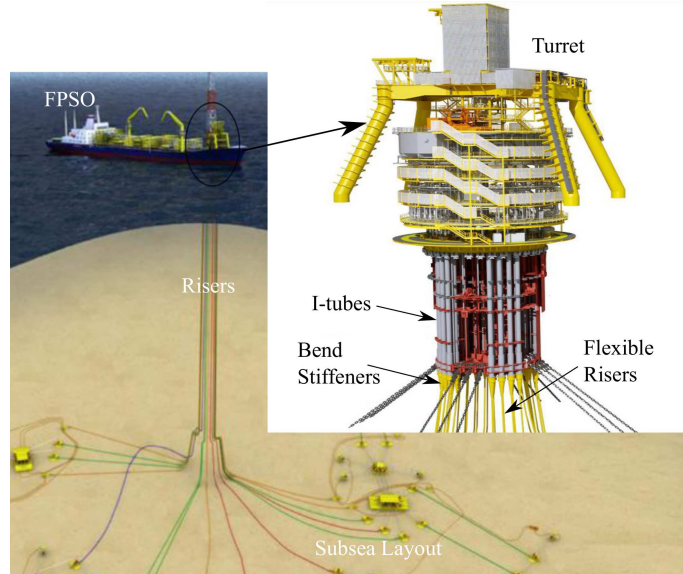


Figure 1.1: Flexible risers supported by the FPSO top mounted turret [1].

the maximum curvatures in the riser system. Bend stiffener, an ancillary polymeric structure with a conical shape, is employed in the top connection to protect flexible riser against excessive bending and accumulative fatigue damage. The riser top connection usually presents two main floating unit interface configurations: i) end-fitting and bend stiffener directly connected to the riser balcony or ii) riser connected to the floating unit in the top end of an I-tube, reducing the end-fitting bending loading, and bend stiffener assembled to a bellmouth with a given inclination in relation to the I-tube longitudinal axis. Figure 1.1 illustrates the second flexible riser-bend stiffener top connection with I-tube configuration in a FPSO top mounted internal turret [1], which is similar to a spread moored FPSO with riser balcony. The objective of this work is to analyze the complex flexible riser-bend stiffener top mechanical responses, and furthermore propose a monitoring approach with parameter estimation methodology to reduce modeling uncertainties in the riser top connection. The flexible pipe cross-section and end fitting, I-tube bellmouth and bend stiffener in the riser top connection together with its main failure models are introduced in Section 1.1; the detailed objective of this work is presented in Section 1.2; the organization of this thesis is summarized in Section 1.3.

1.1 Flexible riser-bend stiffener top connection

1.1.1 Flexible pipe cross section and end fitting

The unbounded flexible pipe is composed of several independent layers interacting with each other with low bending stiffness combined with high axial and torsional stiffness. Figure 1.2 presents a typical flexible riser cross section [2]. The main layers

are identified: i). the interlocked metallic carcass provides the collapse resistance; ii). the extruded polymer internal pressure sheath is used for the internal fluid integrity; iii). interlocked metallic pressure armors support the internal pressure sheath and system internal pressure loads in the radial direction; iv). tensile armor layers typically consist of the flat, round, or shaped metallic wires, in two or four layers helically cross-wound at an angle range from 20° and 60° , to sustain tensile loads and internal pressure totally or partially; v). the extruded polymer outer sheath can provide external fluid integrity.

Main failure models of flexible pipes are concerned in the design process with its increasing applications in deep and ultra-deep water: critical collapse pressure of carcass [6], overbending, radial and lateral buckling of tensile armour wires [7], rupture of tensile armour wire due to fatigue or abrasion [8]. Large bending forces may also result in the unlocking of the inter layer (carcass and pressure armour). And the corrosion of the tensile and pressure armour wires and degradation of the polymer layers by the flooded annulus environment can rapidly increase the fatigue damage of flexible pipe [9].

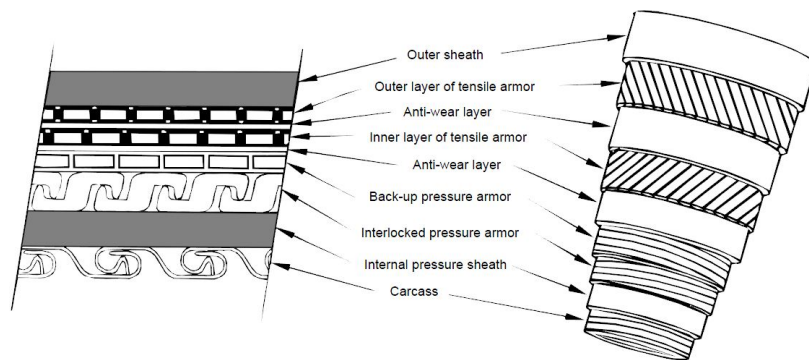


Figure 1.2: Schematic of typical flexible riser cross section [2].

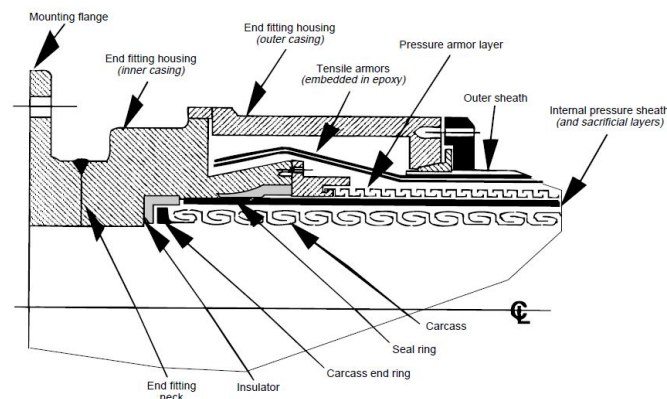


Figure 1.3: End fitting of an unbounded flexible pipe [2].

End fittings are the terminations of flexible pipes, which is illustrated in Fig. 1.3. The end fittings may be built during pipe manufacture or installed in the field. The

main functions of the end fittings are to terminate all the strength members in the construction of flexible pipes and ensure all axial loads and bending moments can be transmitted into the end connector on the vessel without affecting the sealing of fluid-containing layers. The end fitting effects the tensile armour stress calculation significantly for the bending problem [10, 11], which indicates this region can be critical in fatigue analyses.

1.1.2 I-tube bellmouth

The I-tube bellmouth system is usually designed to receive the bend stiffener with an end angle, as adopted by the turret moored FPSO in Schiehallion field [1, 12] and the spread moored FPSOs in Albacora Leste field [13], for examples. Figure 1.4 shows the I-tube bellmouth configuration in a FPSO with riser balcony. A polymeric curved plate sleeve, called “trumpet”, is assembled at the bend stiffener top base and the bellmouth adapter, to avoid riser overbending by an angle deviation inside the I-tube. The polymeric sleeve can also reduce the wear between the riser and I-tube and prevent possible rupture of the riser outer sheath. The contact pressure and relative displacement of riser outer sheath with the I-tube bellmouth interfaces are considered to be the cause of excessive wear [13–15] for the I-tube configuration.

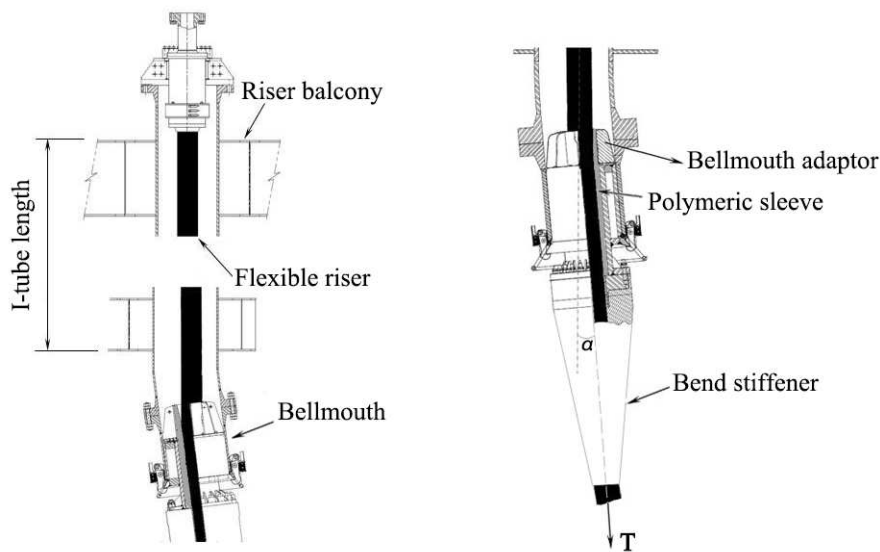


Figure 1.4: Riser-bend stiffener top connection with I-tube interface [3].

1.1.3 Bend stiffener

Bend stiffeners are conical polyurethane structures placed outside of flexible riser top, as shown in Fig.1.4, to ensure a smooth transition with the floating production units, which transfers the shear forces and bending moments principally from the

riser to the support structure. The design of bend stiffener is usually driven by the criteria of fatigue lifetime and minimum bending radius (MBR) of flexible riser [14, 15]. The main design parameters are the stiffener material, the stiffener length and the stiffener maximum external diameters, which greatly influence the mechanical behaviors of bend stiffeners. The polyurethane nonlinear elastic behavior [16, 17], nonlinear viscoelastic behavior for time domain [18] and steady-state formulations [19] of bend stiffener were recently investigated for the riser top connection.

1.2 Objective and methodology

The global dynamic analysis of flexible riser is usually implemented through a global finite element model with beam elements subjected to stochastic environmental loading and operational conditions. The effects of bend stiffener and I-tube interface in the curvature distribution of riser top connection can be either directly incorporated in the global dynamic model or separately assessed by an intermediate quasi-static model [18]. The time series of the effective top tension and curvature distribution are then used as input into a local cross-sectional analytical or numerical model to calculate the armour wire stresses. A stress transfer function can alternatively be employed to convert the obtained time-domain forces and moments in global analysis into tensile armour stresses [20]. The lifetime assessment procedure is followed by cycle counting the resulting irregular stress time series with the Rainflow technique. An appropriate $S - N$ curve selection is an important aspect for fatigue damage estimation due to the possibility of corrosive annulus environment caused by gas/water permeation through polymeric layers degradation mechanisms.

Due to the large degree of uncertainties associated to the lifetime estimation procedure, a safety factor of 10 is usually adopted (API 17J [21], DNV-OS-F201 [22]). If a comprehensive monitoring system is employed, a reduction of the safety factor conservatism may be achieved (API 17B [2]) and is being increasingly facilitated by sensor technology development combined with larger capacity of data storage and processing. The bend stiffener polyurethane mechanical response not only presents a nonlinear loading rate and temperature dependency but is also subjected to weather aging during operation, which may affect its mechanical behavior over time. The top tension, employed for riser local cross-section stress calculation, is usually obtained from global dynamic analyses performed under selected environmental conditions, if direct measurement is not available. As a consequence, both the bend stiffener effect on the curvature distribution and the top tension time series present inherent uncertainties for riser lifetime (re)assessment. A more realistic modeling approach combined with an inverse problem methodology to reduce modeling uncertainties in the riser-bend stiffener top connection is proposed by the

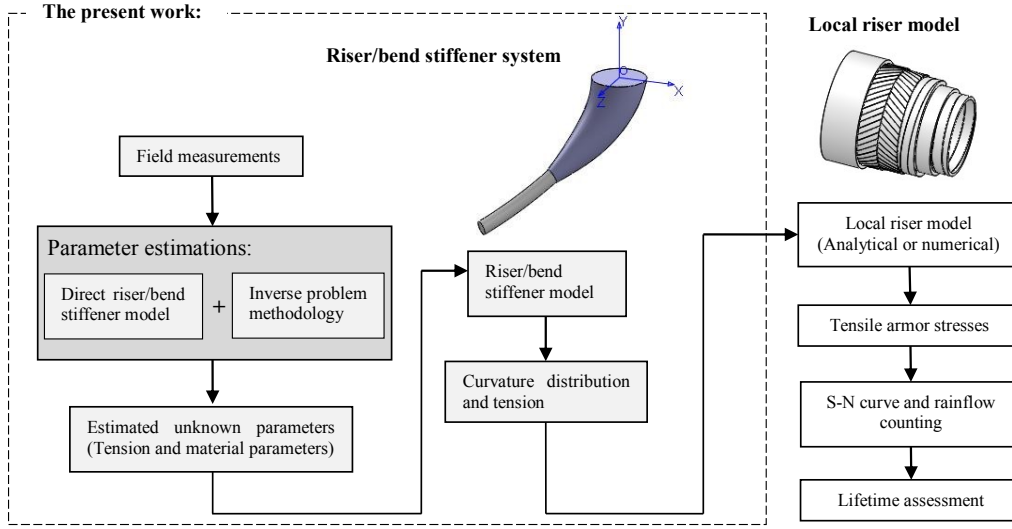


Figure 1.5: A proposed methodology for riser top connection lifetime assessment.

author for the further flexible riser lifetime (re)assessment with less conservatism, as illustrated in Fig.1.5. Once the unknown parameters are estimated by the inverse analysis, the direct model can be employed to calculate the curvature distribution. The curvature results are then used together with the top tension as input into a local cross-sectional analysis model for tensile armour stress calculation, followed by more accurate fatigue assessment.

In this work, a modeling approach of flexible riser-bend stiffener top connection and an inverse problem methodology for multiple parameter estimation in the riser/bend stiffener system are studied in detail as follows:

- An intermediate quasi-static analytical model capturing the complex interactions of riser/bend stiffener with I-tube interface is proposed and investigated for the flexible riser top connection;
- A monitoring approach composed by gyrometers installed along the bend stiffener length combined with the inverse problem methodology (Levenberg-Marquardt algorithm) and a direct riser/bend stiffener analytical model is proposed to numerically estimate the modeling uncertainties: polyurethane hyperelastic response and effective top tension;
- Furthermore, the proposed inverse analysis approach is applied in a full-scale riser/bend stiffener bending-tension test with optical configuration measurements to estimate the loading condition and polyurethane material response by using a direct finite element model and the Levenberg-Marquardt algorithm.

1.3 Organization of the thesis

The analysis of flexible riser-bend stiffener top connection and multiple parameter estimation in the riser/bend stiffener system are investigated in this thesis. Figure 1.6 illustrates the organization structure of the thesis. A literature review is given in the Chapter 2, followed by the analytical model of riser-bend stiffener top connection with I-tube interface in Chapter 3 and the inverse problem methodology in Chapter 4, and the multiple parameter estimation with experimental measurements is presented in Chapter 5. Finally, the conclusions of this work and suggestions to future work are given in Chapter 6

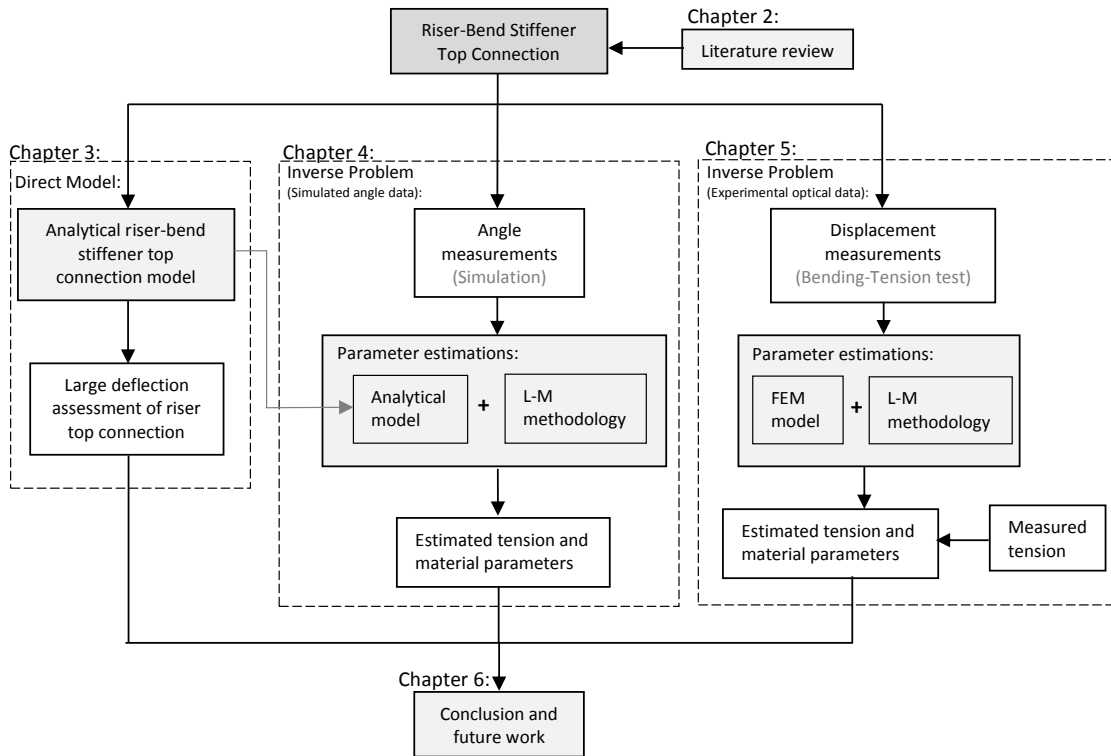


Figure 1.6: Overview of the organization structures of the thesis.

Chapter 2 reviews the literature on the analysis of the riser-bend stiffener top connection system, monitoring techniques in the riser top connection in field applications, the Levenberg-Marquart (L-M) algorithm for parameter estimation, flexible riser bending tests, and optical monitoring techniques. The riser/bend stiffener analysis is usually considered by an analytical model or finite element model based on the large deflection beam. A number of monitoring techniques are currently available for the flexible riser in field or laboratory tests. The L-M algorithm is widely regarded as a robust methodology for parameter estimation.

In Chapter 3, a large deflection beam model is developed to represent the riser top connection with I-tube considering that the bellmouth transition area with the

polymeric sleeve is represented by a straight rigid surface followed by a curved section. The analytical model incorporates the riser nonlinear bending behavior and the nonlinear elastic symmetric response of bend stiffener polyurethane. The mathematical formulation of the statically indeterminate system is presented which results in three systems of coupled differential equations combined with the corresponding multipoint boundary conditions to be numerically solved by an iterative procedure. The large deflection assessment of top connection with I-tube interface, and sleeve geometry and I-tube length influence are investigated by a case study.

In Chapter 4, an inverse problem methodology for multiple parameter estimation in the riser/bend stiffener system is proposed, consisting of gyrometers installed along the bend stiffener length, the L-M algorithm, and the direct analytical model proposed in Chapter 3. For the preliminary investigation purpose, the gyrometer data is numerically estimated by Monte Carlo simulations followed by a case study to investigate the number of sensors (up to 9) and arrangement influence on the inverse parameters estimation and methodology application feasibility for different loading conditions.

Chapter 5 presents the multiple parameter estimation in a bending-tension test of the riser/bend stiffener system with optical measurements. A full-scale bending-tension test of riser/bend stiffener system is conducted on the laboratory vertical rig. The configurations of the riser and bend stiffener sample during the test is measured by a proposed optical image-based technique. A finite element model is developed to represent the bending-tension test. Simultaneous estimation of material parameters and top tension in the riser/bend stiffener system is implemented based on the L-M algorithm combined with the direct finite element model and optical configuration measurements.

Chapter 2

Literature Review

This chapter presents a literature review of the works relevant to the proposed study in this thesis. Section 2.1 reviews the works on the analysis of flexible riser-bend stiffener top connection. Section 2.2 reviews monitoring techniques used in the riser top. Section 2.3 provides an overview of the inverse problem methodology for parameter estimation, with an emphasis on the Levenberg-Marquardt method which is adopted in this work. Previous studies on bending test of flexible risers are reviewed in Section 2.4. Section 2.5 reviews experimental measurement techniques used for the riser/bend stiffener system. Finally, Section 2.6 provides a summary of the literature review.

2.1 Analysis of flexible riser-bend stiffener top connection

Extreme and fatigue loading conditions have to be taken into account in the riser top connection design with its ancillaries of the bend stiffener and I-tube bellmouth. The riser bending in the top connection must be above the allowable MBR under extreme loading conditions. A global dynamic analysis of the riser is generally implemented by a global finite element model subjected to stochastic environment loading and operational conditions. The resulting top tension and angle can be applied into an intermediate local quasi-static model of riser top connection to calculate the curvature distribution. The obtained top tensions and curvature distributions are then applied to a local cross-section model to analyze the tensile armour wire stresses for the riser lifetime (re)assessment (SMITH [23]). API 17J [21], API 17L1 [14] and API 17L2 [15] establish the industry analysis considerations on static and dynamic riser.

A quasi-static intermediate large deflection beam model is usually used to represent the bending of the flexible riser top connection with an attached bend stiffener.

BOEF and OUT [24] developed an analytical beam model with large deflection for the riser/bend stiffener system. LANE *et al.* [25] pointed out that a three-dimensional finite element analysis of the riser/bend stiffener system is required for the assessment of stress concentration points in the interfaces between the metallic and polyurethane. VAZ *et al.* [16] extended the linear elastic symmetric material to nonlinear elastic asymmetric material based on the large deflection beam model, in which the neutral axis is eccentric due to shift from the cross-section centroid. Meanwhile, the bend stiffener and riser were modeled separately, which allows the calculation of the contact force. CAIRE *et al.* [26] studied the riser nonlinear bending curvature and moment relationship effect on the riser/bend stiffener system response based on the linear elastic beam bending model. CAIRE *et al.* [18] analyzed the nonlinear viscoelastic responses of polyurethane in the riser/bend stiffener system by using the large displacement beam bending model, and a steady-state formulation with the nonlinear viscoelastic bend stiffener was presented by CAIRE and VAZ [19]. The design optimization of bend stiffener for the riser top connection has been implemented recently by SMITH [23], TANAKA *et al.* [27], SODAHL and OTTESEN [28] and DROBYSHEVSKI [29]. MENICONI and LOPES [30] and DEMANZE *et al.* [31] proposed approaches for the bend stiffener lifetime assessment, which is affected significantly by the interface between the polyurethane and the inserted steel and body temperature.

The more realistic analysis approaches capturing the complex interaction of riser with bend stiffener and I-tube interface were concerned and employed for the flexible riser top connection analysis. Recently, CLEVELARIO *et al.* [3] presented a dynamic riser top connection test to evaluate the wear between the polymeric sleeve and riser outer sheath. PERDRIZET *et al.* [32] described a three-dimensional finite element model considering the riser end fitting effect and the interaction of riser with bend stiffener combined with a full-scale riser/bend stiffener bending test. ELOSTA *et al.* [33] proposed a finite element pipe-in-pipe model for the riser/bend stiffener system, which represents the interaction between riser and bend stiffener and captures the riser extended length.

2.2 Monitoring techniques in the riser top

A number of monitoring techniques were developed in the flexible riser top for a continuous integrity assessment, considering the damages caused by stress concentration, outer sheath abrasion, rupture of the tensile armors, fatigue failure due to the operational water depth, and corrossions. The integrity assessment monitoring techniques were employed or proposed in field (MARINHO *et al.* [8]): percolated gas surface monitoring for the riser annular space pressure; nitrogen injection in

the annular space and visual inspection through video camera for the riser outer sheath damage and deformation; magnetic system or camera video to monitor the riser torsion; electromagnetic stress measurement, acoustic emission or optical fiber sensors for the monitoring of tensile armour wire rupture.

The direct monitoring of flexible riser parameters in its top region were also applied to reduce lifetime assessment uncertainties. The tensile armor strain measured by optical fiber sensors and curvature estimation through strain gauges or accelerometers were investigated previously. ANDERSEN *et al.* [34] demonstrated the feasibility of using Fiber Bragg Grating sensing technology for strain monitoring in flexible risers. Strain sensors were embedded into a groove with epoxy in the inner tensile armour layer along its entire length in a full-scale test. WEPPE-NAAR and KRISTIANSEN [35] described a system based on Fiber Bragg Grating integrated in tensile armour wires, which would work as strain sensors at selected points along the pipe, monitoring strain data at critical locations, such as top connection. MORIKAWA *et al.* [36, 37] described the direct wire optical monitoring system called MODA in offshore operation, where all the wires in the riser external tensile armour layer were instrumented with Fiber Bragg Grating strain sensors. A window in the polymeric outer sheath of the pipe was temporarily opened to install the sensors and then repaired by a protective and anticorrosive layer. GASPARETTO [38] presented results from MODA system installed near the top end fitting to monitor the flexible riser end fitting fatigue life.

An alternative method is to monitor the curvature along the top connection length of riser and use it as an input to riser local analytical or numerical models to calculate the tensile armour stresses, which requires a certain number of sensors to ensure the result accuracy. LYONS *et al.* [39, 40] and TRARIEUX *et al.* [41] described the monitoring system called Foinaven Umbilical Monitoring System (FUMS) on the FPSO vessel Petrojarl IV. The sensors measured curvatures at three locations in two orthogonal directions in the region of the umbilical bend stiffener. Curvatures were detected by using strain gauges configured in pairs for each location and direction to ensure tension and temperature effects were eliminated. Subsequently, the acquired FUMS data were post-processed. ROBERTS *et al.* [42] proposed a monitoring system by inserting the fiberoptic strain sensors into the bend stiffener to determine the riser curvature along its length in the hang-off area. ELOSTA *et al.* [33] presented a monitoring system called Morphopipe, developing a dedicated polyurethane layer in an external riser annulus and embedding a network of accelerometers MEMS (Micro Electronic Mechanics Sensor), to measure the three dimensional curvature and twisting of pipes in topside dynamic area.

In the present work, a monitoring approach is proposed to measure the rotation angles of riser top. For FPSO riser's life extension in Bijupira-Salema oil field,

Shell Brazil installed 3 motion sensors from 4Subsea [43] in order to acquire the real data for riser and vessel motion. The motion sensor is an autonomous subsea sensor and data logger containing a 3-axis MEMS accelerometer and 3-axis MEMS gyroscope, with its operational frequencies from 10 Hz up to 1024 Hz. Chevron Tahiti's riser monitoring system in the riser hang-off region was designed by 2H Offshore [44] through several INTEGRIPod motion sensors [45], which measures axial acceleration, planar angular velocity, linear displacement, and static and dynamic inclination. For the three dimensional condition in field, the modified algorithms combined with numerical global dynamic model can be incorporated in the monitoring system to transform the monitored data into a plane problem.

2.3 Inverse problem methodology

The inverse problem is a process of calculating the causal factors from a set of observations. In a direct problem, the solution is sought with known boundary and initial conditions and all modeling parameters. Not all these parameters can be directly observed in an inverse problem. Instead, discrete measurements of the dependent variables in the same system can be used to estimate the unknown parameters. Generally, inverse problems are solved by minimizing an objective function with some stabilization techniques used in the estimation procedure. The regularization method can be related to damped least squares methods, such as the one due to Levenberg[46] and Marquardt[47]. The so-called Levenberg-Marquardt Method is a powerful iterative technique for nonlinear parameters estimation, which provides a compromise between the Steepest Descent and Gauss methods with the initial iterations close to the Steepest Descent method and the final iterations close to the Gauss method (BECK and ARNOLD [48]). The Steepest Descent method gives a direction for the iterative step but not a step size. Since the step size is arbitrary, this method can be very inefficient particularly as the minimum is approached. If the problem is ill-conditioned, especially near the initial guess, it is difficult to use the Gauss method for parameter estimations. The Levenberg-Marquardt method introduces constraints into the minimization of the summation of squared residuals to damp oscillation and instabilities due to the ill-conditioned character of the problem, by taking advantage of the Steepest Descent method.

The Levenberg-Marquardt method has been widely used in engineering problems of parameter estimation. OZISIK and ORLANDE [49] introduced the Levenberg-Marquardt method for parameter estimation in heat transfer problem. MOLIMARD *et al.* [50] presented the identification of four orthotropic plate stiffness using a single open-hole tensile test. FU *et al.* [51] described the parameter determination of double-ellipsoidal heat source model and its application in the multi-pass welding

process. SEON *et al.* [52] assessed the 3D shear stress-strain properties of composites using digital image correlation and finite element analysis based on the Levenberg-Marquart algorithm for minimization of weighted least squares error between the measured and finite element model predicted strains. HUANG *et al.* [53] presented the material parameter identification in functionally graded structures with measured displacements. The numerical results revealed that the Levenberg-Marquart algorithm not only has high accuracy and stable convergence, but is also robust to the effect of measured displacement noise. KAZEMI *et al.* [54] proposed an inverse approach for load identification of a viscoplastic material with some unknown viscoplastic constants, where both of the unknown constants and the applied load are simultaneously identified using two nested inverse algorithms. The damped Gauss and the Levenberg-Marquart methods are used for the load identification and unknown material parameters respectively.

2.4 Bending test of flexible pipe

Several full-scale flexible riser bending tests have been conducted in MARINTEK (Norway) [55, 56], COPPE-UFRJ (Brazil)[57], and IFP (France) [32, 58, 59] respectively. TAN *et al.* [55] presented a 4" flexible pipe bending test. The relationship between the pipe bending curvature and moment was measured at three different internal pressure levels. The extensometers were used to measure the strain in the pipe. SAEVIK [56] presented a full-scale fatigue test of 8" flexible riser with a length of 14.5 m. The horizontal test rig enables tension loading by a right end hydraulic cylinder and bending moment by means of two hydraulic cylinders moving the rockhead in the left end. A bellmouth made of two flat steel plates was applied to control the curvature during dynamic bending. SOUSA *et al.* [57] presented a 2.5" flexible pipe bending-tension test with a free span of 4.66 m and 1 up to 4 broken wires in its outer tensile armour. Tensile and transverse loads are simultaneously imposed on the pipe respectively by one hydraulic actuator in one end of pipe and another transverse actuator resting on the pipe. Seven displacement transducers were used to measure the axial displacements and the transverse displacement along the pipe. LEROY *et al.* [58] presented a bending test of 6" flexible pipe with a length of 8 m. One end fitting is anchored on the ground, and the other end fitting was cyclically moved up and downwards in vertical plane. The curvature of pipe was measured by a dedicated image treatment tool. LEROY and ESTRIER [59] introduced a bending test of 4" flexible pipe with 8 m length. Imposed rotations and translation in the end fittings were chosen to obtain constant variations of curvature along the pipe. Parallel strain gauges were used to obtain both axial and transverse strain variations. PERDRIZET *et al.* [32] presented a 8" riser bending-tension test

with bend stiffener. The axial tension and bending cycles are respectively applied by the end tension jack and the swinging table rotations.

2.5 Experimental measurements

The conventional techniques, LVDTs (linear variable displacement transformers), potentiometers and strain gauges, to measure the structure displacements, rotations or curvatures are considered to be complex and limited for the riser/bend stiffener bending test. Potentiometers or LVDTs track the vertical or horizontal displacement. The mounting of these devices requires a complex structure to ensure the small influence of structure vibration. And the size of sensors is specialized which depends on the sample displacement. Strain gauges are easier to mounting, while its application in the bend stiffener may cause three dimensional or localized error due to the conical shape of bend stiffener.

An image-based approach to track the displacements of riser/bend stiffener system is proposed for the bending test applying image acquisition with luminescent targets, and image processing and analysis. The advantages of the proposed method are non-intrusive and allowing spatial and temporal measurements at custom positions and regions of interest. RAMESH *et al.* [60] pointed out the application of binary images makes the vision system faster and less expensive than those operation on color or gray-level images due to smaller memory and processing requirements. After the binary of image, a following image analysis is implemented to computer the shape properties of the objects. Morphological operations for the binary image analysis were interested by medical application (SIRISHA *et al.* [61]), pattern recognition (ZHANG [62]), and geoscience (GROVE and JERRAM [63]).

HERNÁNDEZ *et al.* [64] presented water elevation measurements using binary image analysis for two-dimensional hydrodynamic experiments at the Ocean Technology Laboratory (LabOceano/COPPE-UFRJ). Lens correction and calibrations of the acquired images were preformed with a circle pattern table using Open Source Computer Vision Library (OpenCV[65]). The image processing and analysis were developed in the ImageJ open-source software [66]. HERNÁNDEZ *et al.* [67] described a three-dimensional image-based approach for imperfect structures surface modeling. The procedure is illustrated by using two damaged tubular member samples reconstruction and a three-dimensional mapping of a ship panel.

2.6 Summary

A literature review of flexible riser top connection analysis, monitoring techniques used in the riser top, parameter estimation methodology, bending test of flexible riser

and experimental measurement techniques used for the riser/bend stiffener system is presented in this chapter. A following summary based on the related literature reviews is given for the proposed study in this thesis:

- A detailed modeling analysis of flexible riser top connection is required to study the complex mechanical behavior of riser with bend stiffener and I-tube bellmouth interface;
- For the field application, a number of monitoring techniques in the riser top can be used for specialized objectives. A monitoring approach through accelerometers/gyrometers installed along riser/bend stiffener length is proposed to measure the rotation angles of riser top;
- A full-scale riser/bend stiffener bending-tension test is usually conducted to study mechanical behaviors of riser top connection considering the corresponding non-uniform curvature distribution along the pipe;
- The optical image-based approach is regarded as a suitable method to measure the displacements of sample during the experimental test of riser/bend stiffener system. However, for the field application of optical monitoring system in riser top, the operational environment of camera devices is considered to be harsh;
- An inverse analysis based on the monitored rotation angles or configurations in flexible riser top connection combined with the Levenberg-Marquart algorithm can be employed to estimate the modeling uncertainties of the riser/bend stiffener system: polyurethane hyperelastic response and top tension, for example. And then the riser curvature can be calculated based on the estimations.

Chapter 3

Modeling of Flexible Riser-Bend stiffener Top Connection

This chapter presents a large deflection beam formulation for the flexible riser-bend stiffener top connection with I-tube interface, considering that the bellmouth transition area with the polymeric sleeve is represented by a straight rigid surface followed by a curved section. In addition, the riser has a nonlinear bending behavior represented by a bilinear moment vs curvature function and the bend stiffener polyurethane material exhibits nonlinear elastic symmetric response represented by a power law function. Section 3.1 presents the mathematical formulation of the statically indeterminate system consisting of three systems of coupled differential equations with corresponding multi-point boundary conditions. Section 3.2 presents the iterative numerical procedure applied to solve the multiple-points boundary value problem. Section 3.3 presents a case study with a 7" field applied water injection riser protected by a 1.8 m bend stiffener connected to an I-tube with 7° inclination and subjected to extreme loading conditions. Section 3.4 presents the conclusions of this chapter.

3.1 Mathematical formulation

The flexible riser top connection protected by a bend stiffener and I-tube interface is represented by a large displacement beam model subjected to a tip tension F , angle ϕ_L between the rise tangent and the vertical axis, and angle α between the tension and the riser tangent, as schematically shown in Fig. 3.1(a). The riser is fixed in the end fitting position located at point O and starts contacting the rigid sleeve in point A . The sleeve consists of a curved section AB , with constant radius R_{AB} , followed by a straight section BC . It is considered to be fixed at point C and rotated by an angle ϕ_0 in relation to the Y axis of the Cartesian coordinates (X ,

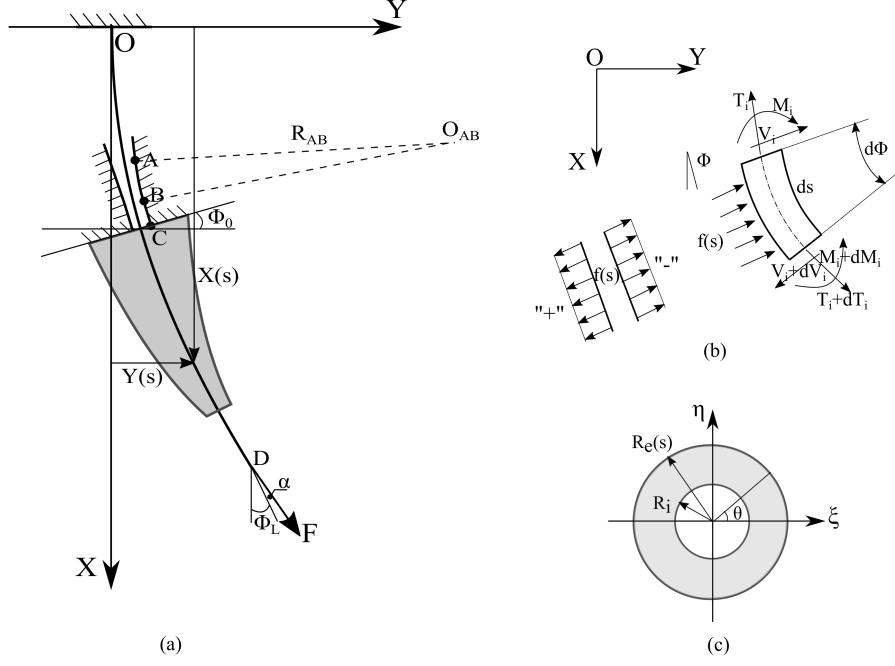


Figure 3.1: (a) Riser-bend stiffener top connection system with I-tube interface beam model; (b) Infinitesimal element; (c) Bend stiffener cross-section.

Y). By assuming that there is no separation in the sleeve region, the riser exhibits a constant curvature value κ_{AB} in the curved section AB and in the straight section BC the riser is considered to have zero curvature until the bend stiffener starts at point C . The mathematical formulation is based on the following assumptions and simplifications,

- Euler-Bernoulli large deflection beam theory is employed;
- the beam is inextensible (neutral axis length is constant);
- the flexible riser has nonlinear bending behavior represented by a bilinear moment vs curvature function;
- the bend stiffener polyurethane material exhibits nonlinear elastic symmetric response represented by a power law function;
- self-weight, frictional forces and dynamic effects are disregarded;
- the gap between the riser and bend stiffener is disregarded;
- the polymeric sleeve in the I-tube transition area is considered to be rigid.

3.1.1 Geometrical relations

An infinitesimal element ds of the beam system is schematically shown in Fig. 3.1(b) in the X and Y Cartesian coordinate system considering that there is no gap between

the riser and bend stiffener. Applying trigonometrical relations to it and considering the curvature as the slope angle rate of change with respect to the distance ds along the neutral axis, leads to the following relations,

$$\frac{dX}{ds} = \cos \phi(s) \quad (3.1a)$$

$$\frac{dY}{ds} = \sin \phi(s) \quad (3.1b)$$

$$\frac{d\phi}{ds} = \kappa(s) \quad (3.1c)$$

where s is the arc-length along the riser top connection system ($0 \leq s \leq L$), L is the total length, $X(s)$ and $Y(s)$ are the deflected riser/bend stiffener coordinates, $\phi(s)$ is the angle between the tangent to the beam axis and the X axis, and $\kappa(s)$ is the curvature.

3.1.2 Equilibrium of internal forces and moments

A schematic of the internal forces and moments in a riser and bend stiffener infinitesimal element is also shown in Fig. 3.1(b). Eliminating multiplication of differential terms, the equilibrium of normal and tangential forces and bending moments yields,

$$\frac{dV_i}{ds} - T_i \frac{d\phi_i}{ds} - (-1)^i f = 0 \quad (3.2a)$$

$$\frac{dT_i}{ds} + V_i \frac{d\phi_i}{ds} = 0 \quad (3.2b)$$

$$\frac{dM_i}{ds} - V_i = 0 \quad (3.2c)$$

where the subscripts $i = 1$ and 2 refer to the riser and bend stiffener, respectively, $V_i(s)$, $T_i(s)$ and $M_i(s)$ are the shear forces, axial forces and bending moments, and $f(s)$ is the contact force between the riser and bend stiffener, which is zero outside bend stiffener and sleeve sections, assuming there is no flexible riser contact in the I-tube region from point O to A . Contact force is positive “+” or negative “-” depending on its direction in the bending plane, as presented in Fig. 3.1(b). Algebraically manipulating the horizontal and vertical infinitesimal equilibrium equations (3.2a) and (3.2b), they may also be described according to,

$$\text{Horizontal (Y-axis): } \frac{d}{ds}(T_i \cos \phi + V_i \sin \phi) - (-1)^i f \sin \phi = 0 \quad (3.3a)$$

$$\text{Vertical (X-axis): } \frac{d}{ds}(T_i \sin \phi - V_i \cos \phi) + (-1)^i f \cos \phi = 0 \quad (3.3b)$$

3.1.3 Constitutive relations and pure bending formulation

Flexible riser

The bending behavior of a flexible riser is governed by interlayer friction mechanisms leading to a hysteretic response when subjected to cyclic loading. The nonlinear bending moment and curvature relationship of flexible riser is shown in Fig. 3.2. For low values of curvature, the interlayer friction forces are able to prevent tensile armours slippage, which results in a high bending stiffness EI_{ns} value. Slippage starts gradually between layers after the curvature reaches a certain critical value, nonlinearly reducing the bending stiffness until the full slippage value EI_{fs} is reached. This nonlinear behavior and stiffness transition is highly affected by the interlayer contact pressure resulting from axisymmetric loading (tension, internal and external pressure), but in the present formulation, for simplification purposes, the transition from the stick to the slip domain is simplified into a bilinear relationship, as follows,

$$M_1(s) = \begin{cases} EI_{ns}\kappa(s), & |\kappa(s)| \leq |\kappa_{cr}| \\ EI_{fs}\kappa(s) + (EI_{ns} - EI_{fs})\kappa_{cr}, & |\kappa(s)| > |\kappa_{cr}| \end{cases} \quad (3.4)$$

where κ_{cr} is the critical curvature at which the stiffness transition occurs, EI_{ns} is the no-slip bending stiffness, and EI_{fs} is the full-slip bending stiffness.

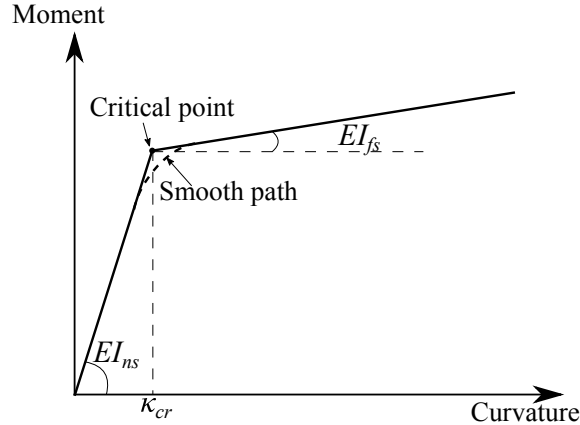


Figure 3.2: Nonlinear bending moment and curvature relationship of flexible riser.

Bend stiffener

The polyurethane employed for bend stiffener manufacture presents a nonlinear mechanical behavior that is different under tension and compression and highly dependent on temperature and loading rate. In general, higher rates lead to a stiffer response and when this effect is disregarded, a hyperelastic modeling approach may

be employed considering the material at a given constant temperature. Further simplification can be employed for a beam bending formulation, where a general nominal stress vs nominal strain function can be used to fit experimental data obtained from uniaxial tensile tests. In the present work, the polyurethane nonlinear elastic behavior is considered to be symmetric (same response for tension and compression) and represented by a two parameters power function defined by,

$$\sigma(\epsilon) = \text{sign}(\epsilon)E_q|\epsilon|^q \quad (3.5)$$

where σ and ϵ are the nominal stress and strain respectively, and E_q and q are the material parameters. The function $\text{sign}(\epsilon)$ is defined as $\epsilon/|\epsilon|$ to determine positive or negative strain under tension or compression, respectively. Tensile tests of typical bend stiffener polyurethane samples have been previously performed in a servo hydraulic testing machine at a constant room temperature 24°C with three different stretch rates (5, 50 and 500 mm/min), as presented by [18]. In the present work, the stress vs strain response obtained for the 50 mm/min loading rate, as shown in Fig. 3.3, is selected for the case study and adjusted up to 15% by Eq. (3.5), leading to the following material parameters: $E_q = 20.19$ MPa and $q = 0.4738$.

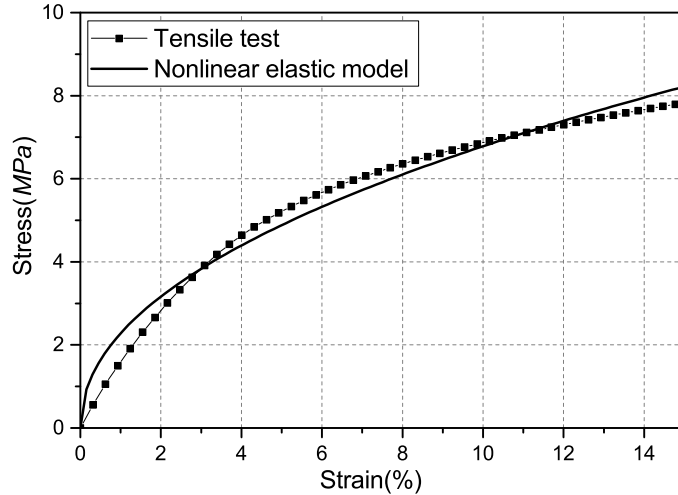


Figure 3.3: Nominal stress versus nominal strain for the tensile test and nonlinear elastic model ($E_q=20.19$ MPa and $q=0.4738$).

Considering Euler-Bernoulli beam bending theory for the riser/bend stiffener system, the strain ϵ at a distance η from the neutral axis can be expressed by $\epsilon(\eta, s) = \eta\kappa(s)$. As the bend stiffener material is assumed to be nonlinear elastic symmetric in tension and compression, the neutral axis coincides with the cross-section centroid during bending. Consequently, the equilibrium of bending moment

for the bend stiffener cross-section area yields,

$$M_2(s) = \int_{ABS} \sigma_{BS} \eta dA = \text{sign}(\kappa(s)) E_q |\kappa(s)|^q I_{BS}(s) \quad (3.6)$$

with the geometrical function $I_{BS}(s)$ given by,

$$I_{BS}(s) = \int_{ABS} |\eta|^{q+1} dA = 2 \left[\left(\frac{D_e(s)}{2} \right)^{q+3} - \left(\frac{D_i}{2} \right)^{q+3} \right] \int_{-\frac{\pi}{2}}^{\frac{\pi}{2}} |\sin \theta|^{q+1} \cos^2 \theta d\theta \quad (3.7)$$

where, as shown in Fig. 3.1(c), the subscript BS refers to the bend stiffener cross-section in the Cartesian coordinates (η, ξ) . $D_e(s)$ and D_i are, respectively, the external and internal diameters, dA is an infinitesimal element of area, and θ is the angle of infinitesimal element position related to the ξ axis.

3.1.4 Governing equations

The top connection system governing equations may be separately obtained for different sections and combined with appropriate multipoint boundary conditions. The three sections adopted are schematically presented in Fig. 3.4 and defined as follows,

1. Section I ($0 \leq s \leq s_1$): flexible riser from fixed boundary condition at point O up to the contact point A in the sleeve, with an arc-length given by s_1 ;
2. Section II ($s_1 \leq s \leq s_3$): flexible riser contact region with the sleeve, from point A to C . The distances s_2 and s_3 define the arc-lengths from point O to B and C , respectively. The segment AB consists of a curved section with constant radius R_{AB} and arc-length given by $s_{AB} = s_2 - s_1$. The straight section BC has an arc-length defined by $L_{BC} = s_3 - s_2$. The sleeve contact constraint enforces a reaction force N_A at point A and a reaction moment M_B at point B to the flexible riser, as shown in Fig. 3.4(a);
3. Section III ($s_3 \leq s \leq L$): flexible riser/bend stiffer section CD with an arc-length of $L_{CD} = L - s_3$. The arc-length s_4 is defined from the point O to the bend stiffener tip end. The bend stiffener has a total length of L_{BS} . The loading (F, ϕ_L, α) is applied to the end of the flexible riser segment at $s = L$.

Section I ($0 \leq s \leq s_1$) - flexible riser extended section

Isolating the first section, where there is no contact force, the shear and tension forces at point A can be respectively defined as, $T_A = T_1(s_1)$ and $N_A = V_1(s_1)$,

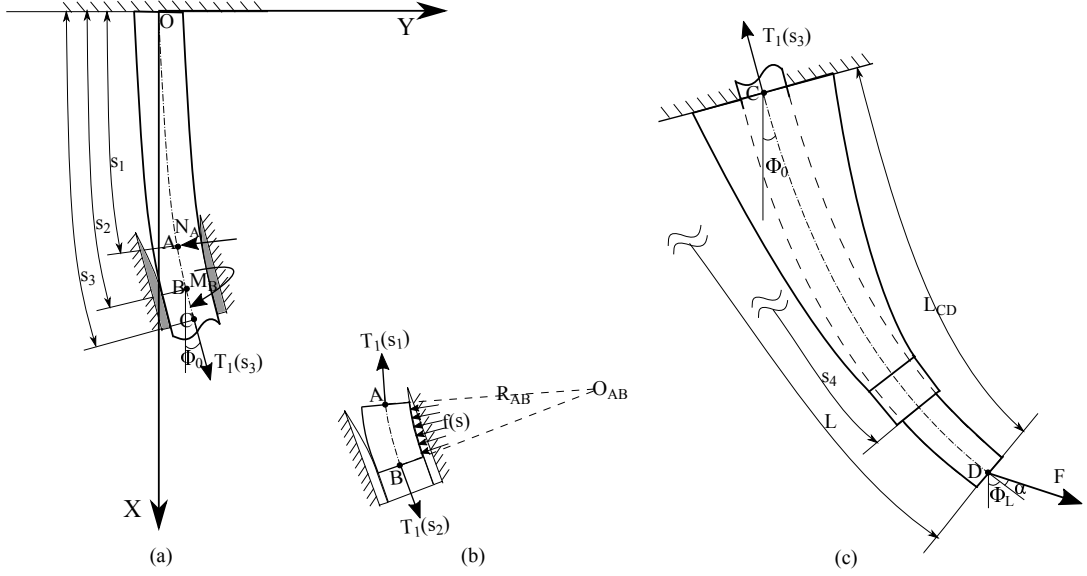


Figure 3.4: Schematic of the riser-bend stiffener top connection model: (a) Configuration of the extended riser section in the I-tube area; (b) Contact force of the riser with the sleeve; (c) Configuration of riser/bend stiffener section.

with a neutral axis slope given by $\phi(s_1) = \phi_A$. Integrating Eqs. (3.3a) and (3.3b) considering these constants, leads to,

$$T_1(s) \sin(\phi(s)) - V_1(s) \cos(\phi(s)) = T_A \sin \phi_A - N_A \cos \phi_A \quad (3.8a)$$

$$T_1(s) \cos(\phi(s)) + V_1(s) \sin(\phi(s)) = T_A \cos \phi_A + N_A \sin \phi_A \quad (3.8b)$$

Further manipulating Eqs. (3.8a) and (3.8b) yields the following shear force equation,

$$V_1(s) = T_A \sin(\phi(s) - \phi_A) + N_A \cos(\phi(s) - \phi_A) \quad (3.9)$$

Introducing Eq. (3.9) into Eq. (3.2c) with the riser bending moment formulation (3.4) yields,

$$\frac{d\kappa(s)}{ds} = \begin{cases} \frac{1}{EI_{ns}} (T_A \sin(\phi(s) - \phi_A) + N_A \cos(\phi(s) - \phi_A)), & |\kappa(s)| \leq |\kappa_{cr}| \\ \frac{1}{EI_{fs}} (T_A \sin(\phi(s) - \phi_A) + N_A \cos(\phi(s) - \phi_A)), & |\kappa(s)| > |\kappa_{cr}| \end{cases} \quad (3.10)$$

Equation (3.10) and the geometrical relations (3.1a) - (3.1c) form a system of four first-order nonlinear differential equations for the coordinates $X(s)$ and $Y(s)$, angle $\phi(s)$ and curvature $\kappa(s)$ in the riser extended section.

Section II ($s_1 \leq s \leq s_3$) - flexible riser/sleeve contact region

The riser deflection in the sleeve contact region is assumed to follow the curved sleeve geometrical shape in the segment AB followed by the straight segment BC ,

yielding the following angle relations,

$$\begin{cases} d\phi(s)/ds = \kappa_{AB}, & s_1 \leq s \leq s_2 \\ \phi(s) = \phi_0, & s_2 \leq s \leq s_3 \end{cases} \quad (3.11)$$

Introducing the constant curvature κ_{AB} into the flexible riser bending moment vs curvature relation given by (3.4) and considering the flat sleeve region BC leads to the following relation,

$$M_1(s) = \begin{cases} \begin{cases} EI_{ns}\kappa_{AB}, & |\kappa_{AB}| \leq |\kappa_{cr}| \\ EI_{fs}\kappa_{AB} + (EI_{ns} - EI_{fs})\kappa_{cr}, & |\kappa_{AB}| > |\kappa_{cr}| \end{cases}, & s_1 \leq s \leq s_2 \\ 0, & s_2 \leq s \leq s_3 \end{cases} \quad (3.12)$$

which from Eq. (3.2c) results in a zero shear force V_1 distribution in this region and employing Eq. (3.2b) a constant tension $T_1(s_1) = T_1(s_3) = T_A$ is obtained. It should be noted that in the transition from the curved to the flat region in the sleeve, the bending moment distribution drops from a constant value caused by the concentrated reaction moment $M_B = M_1(s_2)$ to zero. The contact force between the riser and the sleeve can be calculated employing Eq. (3.2a) considering the constant curvature κ_{AB} in section AB and the zero curvature in section BC , as shown in Fig. 3.4(b), leading to,

$$f(s) = \begin{cases} T_A\kappa_{AB}, & s_1 \leq s < s_2 \\ 0, & s_2 \leq s \leq s_3 \end{cases} \quad (3.13)$$

Section III ($s_3 \leq s \leq L$) - flexible riser/bend stiffener

For the riser/bend stiffener section (segment CD) in Fig. 3.4(c), summing up Eqs. (3.2a)-(3.2c) for the riser $i = 1$ and bend stiffener $i = 2$, yields,

$$\frac{dV}{ds} - T\frac{d\phi}{ds} = 0 \quad (3.14a)$$

$$\frac{dT}{ds} + V\frac{d\phi}{ds} = 0 \quad (3.14b)$$

$$\frac{dM}{ds} - V = 0 \quad (3.14c)$$

where $M = M_1 + M_2$, $T = T_1 + T_2$ and $V = V_1 + V_2$ are the total bending moment, tension and shear force of riser/bend stiffener section respectively. Considering the tip loading condition defined by the force F and angles α and ϕ_L and integrating Eqs. (3.3a) and (3.3b), leads to,

$$T(s) \sin(\phi(s)) - V(s) \cos(\phi(s)) = F \sin(\phi_L + \alpha) \quad (3.15a)$$

$$T(s) \cos(\phi(s)) + V(s) \sin(\phi(s)) = F \cos(\phi_L + \alpha) \quad (3.15b)$$

that can be solved to find the total shear force relation given by,

$$V(s) = -F \sin(\phi_L + \alpha - \phi(s)) \quad (3.16)$$

Introducing Eq. (3.16) into Eq. (3.14c) with the bending moment formulations (3.4) and (3.6) of the riser and bend stiffener, respectively, yields,

$$\frac{d\kappa(s)}{ds} = - \begin{cases} \frac{1}{EI_{ns} + E_q q |\kappa(s)|^{q-1} I_{BS}(s)} \left(F \sin(\phi_L + \alpha - \phi(s)) + \text{sign}(\kappa(s)) E_q |\kappa(s)|^q \frac{dI_{BS}(s)}{ds} \right), & |\kappa(s)| \leq |\kappa_{cr}| \\ \frac{1}{EI_{fs} + E_q q |\kappa(s)|^{q-1} I_{BS}(s)} \left(F \sin(\phi_L + \alpha - \phi(s)) + \text{sign}(\kappa(s)) E_q |\kappa(s)|^q \frac{dI_{BS}(s)}{ds} \right), & |\kappa(s)| > |\kappa_{cr}| \end{cases} \quad (3.17)$$

Equation (3.17) and the geometrical equations (3.1a) - (3.1c) form the system of four first-order nonlinear differential equations in the riser/bend stiffener section. Generally, a geometrical discontinuity exists at the bend stiffener tip end due to the tip thickness, which is taken into account by ensuring the total moment continuity in the riser/bend stiffener section.

3.1.5 Geometrical compatibility

The arc-length s_{AB} of the curved sleeve section may be written as a function of the initial contact angle ϕ_A and the sleeve inclination ϕ_0 , as follows,

$$s_{AB} = R_{AB}(\phi_0 - \phi_A) \quad (3.18)$$

and arc-lengths of riser/sleeve and riser/bend stiffener sections can be described by summations of riser extended arc-length s_1 , s_{AB} , L_{BC} and L_{BS} ,

$$s_2 = s_1 + s_{AB} \quad (3.19a)$$

$$s_3 = s_1 + s_{AB} + L_{BC} \quad (3.19b)$$

$$s_4 = s_1 + s_{AB} + L_{BC} + L_{BS} \quad (3.19c)$$

and the length of riser/bend stiffener section is presented by,

$$L_{CD} = L - s_1 - s_{AB} - L_{BC} \quad (3.20)$$

as schematically presented in Fig. 3.4. As the sleeve is fixed in the point C with given coordinates, the coordinates of initial contact point A in the sleeve are geometrically

related to R_{AB} , ϕ_A and ϕ_0 according to,

$$X_A = X_C - L_{BC} \cos \phi_0 - R_{AB}(\sin \phi_0 - \sin \phi_A) \quad (3.21a)$$

$$Y_A = Y_C - L_{BC} \sin \phi_0 + R_{AB}(\cos \phi_0 - \cos \phi_A) \quad (3.21b)$$

and the coordinates of point B yield,

$$X_B = X_C - L_{BC} \cos \phi_0 \quad (3.22a)$$

$$Y_B = Y_C - L_{BC} \sin \phi_0 \quad (3.22b)$$

The contact angle ϕ_A and the arc-length s_1 are under the following system geometrical restrictions: $\sqrt{X_A^2 + Y_A^2} \leq s_1 \leq X_A + Y_A$ and $0 \leq \phi_A \leq \phi_0$.

3.1.6 Multipoint boundary conditions

The riser-bend stiffener top connection beam system is under multipoint boundary conditions, which consists of a built-in point O in the end fitting position, fixed constraints due to the sleeve curved section AB and straight section BC , a bend stiffener rotation in the connection point C with the sleeve and a flexible riser tip end rotation at point D . The boundary conditions are defined, for each point, as follows,

- i). Point O - fixed boundary condition in the end fitting position ($s = 0$):

$$X(0) = 0, \quad Y(0) = 0 \quad \text{and} \quad \phi(0) = 0 \quad (3.23a-c)$$

- ii). Point A - flexible riser initial contact point with the sleeve ($s = s_1$):

$$X(s_1) = X_A, \quad Y(s_1) = Y_A, \quad \phi(s_1) = \phi_A \quad \text{and} \quad \frac{d\phi(s_1)}{ds} = \kappa_{AB} \quad (3.24a-d)$$

where ϕ_A is the riser initial contact angle with the sleeve and (X_A, Y_A) are the contact point coordinates. The sleeve normal reaction force N_A is applied to the riser at this point.

- iii). Point B - end of sleeve curved section ($s = s_2$):

$$X(s_2) = X_B, \quad Y(s_2) = Y_B \quad \text{and} \quad \phi(s_2) = \phi_0 \quad (3.25a-c)$$

where ϕ_0 is the sleeve inclination and (X_B, Y_B) are the coordinates of point B . The sleeve reaction moment M_B is applied to the riser at this point.

iv). Point C - end of sleeve flat section and beginning of bend stiffener ($s = s_3$):

$$X(s_3) = X_C, \quad Y(s_3) = Y_C \quad \text{and} \quad \phi(s_3) = \phi_0 \quad (3.26\text{a-c})$$

where (X_C, Y_C) are the coordinates of point C and ϕ_0 is the bend stiffener base inclination relative to the X axis, which is the same as the sleeve inclination.

v). Point D - flexible riser tip ($s = L$):

$$\phi(L) = \phi_L \quad (3.27)$$

where ϕ_L is the rotation angle in the riser tip end.

Table 3.1: Top connection system geometrical and loading parameters

Input data	$(X_B, Y_B), (X_C, Y_C)$ - sleeve coordinates ϕ_0 - sleeve rotation angle R_{AB} - sleeve radius ($\kappa_{AB} = 1/R_{AB}$) L, L_{BS} and L_{BC} - total riser, bend stiffener and sleeve flat segment length F, ϕ_L and α - loading conditions
Unknowns	s_1 - arc-length of segment OA ϕ_A - initial contact angle N_A - reaction force

3.2 Numerical solution procedure

The system of sections I , II and III coupled governing differential equations, subjected to boundary conditions (3.23) - (3.27) and geometrical compatibility equations (3.18) - (3.22) forms a multipoint boundary value problem (BVP) of the riser/bend stiffener top connection system with I-tube. Table 3.1 summarizes the input and unknown geometrical and loading parameters. The initial contact angle ϕ_A and arc-length s_1 of segment OA are geometrical unknown parameters. The riser initial contact point coordinates (X_A, Y_A) with the sleeve are unknown parameters that can be calculated with Eq. (3.21) once the angle ϕ_A and arc-length s_1 are iteratively found. The sleeve reaction force N_A at contact point A is another unknown to be solved. The Mathematica package [68] is employed for the iterative numerical solution following the flowchart presented in Fig. 3.5 and detailed as follows:

- i). Start the loop ($m = 0$) with initial values given by: angle $\phi_A^0 = \phi_0$, arc-length $s_1^0 = \sqrt{X_B^2 + Y_B^2}$ and tension $T_A^0 = F$;
- ii). Calculate the riser/bend stiffener section length L_{CD}^m with Eq. (3.20);

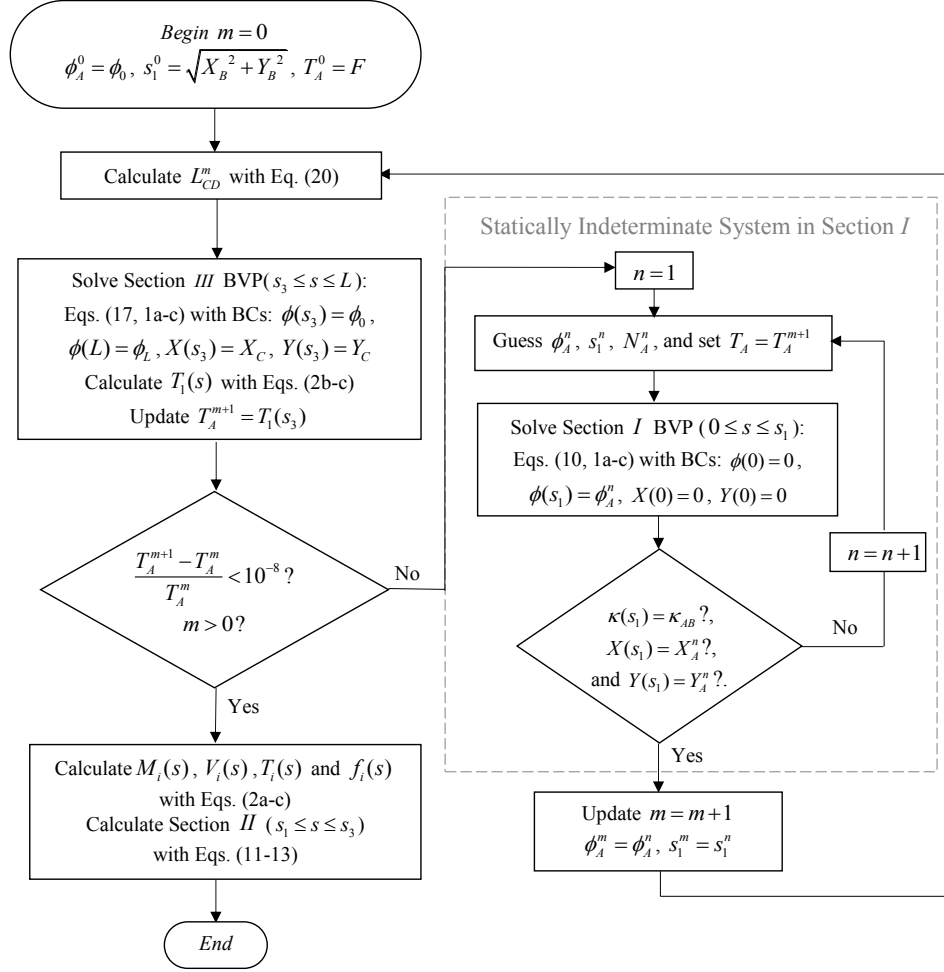


Figure 3.5: Flowchart of numerical solution procedure for flexible riser-bend stiffener top connection system.

iii). Solve section *III* BVP with governing equations given by Eqs. (3.17), (3.1a) - (3.1c) and boundary conditions (3.26a-c) and (3.27) with the shooting method, that converts the BVP problem into an equivalent initial value problem (IVP). As there is a curvature discontinuity at the bend stiffener tip, a modified shooting method is employed to capture this effect, as follows: a) Guess an initial curvature $\kappa(s_3)$, and integrate two differential equations (3.17) and (3.1c) with $\kappa(s_3)$ and $\phi(s_3) = \phi_0$ until the bend stiffener tip, $s_4 = s_3 + L_{BS}$. Therefore, curvature $\kappa(s_4)^-$ and angle $\phi(s_4)$ at the left side of bend stiffener tip are obtained. Ensure the moment continuity at this point, i.e., total moment at the left side of bend stiffener tip (composed of riser and bend stiffener), $M(s_4) = M_1(s_4) + M_2(s_4)$, is equal to the total moment at the right side of the tip (only riser). With this condition, the riser curvature discontinuity

$\kappa(s_4)^+$ is calculated at the right side of bend stiffener tip,

$$\kappa(s_4)^+ = \begin{cases} \frac{1}{EI_{ns}} M(s_4), & |M(s_4)| \leq |M_{cr}| \\ \frac{1}{EI_{fs}} (M(s_4) - (EI_{ns} - EI_{fs})\kappa_{cr}), & |M(s_4)| > |M_{cr}| \end{cases} \quad (3.28)$$

where $M_{cr} = EI_{ns}\kappa_{cr}$ is the critical bending moment in the nonlinear riser bending curvature and moment relationship. With angle $\phi(s_4)$ and “jumped” curvature $\kappa(s_4)^+$, integrate two differential equations (3.17) and (3.1c) from the bend stiffener tip $s = s_4$ to the riser end $s = L$, and compare the calculated angle $\phi(L)$ with the specified boundary condition ϕ_L ; b) Update the initial curvature with the bisection method and restart the process until the calculated angle $\phi(L)$ matches the specified angle ϕ_L with a given convergence criteria $\frac{\phi(L) - \phi_L}{\phi_L} \leq 10^{-5}$; c) After this BVP solution is found, calculate $T_1(s)$ employing Eqs. (3.2c) and (3.2b) to update $T_A^{m+1} = T_1(s_3)$;

iv). Check stop criteria with $(T_A^{m+1} - T_A^m)/T_A^m$ after the first m loop. If satisfied go to (v.). If not, set $n = 1$ and proceed with the Section I BVP loop as follows:

- (a). Guess angle ϕ_A^n , arc-length s_1^n , reaction force N_A^n and set tension $T_A = T_A^{m+1}$;
- (b). Solve section I BVP with governing equations defined by (3.10), (3.1a) - (3.1c) and boundary conditions (3.23a-c) and (3.24c). The Mathematica FindRoot function [68] is employed to search for a numerical solution to the simultaneous equations until the roots are found to a specified accuracy;
- (c). Update $m = m + 1$ and set $\phi_A^m = \phi_A^n$ and $s_1^m = s_1^n$. Return to ii.);
- v). Calculate the moments $M_i(s)$, shear forces $V_i(s)$, axial forces $T_i(s)$ and contact force $f_i(s)$ with Eqs. (3.2a) - (3.2c);
- vi). Calculate Section II with Eqs. (3.11) - (3.13).

3.3 Case study

A case study is carried out with a 7^m flexible riser with a total arc-length of $L_1 + 4m$, surrounded by a fixed sleeve inside the I-tube end and protected by a 1.8 m bend stiffener, as presented in Fig. 3.6. An I-tube turning point with 7° inclination occurs at L_1 , followed by a 1.2 m segment length up to the bend stiffener base. The sleeve consists of a curved section with a constant bending radius R_{AB} and a straight section of 0.5 m. Two loading conditions on the riser-bend stiffener top connection system are considered, corresponding to static and dynamic extreme values, respectively: ($F = 450$ kN, $\phi_L = 10^\circ$) and ($F = 1200$ kN, $\phi_L = 15^\circ$), both with a zero angle α . The following geometrical and material parameters are generally considered in the case study:

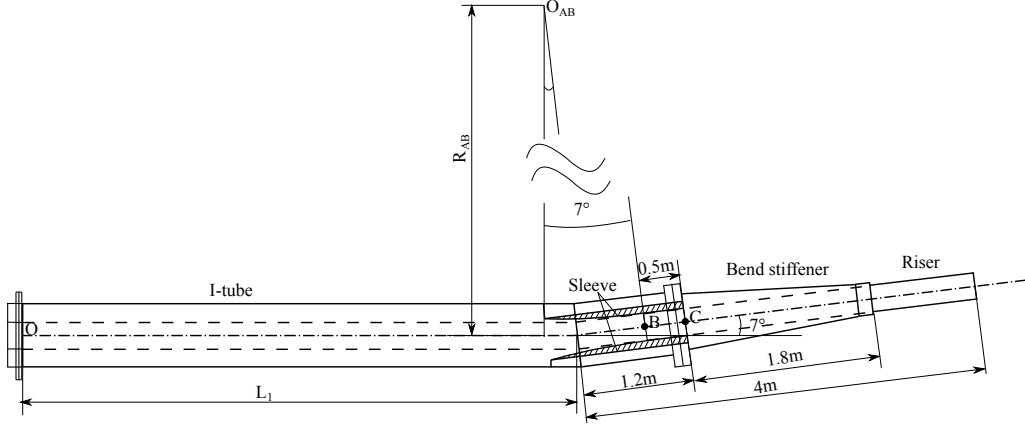


Figure 3.6: Riser-bend stiffener top connection with I-tube interface system schematic drawing.

- The riser bilinear bending behavior, presented in Eq. (3.4), is defined by the following parameters: $EI_{fs} = 40 \text{ kNm}^2$, $EI_{ns} = 2800 \text{ kNm}^2$ and $\kappa_{cr} = 0.002 \text{ m}^{-1}$ [69]. The flexible riser safely sustains a minimum bending radius (MBR) of 2 m or higher, equivalent to a maximum curvature of 0.5 m^{-1} .
- The nonlinear elastic model presented in Eq. (3.5) is employed for the bend stiffener polyurethane behavior with the following material parameters: $E_q = 20.19 \text{ MPa}$ and $q = 0.4738$. The bend stiffener geometrical parameters are shown in Fig. 3.7, consisting of a 1.65 m conical shape followed by a 0.15 m thin cylindrical tip. The riser/bend stiffener section length from bend stiffener top to riser tip is described by L_{CD} with a initial approximate straight length $L_{CD}^I=2.8 \text{ m}$. And the coordinates of point C are given by,

$$X_C = L_1 + 1.2 \cos \phi_0 \quad (3.29a)$$

$$Y_C = 1.2 \sin \phi_0 \quad (3.29b)$$

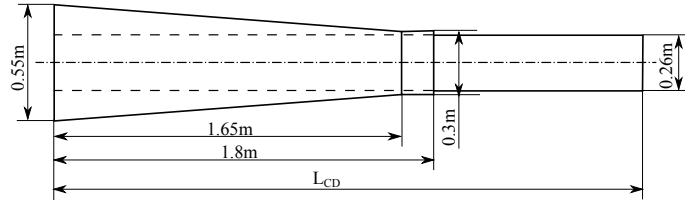


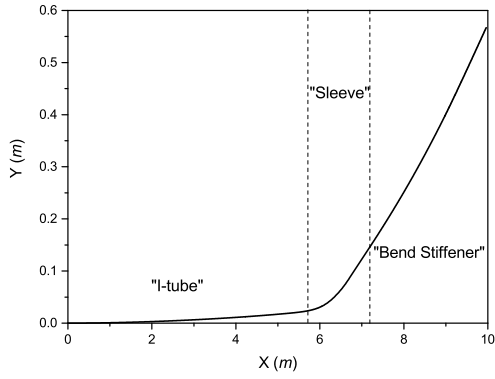
Figure 3.7: Geometry of the riser/bend stiffener section.

3.3.1 Large deflection assessment of top connection with I-tube interface

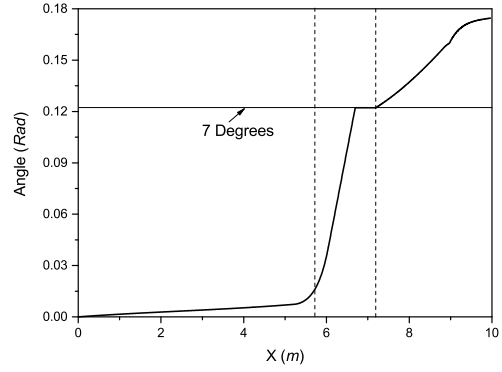
The riser-bend stiffener top connection response with I-tube interface is initially assessed considering an I-tube length of $L_1 = 6$ m and a sleeve curved section with a radius of $R_{AB} = 8$ m. The resulting configuration, angle, curvature, bending moment, shear force and axial force distribution along the X axis are presented in Fig. 3.8 and Fig. 3.9, for the two loading conditions (450 kN, 10°) and (1200 kN, 15°). The dotted lines define the coordinates of “I-tube”, “Sleeve” and “Bend stiffener” sections.

Figure 3.8a and Figure 3.9a show that the riser slightly deflects along the I-tube length up to the initial contact point with the sleeve, keeps contact with the sleeve following its shape, and continues the deflection attached to the bend stiffener, as no gap is considered. Along the riser/sleeve contact length, riser sustains a reaction force from sleeve in the initial contact point A and the shear force of riser drops to zero, and afterwards the moment of riser keeps constant following the curvature of sleeve curved section until the sleeve straight section starts with zero moment, which can be observed in the shear force and moment distribution in Figs. 3.8d-e and Figs. 3.9d-e. It can be seen in the curvature distribution in Fig. 3.8c and Fig. 3.9c that the riser is a stiffer structure below the critical curvature while its flexibility appears instantly after the critical point. The riser curvature, moment and shear force become zero passing through the sleeve straight section with the inclination 7° . For the dynamic extreme loading (1200 kN, 15°), the maximum curvature 0.19 m^{-1} in the bend stiffener root is higher than the sleeve curvature $\kappa_{AB} = 0.125$ m^{-1} . The maximum curvature along the riser/bend stiffener section appears in the bend stiffener tip with a curvature discontinuity for the static extreme loading (450 kN, 10°). Higher tension and rotation angle lead to the larger displacement and higher maximum curvature in the riser/bend stiffener section. The initial curvatures in the riser end fitting are 0.002 m^{-1} and 0.017 m^{-1} for the loading cases (450 kN, 10°) and (1200 kN, 15°) respectively. The bend stiffener sustains primarily the bending moment and shear force, and the tension is small along the length of bend stiffener.

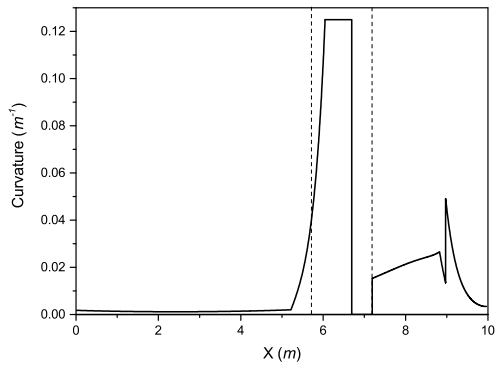
The contact force distributions along the riser/sleeve contact region and bend stiffener length for two loading conditions are shown in Fig. 3.10. The contact forces keep constant in the sleeve curved section and drop to zero in the straight sleeve section. The larger loading conditions result in a larger contact force in both the curved sleeve and riser/bend stiffener sections, as well as a longer contact length in the curved sleeve section. The location of the maximum contact force also changes with the loading conditions. For the larger loading conditions, the maximum contact force is located at the base of bend stiffener; for the smaller loading conditions, the



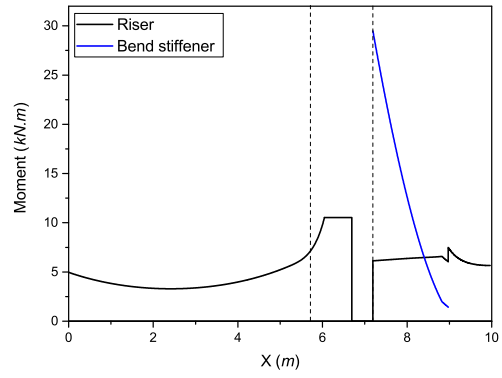
(a) Configuration



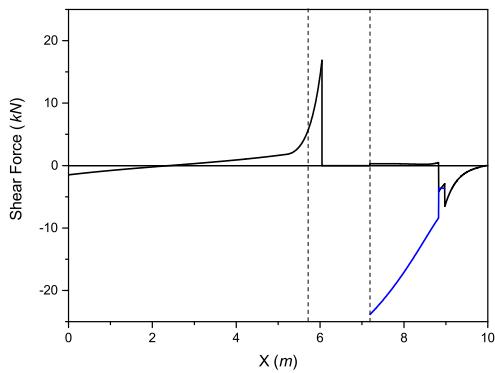
(b) Angle distribution



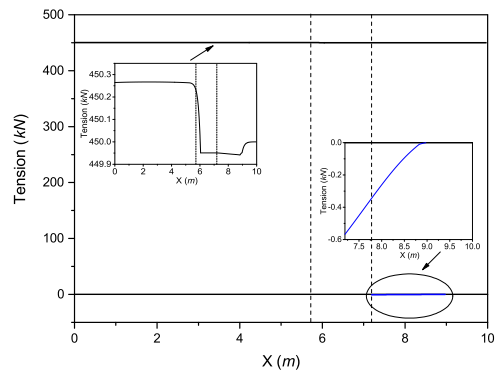
(c) Curvature distribution



(d) Moment distribution

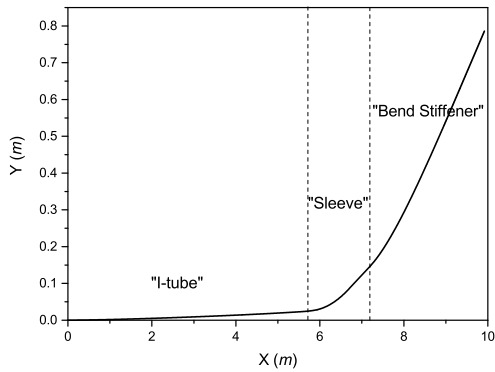


(e) Shear force distribution

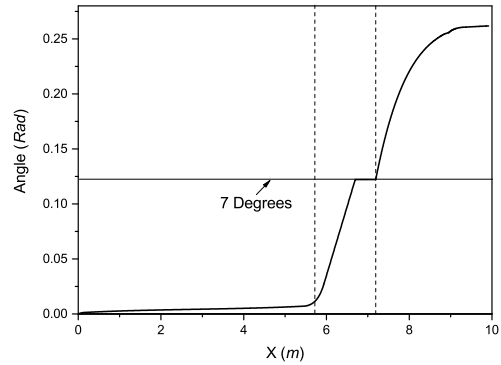


(f) Tension distribution

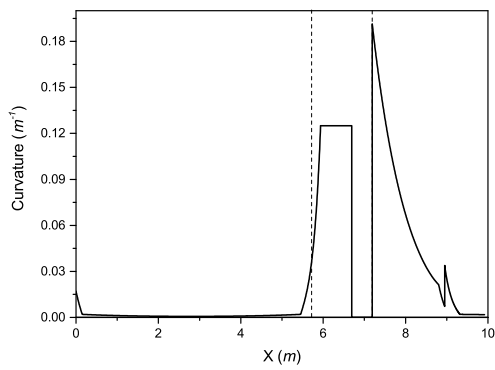
Figure 3.8: Top connection response for loading (450 kN, 10°): (a) Configuration; (b) Angle; (c) Curvature; (d) Bending moment; (e) Shear force and (f) Tension distributions.



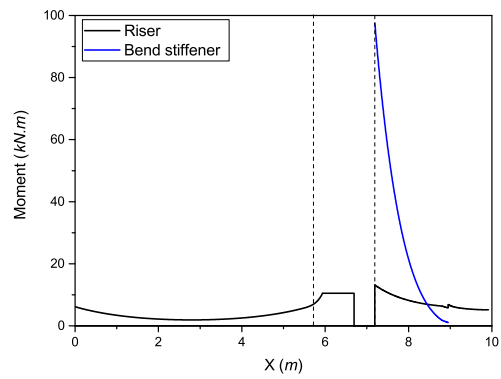
(a) Configuration



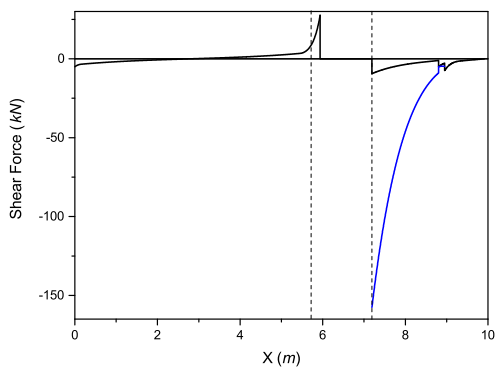
(b) Angle distribution



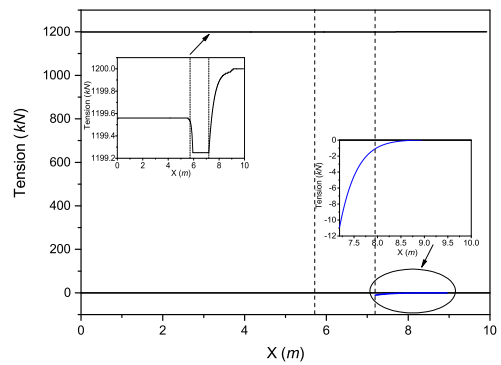
(c) Curvature distribution



(d) Moment distribution



(e) Shear force distribution



(f) Tension distribution

Figure 3.9: Top connection response for loading (1200 kN, 15°): (a) Configuration; (b) Angle; (c) Curvature; (d) Bending moment; (e) Shear force and (f) Tension distributions.

maximum contact force is located near the tip end of bend stiffener.

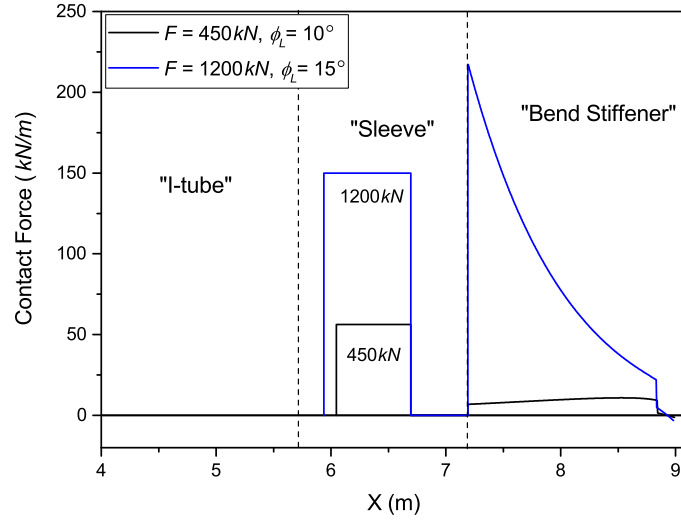


Figure 3.10: Contact force distribution along riser/sleeve and riser/bend stiffener sections.

3.3.2 Sleeve geometry influence

The sleeve geometry influence in the top connection system response subjected to loading conditions (450 kN, 10°) and (1200 kN, 15°) is assessed considering an I-tube length of $L_1 = 6$ m with the following sleeve geometrical parameters: i) Sleeve \mathcal{A} - straight section of 0.5 m without curved section; ii) Sleeve \mathcal{B} - straight section of 0.5 m + curved section with sleeve radius varying from $R_{AB} = 1, 2, \dots, 9, 10$ m.

The initial contact angle ϕ_A , the arc-length s_1 , the reaction force N_A , the riser end-fitting curvature κ_0 , the riser/bend stiffener section length variation ΔL_{CD} in relation to the initial length L_{CD}^I and the contact force f_{AB} along section AB are presented in Table 3.2 and Table 3.3, for both loading conditions, respectively. It can be observed that ϕ_A , s_1 , N_A , ΔL_{CD} and f_{AB} decrease as the sleeve radius increases. The tension T_A presents no variation with the sleeve radius and is given by 449.9 kN and 1199.2 kN for both load cases, respectively. The smallest radius results in the highest contact force between the riser and the sleeve. Figure 3.11 shows the initial contact angle ϕ_A and the end-fitting curvature κ_0 versus the sleeve radius R_{AB} for both load cases. For the end-fitting curvature, higher sleeve radius lead to smaller values of κ_0 for both loading conditions, which may be an important consideration for preliminary design purposes. In terms of the contact angle ϕ_A , it can be observed that as the sleeve radius decreases below a certain limit value, 1.6m for (1200 kN, 15°) and 2.6 m for (450 kN, 10°), the riser does not interact with the curved sleeve section and enters into direct contact with the straight section, that presents an inclination angle of 7°. Below this sleeve radius limit in sleeve \mathcal{B} ,

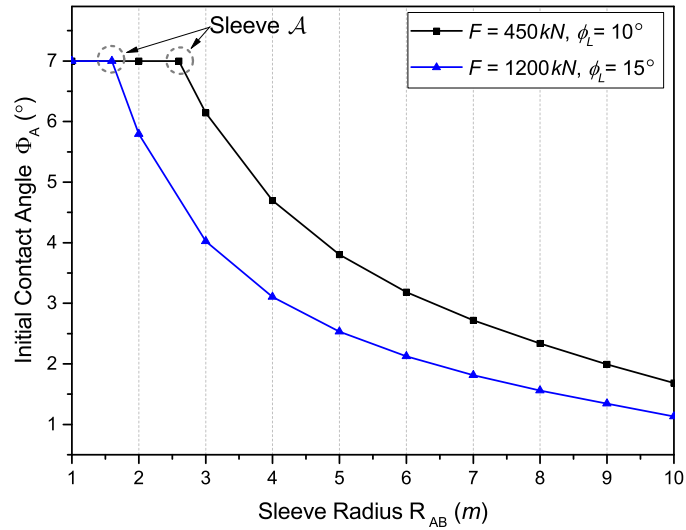
the riser curvature presents the highest values: 0.38 m^{-1} for $(450 \text{ kN}, 10^\circ)$ and 0.65 m^{-1} for $(1200 \text{ kN}, 15^\circ)$, observed in Fig. 3.12, as calculated for the straight sleeve configuration \mathcal{A} . The figure also presents the curvature distribution for other sleeve geometries ($R_{AB} = 4, 7$ and 10 m) where, as expected, higher sleeve radius lead to lower curvature values in the curved section followed by zero curvature in the 0.5 m straight section. It is important to highlight that the curvature distribution in the bend stiffer region is not affected by the sleeve geometry.

Table 3.2: Sleeve radius influence in the top connection response ($450 \text{ kN}, 10^\circ$)

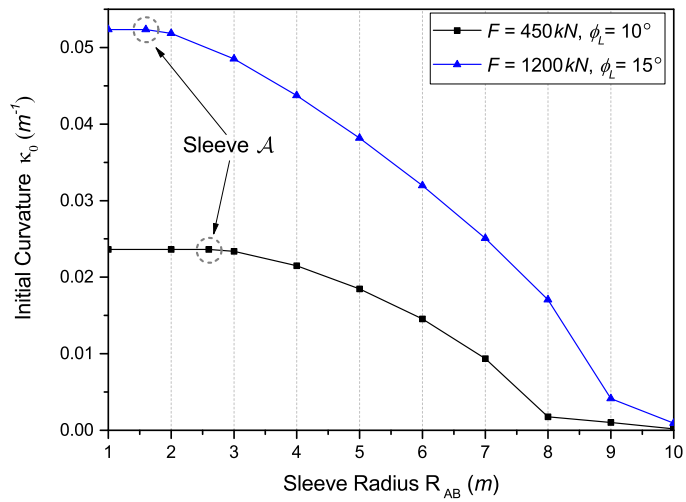
	Sleeve \mathcal{A}	R_{AB} (m) of sleeve \mathcal{B}							
	–	3	4	5	6	7	8	9	10
ϕ_A ($^\circ$)	7	6.14	4.70	3.80	3.18	2.72	2.34	1.99	1.68
s_1 (m)	6.69	6.65	6.54	6.42	6.30	6.17	6.05	5.91	5.77
κ_0 (m^{-1})	0.024	0.023	0.022	0.019	0.015	0.009	0.002	0.001	≈ 0
N_A (kN)	51.6	44.8	33.6	26.9	22.4	19.2	16.9	15.0	13.6
ΔL_{CD} (mm)	3.76	3.74	3.61	3.40	3.18	2.94	2.69	2.43	2.15
f_{AB} ($\frac{\text{kN}}{\text{m}}$)	–	150.0	112.5	90.0	75.0	64.3	56.2	50.0	45.0

Table 3.3: Sleeve radius influence in the top connection response ($1200 \text{ kN}, 15^\circ$)

	Sleeve \mathcal{A}	R_{AB} (m) of sleeve \mathcal{B}								
	–	2	3	4	5	6	7	8	9	10
ϕ_A ($^\circ$)	7	5.79	4.02	3.11	2.53	2.12	1.81	1.56	1.34	1.13
s_1 (m)	6.69	6.65	6.54	6.42	6.31	6.19	6.06	5.94	5.81	5.67
κ_0 (m^{-1})	0.052	0.052	0.049	0.044	0.038	0.032	0.025	0.017	0.004	≈ 0
N_A (kN)	135.1	109.7	73.1	54.9	43.9	36.7	31.5	27.6	24.6	22.2
ΔL_{CD} (mm)	4.12	4.10	3.93	3.71	3.48	3.24	2.98	2.71	2.44	2.16
f_{AB} ($\frac{\text{kN}}{\text{m}}$)	–	599.6	399.8	299.8	239.9	199.9	171.3	149.9	133.3	119.9

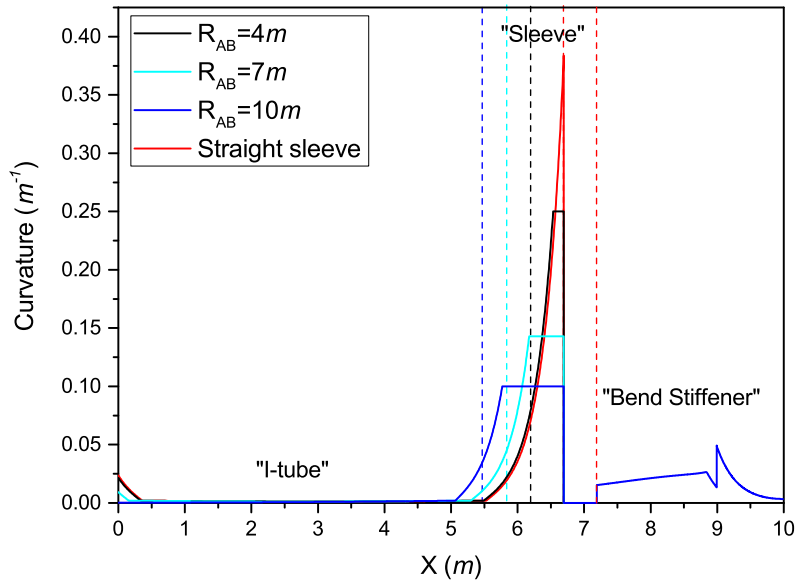


(a) Initial contact angle ϕ_A

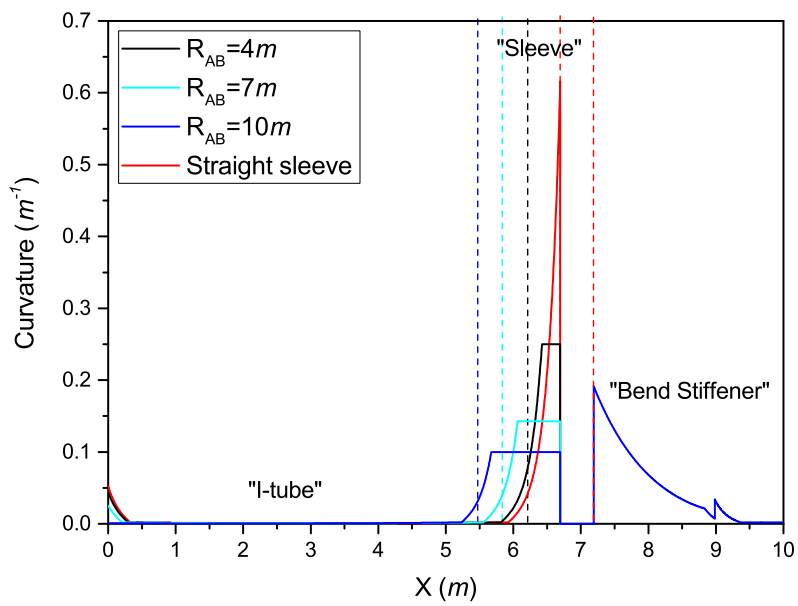


(b) End-fitting curvature κ_0

Figure 3.11: Initial contact angle and end-fitting curvature versus curved sleeve radius.



(a) $450kN, 10^\circ$



(b) $1200kN, 15^\circ$

Figure 3.12: Sleeve geometry influence in the curvature distribution.

3.3.3 I-tube length influence

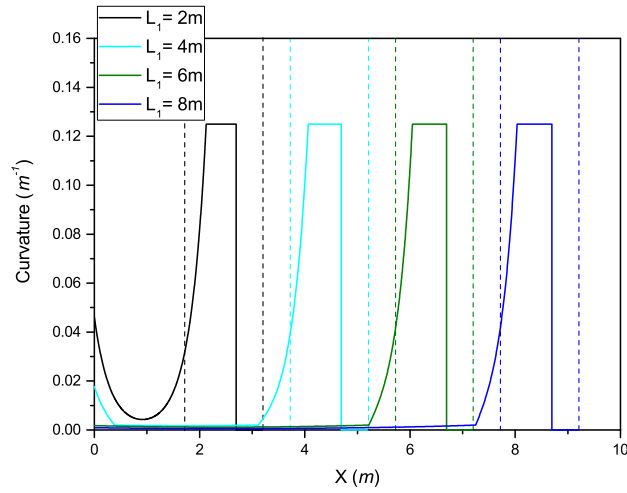
To investigate the I-tube length influence in the top connection system response, a sleeve geometry with a curved section radius given by $R_{AB} = 8$ m and a 0.5 m straight section is considered combined with the following values of I-tube lengths: $L_1 = 2, 3, 4, \dots, 8$ m. The same loading conditions employed in the previous section are used here. The initial contact angle ϕ_A , the arc-length s_1 , the reaction force N_A , the riser end-fitting curvature κ_0 and the riser/bend stiffener section length variation ΔL_{CD} in relation to the initial length L_{CD}^I are presented in Table 3.4 and Table 3.5. The length variation presents a small influence in the reaction force N_A and a slight increase in the relative sliding ΔL_{CD} is observed as the I-tube length increases. The tension T_A presents no variation with the I-tube length and is given by 449.9 kN and 1199.2 kN for both load cases, respectively. As there is no variation in the curvature and tension in the sleeve region, the contact force f_{AB} is constant and given by 56 kN/m and 150 kN/m for each load case, respectively. The flexible riser curvature distribution in the I-tube and sleeve region is presented in Fig. 3.13 for both loading conditions. A decrease in the length between the end-fitting and the riser initial contact point A with the sleeve leads to a larger curvature variation in the region, which is highlighted in Fig. 3.14, demonstrating that the end-fitting curvature κ_0 decreases as the I-tube length increases.

Table 3.4: I-tube length influence in the top connection response (450 kN, 10°)

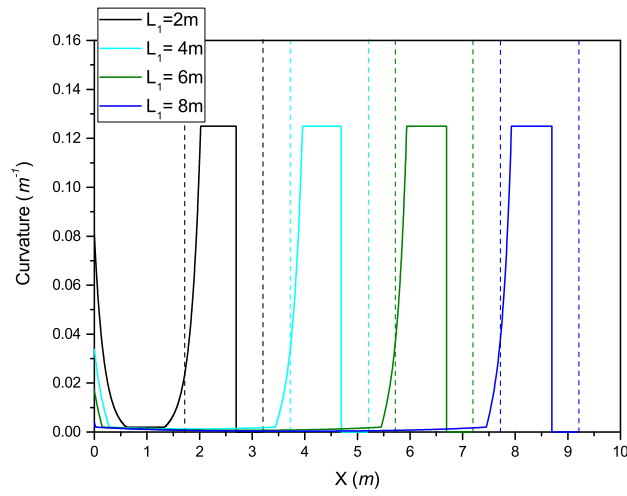
	L_1 (m)						
	2	3	4	5	6	7	8
ϕ_A ($^\circ$)	2.91	2.61	2.47	2.40	2.34	2.28	2.25
s_1 (m)	2.13	3.08	4.06	5.05	6.05	7.04	8.03
κ_0 (m^{-1})	0.046	0.027	0.018	0.010	0.002	0.001	≈ 0
N_A (kN)	16.76	16.78	16.81	16.84	16.87	16.89	16.91
ΔL_{CD} (mm)	2.55	2.62	2.66	2.67	2.69	2.70	2.70

Table 3.5: I-tube length influence in the top connection response (1200 kN, 15°)

	L_1 (m)						
	2	3	4	5	6	7	8
ϕ_A ($^\circ$)	2.16	1.84	1.69	1.61	1.56	1.52	1.50
s_1 (m)	2.02	2.98	3.96	4.94	5.94	6.93	7.93
κ_0 (m^{-1})	0.081	0.049	0.034	0.024	0.017	0.011	0.004
N_A (kN)	27.39	27.46	27.52	27.57	27.59	27.61	27.61
ΔL_{CD} (mm)	2.58	2.66	2.68	2.71	2.71	2.72	2.73



(a) 450 kN, 10°



(b) 1200 kN, 15°

Figure 3.13: I-tube length influence in the curvature distribution ($L_1 = 2, 4, 6, 8$ m).

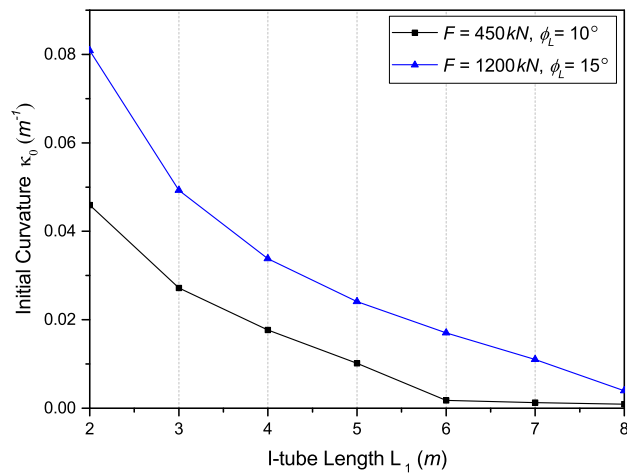


Figure 3.14: Initial curvature versus I-tube length (Curved sleeve radius $R_{AB} = 8$ m).

3.4 Conclusions

A large deflection beam formulation is developed for riser-bend stiffener top connection with I-tube interface. The end-fitting is assumed clamped in the I-tube top and the riser interacts with a straight rigid surface followed by a curved section in the bellmouth region. The riser and bend stiffener are assumed to have the same deflection as no gap is considered. The formulation incorporates the riser nonlinear bending behavior and nonlinear elastic bend stiffener polyurethane, and allows the calculation of the contact forces between the riser/sleeve and riser/bend stiffener sections. The mathematical formulation of the statically indeterminate system results in three systems of coupled differential equations combined with corresponding multipoint boundary conditions. An iterative numerical procedure has been presented and employed to solve the boundary value problem with the Mathematica package.

A case study is carried out with a 7" flexible riser protected by a 1.8 m bend stiffener connected to an I-tube with 7° inclination and subjected to extreme loading conditions. The results of large deflection assessment of riser top connection with I-tube interface were validated by a FEM model [69] in a complementary numerical study. A parametric assessment is performed to evaluate the influence of the sleeve shape and I-tube length on the riser curvature distribution. The following conclusions are obtained:

- i). The curvature distribution in the bend stiffener region is not affected by the sleeve geometry;
- ii). The end-fitting curvature is affected by both parameters, where, a) as the sleeve radius R_{AB} increases, the initial curvature k_0 decreases and, b) as the I-tube length L_1 is increased, the initial curvature decreases;
- iii). The sleeve radius not only controls the initial contact angle and curvature distribution in the contact region, but also that, below a given radius, the riser does not interact with the curved section but directly contact the straight sleeve region, which leads to a peak in the riser curvature;
- iv). The contact force between the riser and the sleeve is highly affected by its radius but is not influenced by the I-tube length.

Chapter 4

Inverse Problem Methodology in Riser/Bend Stiffener System

This chapter presents an inverse methodology for multiple parameter estimation in the riser/bend stiffener system. A simplified analytical riser/bend stiffener model based on the modeling analysis in Chapter 3 is considered in the inverse analysis when the bend stiffener material behavior and top tension are the unknown modeling uncertainties in the riser top connection system. If the bending behavior of riser in the I-tube region is required, the more detailed direct model of riser-bend stiffener top connection should be considered. A 4" flexible pipe protected by a 1.9 m bend stiffener, which has been adopted by several authors [16, 18, 24], is considered in this chapter. Section 4.1 describes the direct analytical model of riser/bend stiffener system. Section 4.2 presents an inverse parameter estimation methodology, which consists of the Levenberg-Marquardt algorithm, gyrometer monitoring rotation angles along the riser/bend stiffener length and a direct analytical model of riser/bend stiffener system. In Section 4.3, a case study of parameter estimations investigates the influences of the direct riser/bend stiffener model, number of sensors, sensor arrangement and loading conditions. Section 4.4 presents conclusions of this chapter.

4.1 Direct analytical model of riser/bend stiffener system

The analytical formulations of flexible riser-bend stiffener top connection are presented in Chapter 3, including the governing equations for the riser extended section, riser/bellmouth sleeve contact region and riser/bend stiffener section, which concludes the curvature distribution of riser in the bend stiffener region is not affected by the sleeve geometry. In the present inverse analysis work, the isolated riser/bend

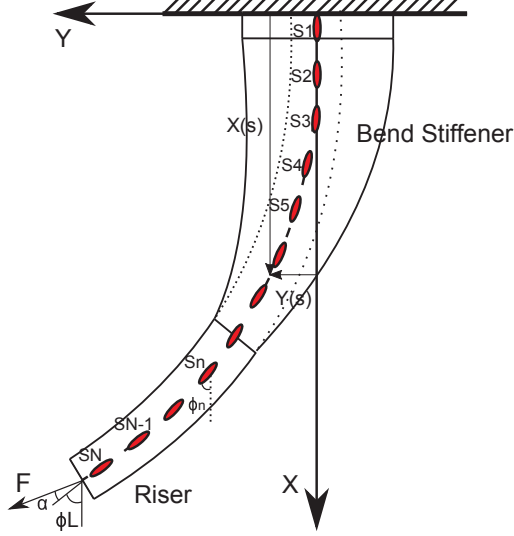


Figure 4.1: A bend stiffener system with N monitoring points.

stiffener analytical model is investigated considering the unknown polyurethane hyperelastic response and effective top tension. The riser and bend stiffener are clamped in the same top cross-section, and the initial inclination angle is disregarded. The riser/bend stiffener system with a total length of L is subjected to a top tension F with a angle α and a rotation angle ϕ_L , as schematically shown in Fig. 4.1.

Equation (3.17) and equation (3.1c) are decoupled from Eq. (3.1a) and Eq. (3.1b) and, consequently, can be solved independently. Introducing Eq. (3.1c) into Eq. (3.17) results in a second-order nonlinear differential equation for the angle:

$$\frac{d^2\phi}{ds^2} = -\frac{F \sin(\phi_L + \alpha - \phi) + E_q \left(\frac{d\phi}{ds}\right)^q \left(\frac{dI_{BS}}{ds}\right)}{EI_{riser} + E_q q \left(\frac{d\phi}{ds}\right)^{q-1} I_{BS}} \quad (4.1)$$

subjected to the following boundary conditions: $\phi(0) = 0$ and $\phi(L) = \phi_L$. Here, the formulation of riser/bend stiffener system only considers the full-slip bending stiffness $EI_{riser} = EI_{fs}$ of riser. For polyurethane linear elastic symmetric response, $q = 1$ and the stress-strain relation becomes $\sigma(\epsilon) = E_{BS}\epsilon$. The total bending moment vs curvature relation becomes $M = EI(s)\kappa$, with bending stiffness $EI(s) = EI_{fs} + EI_{BS}(s)$, and Eq. (4.1) is simplified into,

$$\frac{d^2\phi}{ds^2} = -\frac{1}{EI_{fs} + EI_{BS}} \left(F \sin(\phi_L + \alpha - \phi) + \frac{d\phi}{ds} \frac{dEI_{BS}}{ds} \right) \quad (4.2)$$

Equation (4.1) is solved by a central finite difference method with the arc-length $[0, L]$ divided into M subintervals ($\Delta s = L/M$) resulting in a system of $M-1$ non-

linear algebraic equations as follows,

$$\frac{\phi_{m+1} - 2\phi_m + \phi_{m-1}}{(\Delta s)^2} = - \frac{F \sin(\phi_L + \alpha - \phi_m) + E_q \left(\frac{\phi_{m+1} - \phi_{m-1}}{\Delta s} \right)^q \left(\frac{dI_{BS}(s_m)}{ds} \right)}{EI_{fs} + E_q q \left(\frac{\phi_{m+1} - \phi_{m-1}}{\Delta s} \right)^{q-1} I_{BS}(s_m)} \quad (4.3)$$

where $\phi_0 = 0$, $\phi_M = \phi_L$ and $s_m = (m - 1)\Delta s$ ($m = 1, 2, \dots, M - 1$). The numerical solution to the simultaneous system of $M - 1$ equations ($\phi_1, \phi_2, \dots, \phi_{M-1}$) is solved by the Mathematica [68] package with the FindRoot function.

4.2 Inverse parameter estimation methodology

Combining a direct riser/bend stiffener model and a set of angle measurements $((s_1, \psi_1), (s_2, \psi_2), \dots, (s_N, \psi_N))$ obtained by gyrometers installed along bend stiffener length, as schematically presented in Fig. 4.1, a number of model parameters P_j can be estimated through an iterative non-linear least squares minimization algorithm, observing that the total number of sensors N must be larger than the number of parameters j . In the present work, to assess the proposed methodology feasibility in retrieving uncertain data, the previously presented large deflection beam model in Section 4.1 is adopted to obtain the effective tension ($P_1 = F$) and the bend stiffener nonlinear elastic parameters ($P_2 = E_q$ and $P_3 = q$), employing numerically simulated gyrometer data.

4.2.1 Levenberg-Marquardt (L-M) methodology

The discrepancy between the numerically estimated angle distribution $\phi_i(F, E_q, q)$ and the data measured by the gyrometers ψ_i ($i = 1, \dots, N$), may be expressed by the summation of the squared residuals at N arc-length positions, as follows,

$$R(F, E_q, q) = \sum_{i=1}^N (\psi_i - \phi_i(F, E_q, q))^2 \quad (4.4)$$

By minimizing Eq. (4.4), it is possible to estimate the values of unknown parameters P_j that best match the model to the measurements. The equation can be generalized in matrix form, as follows,

$$R(\mathbf{P}) = [\mathbf{\Psi} - \mathbf{\Phi}(\mathbf{P})]^T [\mathbf{\Psi} - \mathbf{\Phi}(\mathbf{P})] \quad (4.5)$$

where the superscript T denotes the matrix transpose. $\mathbf{P}^T = [F, E_q, q]$, $\mathbf{\Psi}$ and $\mathbf{\Phi}$ are the vectors of unknown parameters, measured angles and estimated angles

respectively. To minimize the sum of squares $R(\mathbf{P})$, the gradient of $R(\mathbf{P})$ with respect to the vector of parameters \mathbf{P} equates to zero, consequently,

$$\Delta R(\mathbf{P}) = -2\mathbf{J}^T(\mathbf{P})[\Psi - \Phi(\mathbf{P})] = \mathbf{0} \quad (4.6)$$

where $\mathbf{J}(\mathbf{P})$ is the sensitivity matrix. The elements in the sensitivity matrix are called sensitivity coefficients and are defined as the first derivative of the estimated angle at the position s_i with respect to the unknown parameter P_j , as follows,

$$J_{ij} = \frac{\partial \Phi_i}{\partial P_j}, \quad (4.7)$$

$$i = 1, 2, \dots, N \quad \text{and} \quad j = 1, 2, 3$$

Linearizing the vector of estimated angles with a Taylor series expansion around the current solution \mathbf{P}^k at iteration k ,

$$\Phi(\mathbf{P}) = \Phi(\mathbf{P}^k) + \mathbf{J}^k[\mathbf{P} - \mathbf{P}^k] \quad (4.8)$$

where $\Phi(\mathbf{P}^k)$ and \mathbf{J}^k are the estimated angles and sensitivity matrix at iteration k respectively. Substituting Eq. (4.8) into Eq. (4.6) and incorporating a damping factor μ^k to improve the convergence behavior, the following iterative procedure is obtained to estimate the vector of unknown parameters, known as the Levenberg-Marquardt (L-M) method [49],

$$\mathbf{P}^{k+1} = \mathbf{P}^k + [(\mathbf{J}^k)^T \mathbf{J}^k + \mu^k \Omega^k]^{-1} (\mathbf{J}^k)^T [\Psi - \Phi(\mathbf{P}^k)] \quad (4.9)$$

where $\Omega^k = \text{diag}[(\mathbf{J}^k)^T \mathbf{J}^k]$ is a diagonal matrix. The value of damping factor μ^k is then reduced gradually as the iteratively estimated parameters advance to the convergent estimations. The following stopping criterion is employed to terminate the iterative L-M procedure,

$$\left| \frac{P_j^{k+1} - P_j^k}{P_j^k} \right| < \epsilon \quad \text{and} \quad j = 1, 2, 3 \quad (4.10)$$

where ϵ are tolerances from the field application, here it is assumed 10^{-8} .

4.2.2 Computational Algorithm

The L-M algorithm for the parameter estimations in riser/bend stiffener system is presented in the flowchart of Fig. 4.2. In the first step, the initial unknown parameters \mathbf{P}^0 could be any set of reasonable values, and the initial damping factor is set to $\mu^0 = 0.001$ [49]. The numerical model estimated angles $\Phi(\mathbf{P}^k)$ are obtained

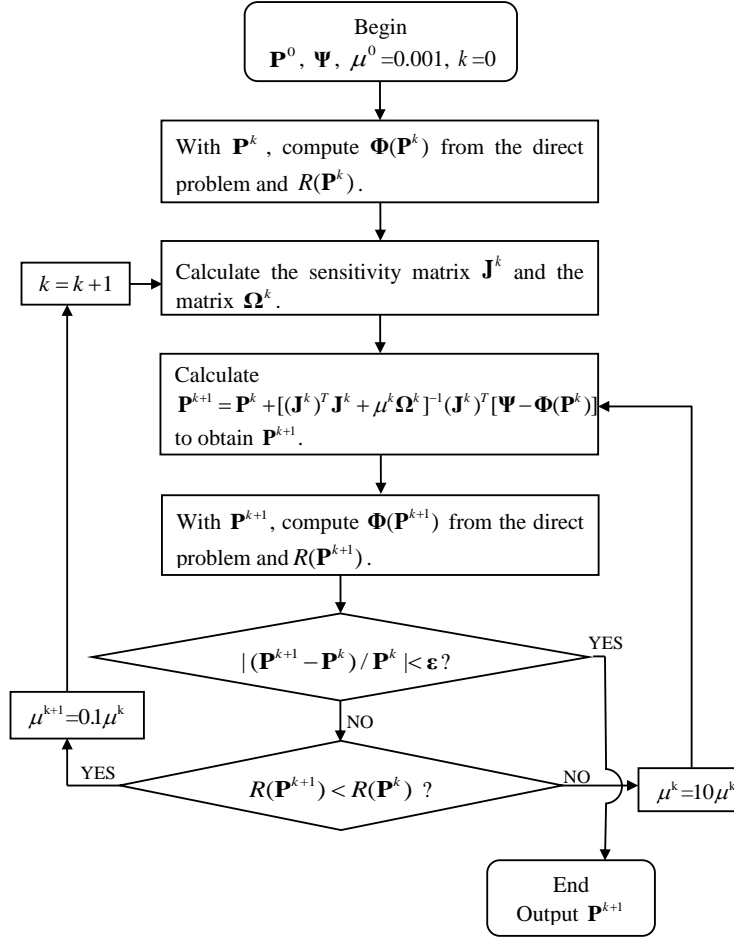


Figure 4.2: Flowchart of Levenberg-Marquardt computational algorithm.

at measurement locations by using the current estimations \mathbf{P}^k . The sensitivity coefficients can then be numerically computed by central finite differences [49],

$$\begin{aligned}
 J_{i1}^k &\cong \frac{\phi_i(P_1^k + \beta P_1^k, P_2^k, P_3^k) - \phi_i(P_1^k - \beta P_1^k, P_2^k, P_3^k)}{2\beta P_1^k}, \\
 J_{i2}^k &\cong \frac{\phi_i(P_1^k, P_2^k + \beta P_2^k, P_3^k) - \phi_i(P_1^k, P_2^k - \beta P_2^k, P_3^k)}{2\beta P_2^k}, \\
 J_{i3}^k &\cong \frac{\phi_i(P_1^k, P_2^k, P_3^k + \beta P_3^k) - \phi_i(P_1^k, P_2^k, P_3^k - \beta P_3^k)}{2\beta P_3^k},
 \end{aligned} \tag{4.11}$$

and $i = 1, 2, \dots, N$

where the small correction coefficient $\beta = 10^{-4}$, which does not influence the convergent estimated results but affect the number of iterations.

In the iteration step k , check the stopping criteria, and stop the iterative procedure if criteria are satisfied, or compare $R(\mathbf{P}^{k+1})$ with $R(\mathbf{P}^k)$. If $R(\mathbf{P}^{k+1}) \geq R(\mathbf{P}^k)$, enter into a subpath for iterative k and replace μ^k by $10\mu^k$, and recalculate \mathbf{P}^{k+1} , $\Phi(\mathbf{P}^{k+1})$, and $R(\mathbf{P}^{k+1})$ again until $R(\mathbf{P}^{k+1}) < R(\mathbf{P}^k)$. And then accept the new estimated \mathbf{P}^{k+1} and replace μ^k by $0.1\mu^k$ and go to iteration step $k + 1$. The itera-

tions vary in each estimation program according to the measurement errors and the initial guesses of unknown parameters, and the maximum number of iterations is chosen to be 50 in the loop, which is found to be sufficient for the problem.

The choice of damping factor in the subpath of each iteration guarantees the summation of squared residuals keep decreasing during the whole iterative process. In the beginning of iterations, the L-M method tends to be the Steepest Descent method with relative larger $\mu^k \Omega^k$, that is, a very small step is taken in the negative gradient direction. The parameter μ^k is then gradually reduced as the iteration procedure advances to the solution of parameter estimation, and then the L-M method tends to be the Gauss method. The L-M algorithm has its advantage of the local convergence comparing with the Gauss algorithm.

4.3 Case Study

A 4" flexible pipe protected by a 1.9 m long bend stiffener is employed in the present case study, as previously adopted by Vaz et al. [16]. The geometric parameters of the riser/bend stiffener are shown in Fig. 4.3. The riser bending stiffness is assumed constant and given by $EI_{fs} = 10 \text{ kNm}^2$. The applied top tension F varies from 62.5 to 500 kN and the tip angle ϕ_L from 0.5° to 30° with $\alpha = 0$ to encompass a large range of loading conditions. The following analyses are carried out to investigate the influences of the number of sensors (up to $N = 9$), sensor distribution along length, loading condition and top connection model on the inverse calculation of top tension and bend stiffener material parameters (the subscript e stands for *estimated*):

- a. Inverse calculation of top tension F_e^{LE} and Young's modulus E_e^{LE} based on simulated gyrometer data and linear elastic model ($F = 125, 500 \text{ kN}$, $\phi_L = 10^\circ$).
- b. Inverse calculation of top tension F_e^{NLE} and material parameters $E_{q,e}^{NLE}$, q_e^{NLE} based on simulated gyrometer data and nonlinear elastic model:
 - (i). gyrometer arrangement assessment for a selected load case ($F = 125 \text{ kN}$, $\phi_L = 10^\circ$);
 - (ii). top tension ($F = 62.5, 125, 250, 500 \text{ kN}$, $\phi_L = 10^\circ$) parametric assessment with 4 sensors;
 - (iii). tip angle ($\phi_L = 2, 3, 4, 5, 6, 8, 10, \dots, 28, 30^\circ$, $F = 125 \text{ kN}$) parametric assessment with 4 sensors;

- (iv). tip angle ($\phi_L = 2, 3, 4, 5^\circ$, $F = 125$ kN) parametric assessment with 9 sensors;
- (v). tip angle ($\phi_L = 0.5, 1, 1.5, 2^\circ$, $F = 125$ kN) parametric assessment with 4 sensors and considering known material properties.

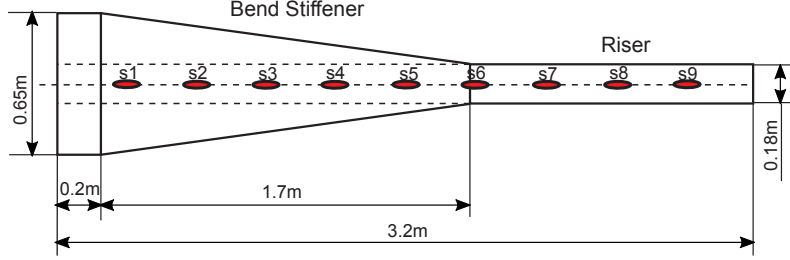


Figure 4.3: Geometric parameters of the bend stiffener system with nine sensors.

4.3.1 Gyrometer data - numerical simulation procedure

In this preliminary investigation of the proposed monitoring approach, the gyrometer data $\psi_i(s_i)$ is simulated at N points along top connection arc-length ($i = 1, 2, \dots, N$) by adding random errors to numerically calculated angles $\phi_i(s_i, F, E_q, q)$ with a set of specified parameters, as follows,

$$\begin{aligned} \psi_i &= \phi_i(s_i, F, E_q, q) + \delta e_i \\ i &= 1, 2, \dots, N \end{aligned} \quad (4.12)$$

where δ is the sensor precision, assumed to be the same for all positions, and e_i is a random variable with standard normal distribution in which 99% of probability lies in the range $-2.576 < e_i < 2.576$. For the present case study, it is assumed $\delta = 0.0002$ rad, as previously described by sensor noise of gyrometers employed in offshore applications [43]. The nonlinear elastic material parameters $E_q = 20.19$ MPa and $q = 0.4738$, as shown in Fig. 3.3, are employed for the data generation.

As the simulated sensor data contain random errors, the Monte Carlo approach is adopted in all the subsequent simulations. For each sensor position i , 200 different values of e_i are randomly generated and, consequently, the unknown parameters must be estimated 200 times for each analysis.

4.3.2 Inverse method based on linear elastic model

The first investigation consists in generating the sensor data $\psi_i(s_i)$ with the nonlinear elastic model given by Eq. (4.1), as described in the previous section, for two loading

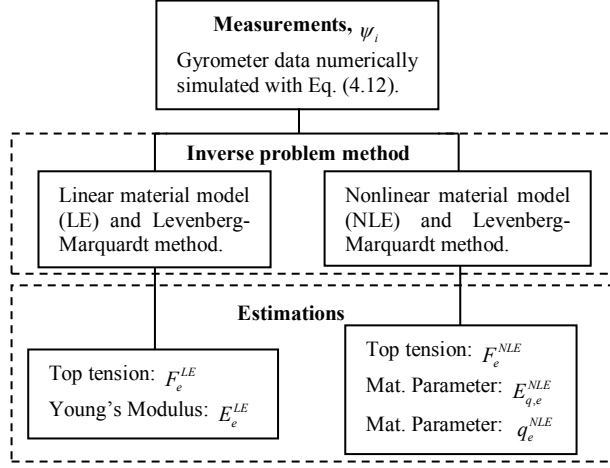


Figure 4.4: Parameters estimation procedure for the riser/bend stiffener system.

Table 4.1: The mean and standard deviation values of top tension F_e and Young's modulus E_e estimation by linear material model for two loading cases ($F = 125, 500$ kN, $\phi_L = 10^\circ$)

Load	125 kN		500 kN	
	Estimation	Error(%)	Estimation	Error(%)
\bar{F}_e^{LE} (kN)	172.4	[33.1,44.5]	530.4	[-4.0,18.9]
$\sigma_{F,e}$ (kN)	2.2	-	22.0	-
\bar{E}_e^{LE} (MPa)	463.6	-	232.4	-
$\sigma_{E,e}$ (MPa)	6.3	-	9.7	-

conditions ($F = 125, 500$ kN, $\phi_L = 10^\circ$) and with nine ($N = 9$) sensor positions (0.32, 0.64, 0.96, 1.28, 1.60, 1.92, 2.24, 2.56, 2.88 m). The linear elastic model described by Eq. (4.2) is then applied in the inverse estimation of the top tension F_e^{LE} and Young's modulus E_e^{LE} , as summarized in the flowchart presented in Fig. 4.4.

The mean and standard deviation values of estimated top tension F_e and Young's modulus E_e and the top tension errors, given by $[(F_e^{min} - F)/F, (F_e^{max} - F)/F]$, are presented in Table 4.1. A larger top tension variation range of [33.1%, 44.5%] is observed for the smaller loading magnitude, $F = 125$ kN. The nominal stress vs nominal strain (up to 2%) of the nonlinear elastic response, adopted for sensor data generation, and the envelope of the estimated Young's modulus are presented in Fig. 4.5. The envelope is defined by the maximum and minimum parameter values obtained from the Monte Carlo simulations performed with 200 samples. It can be observed that a stiffer polyurethane is obtained for the lower loading case, with a very large variation between the two estimations.

As the sensor data is numerically generated with the nonlinear elastic model, a direct comparison between the “exact” angle and curvature distributions can be made with the inverse method results. Figures 4.6, 4.7 and 4.8 present the angle, curvature and maximum strain envelope distributions along arc-length, respectively. Larger differences between the direct model and inverse calculations are observed for $F = 125$ kN, as anticipated from the results presented in Table 4.1. It can also be observed in Fig. 4.8 that, as the estimated maximum bend stiffener strain increases, the deviation from the “exact” nonlinear model tends to increase, which is in agreement with the stress vs strain curve presented in Fig. 4.5.

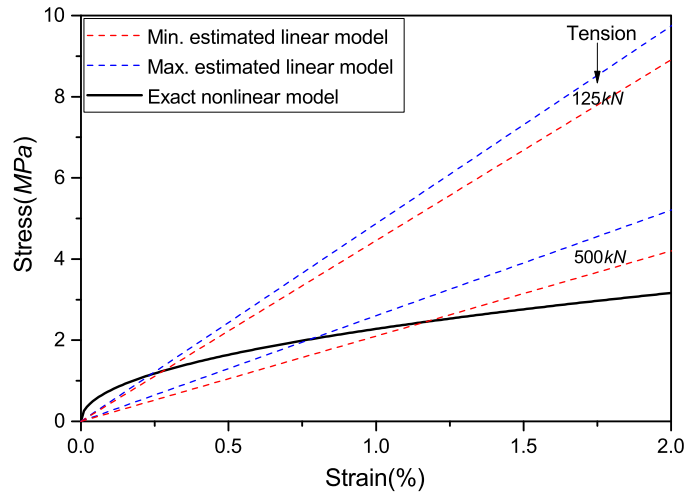


Figure 4.5: Nominal stress vs. nominal strain of nonlinear elastic model and inverse method calculation envelope (simulated sensor data + linear elastic model) of Young’s modulus for two loading conditions ($F = 125, 500$ kN, $\phi_L=10^\circ$).

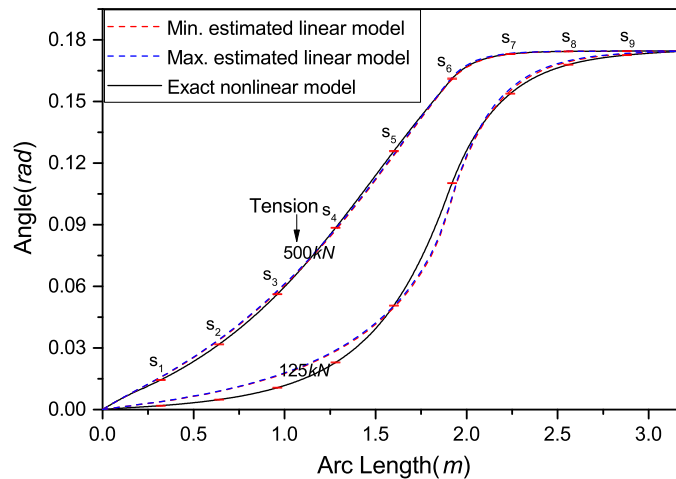


Figure 4.6: Angle distribution of nonlinear elastic model and inverse method calculation envelope (simulated sensor data + linear elastic model) for two loading conditions ($F = 125, 500$ kN, $\phi_L=10^\circ$).

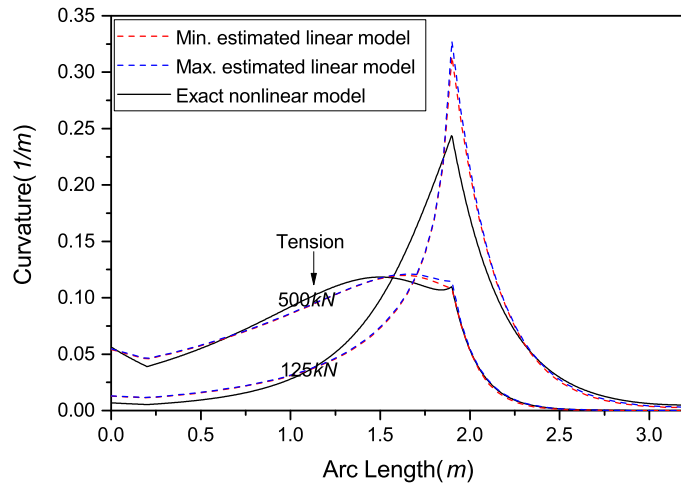


Figure 4.7: Curvature distribution of nonlinear elastic model and inverse method calculation envelope (simulated sensor data + linear elastic model) for two loading conditions ($F = 125, 500 \text{ kN}$, $\phi_L = 10^\circ$).

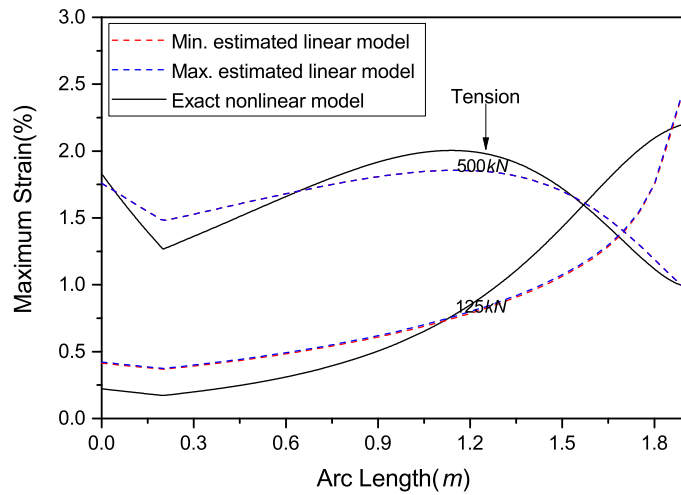


Figure 4.8: Maximum strain distribution of nonlinear elastic model and inverse method calculation envelope (simulated sensor data + linear elastic model) for two loading conditions ($F = 125, 500 \text{ kN}$, $\phi_L = 10^\circ$).

4.3.3 Inverse method based on nonlinear elastic model

For all the subsequent analyses, the nonlinear elastic model is employed for the inverse parameter estimation. The effect of different sensor arrangements is initially investigated, followed by the assessment of loading condition influence on the inverse estimation of F_e^{NLE} , $E_{q,e}^{NLE}$ and q_e^{NLE} .

Gyrometer arrangement assessment

A 125 kN top tension with a tip angle of 10° is defined as the reference load case in this section. The angle along arc-length varies from a small value close to encastre to a maximum value at tip, where its distribution depends on the loading condition and system properties. As a consequence, the sensor arrangement has a direct impact in the inverse methodology. In order to assess the influence that the number of sensors and positioning have on the inverse parameters estimation, five arrangements are investigated (A1-3 sensors (s_6 - s_8), A2-3 sensors (s_4 - s_6), A3-4 sensors (s_3 - s_6), A4-5 sensors (s_3 - s_7), A5-9 sensors (s_1 - s_9)) with the number of sensors N ranging from 3 to 9, as described in Table 4.2.

The L-M sensitivity coefficients, defined in Eq. (4.7), may be employed to support the most efficient sensor positioning in terms of inverse method application. The sensitivity matrix J_{ij} ($i = 1, 2, \dots, 9$, and $j = 1, 2, 3$) is presented in Table 4.2 for the present load case, where it can be observed that the locations s_3 to s_7 are more sensitive than s_1 , s_2 , s_8 , and the location s_9 has the smallest values.

Table 4.3 presents the influence that the arrangement has on the mean and standard deviation values of estimated top tension and material parameters. The parameters errors are also presented, being defined by $[(P_{j,e}^{min} - P_j)/P_j, (P_{j,e}^{max} - P_j)/P_j]$ ($j = 1, 2, 3$). It can be observed, as expected, that the higher the number of sensors the lower is the standard deviation and the deviation from the “exact” value. Higher values of sensitivity coefficients indicate the best position for sensor installation, which can be observed, for example, by comparing arrangements A1 and A2. For the arrangement A1, where all the sensors are placed in the riser segment, the sensitivity coefficients present lower magnitudes values and as a consequence, the estimation accuracy is lower.

The probability distribution of the estimated parameters F_e^{NLE} , $E_{q,e}^{NLE}$ and q_e^{NLE} are shown in Figs. 4.9, 4.10 and 4.11, respectively, for two sensor arrangements (A3, A5). When 9 sensors are employed, the distributions are more concentrated around the exact values, which is also confirmed by the stress vs strain envelope results presented in Fig. 4.12.

Table 4.2: Sensor arrangement definition and sensitivity coefficient matrix ($F=125\text{kN}$, $\phi_L=10^\circ$)

	s_1 (0.32m)	s_2 (0.64m)	s_3 (0.96m)	s_4 (1.28m)	s_5 (1.60m)	s_6 (1.92m)	s_7 (2.24m)	s_8 (2.56m)	s_9 (2.88m)
$J_{i1} \times 10^7$ (rad/N)	0.254	0.614	1.242	2.313	3.728	3.774	2.138	0.967	0.352
$J_{i2} \times 10^9$ (rad/Pa)	-0.163	-0.397	-0.814	-1.545	-2.526	-1.953	-0.630	-0.201	-0.059
J_{i3}	0.023	0.055	0.107	0.186	0.272	0.193	0.062	0.020	0.006
A1	—	—	—	—	—	s_6	s_7	s_8	—
A2	—	—	—	s_4	s_5	s_6	—	—	—
A3	—	—	s_3	s_4	s_5	s_6	—	—	—
A4	—	—	s_3	s_4	s_5	s_6	s_7	—	—
A5	s_1	s_2	s_3	s_4	s_5	s_6	s_7	s_8	s_9

Table 4.3: Sensor arrangement effect on the mean and standard deviation values of estimated top tension and material parameters ($F = 125 \text{ kN}$, $\phi_L=10^\circ$, $E_q=20.19\text{MPa}$ and $q=0.4738$)

	F_e^{NLE} $\bar{F}_e^{NLE}, \sigma_{F,e}, Error$ (kN),(kN), (%)			$E_{q,e}^{NLE}$ $\bar{E}_{q,e}^{NLE}, \sigma_{E_{q,e}}, Error$ (MPa),(MPa), (%)			q_e^{NLE} $\bar{q}_e^{NLE}, \sigma_{q,e}, Error$ (%)		
A1	124.9,	2.0,	[-4.4, 4.3]	17.46,	0.19,	[-16.0, -10.9]	0.4441,	0.0020,	[-7.4, -5.1]
A2	124.9,	3.9,	[-8.7, 9.6]	20.20,	1.73,	[-20.1, 30.5]	0.4733,	0.0110,	[-5.8, 7.2]
A3	124.9,	3.4,	[-8.7, 6.9]	20.12,	1.29,	[-17.6, 16.9]	0.4729,	0.0080,	[-4.8, 4.5]
A4	124.8,	1.8,	[-3.5, 3.1]	20.15,	0.96,	[-11.5, 13.9]	0.4734,	0.0074,	[-3.9, 4.1]
A5	125.1,	1.6,	[-3.4, 3.6]	20.23,	0.85,	[-11.2, 12.9]	0.4738,	0.0062,	[-3.8, 3.5]

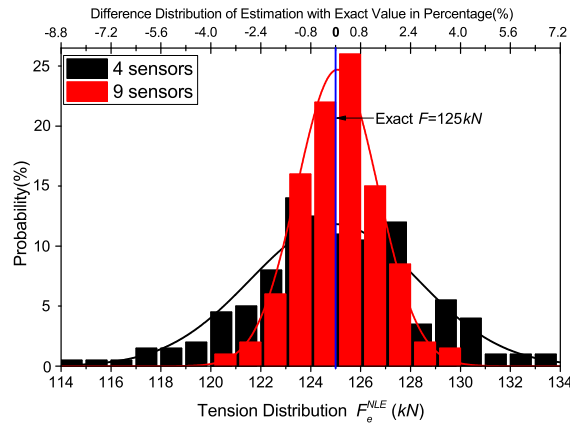


Figure 4.9: Probability distribution of estimated top tension F_e^{NLE} for arrangements A3 and A5.

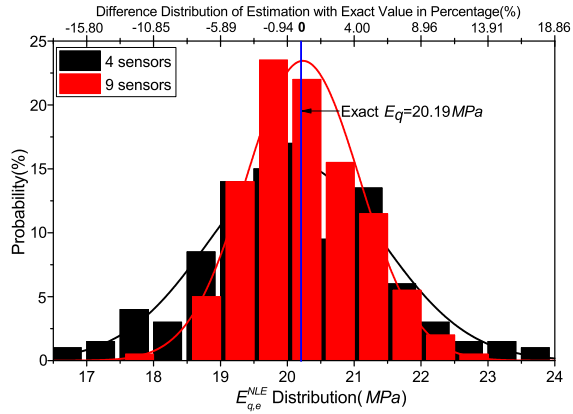


Figure 4.10: Probability distribution of material parameter $E_{q,e}^{NLE}$ for arrangements A3 and A5.

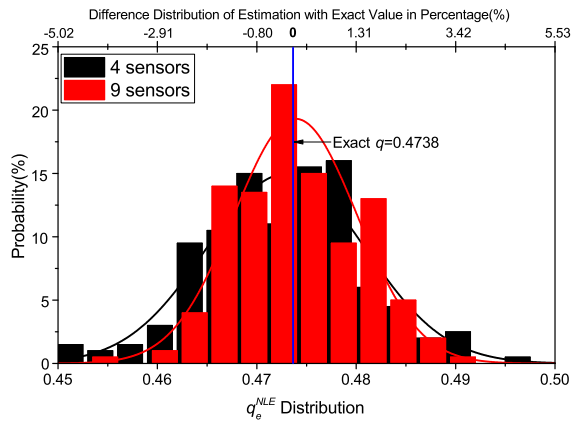


Figure 4.11: Probability distribution of material parameter q_e^{NLE} for arrangements A3 and A5.

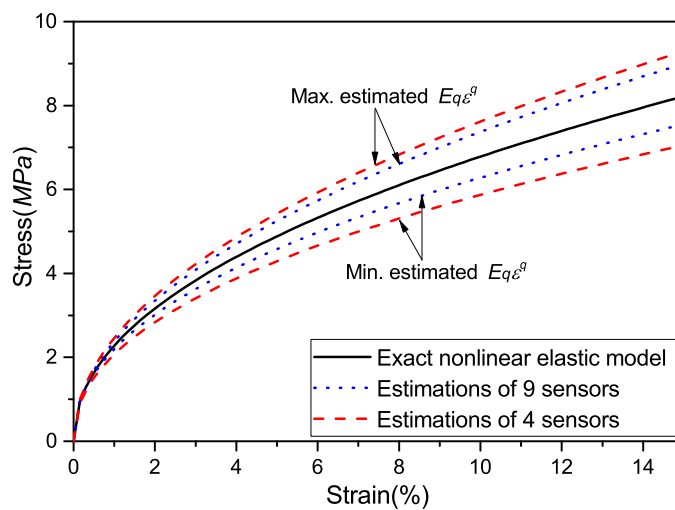


Figure 4.12: Estimated material curve envelope for arrangements A3 and A5.

Top tension parametric assessment with 4 sensors (arrangement A3)

The sensor arrangement A3, with 4 sensors, is selected to investigate the effect of four applied top tensions (62.5, 125, 250, and 500 kN, $\phi_L=10^\circ$) on the inverse parameters estimation.

The top tension effect on the sensitivity coefficients is presented in Fig. 4.13. It is observed that top tension variation presents a larger influence on the force sensitivity coefficient J_F after bend stiffener termination. For the material parameters, the largest values occur around $s = 1.6$ m. Table 4.4 presents the top tension effect on the mean and standard deviation values of estimated top tension and material parameters. The increase in top tension standard deviation follows the increase in the loading application. For the material parameters, it can be observed that the smallest standard deviation values occur for the $F = 125$ kN loading case.

The angle and curvature envelope distributions are respectively presented in Figs. 4.14 and 4.15 for two loading cases ($F = 125, 500$ kN). A very good correlation with the “exact” distribution is observed. Figure 4.14 also presents the sensor error range resulting from the Monte Carlo simulation with 200 values of e_i (see Eq. (4.12)) and the “exact” angle distribution for all the cases.

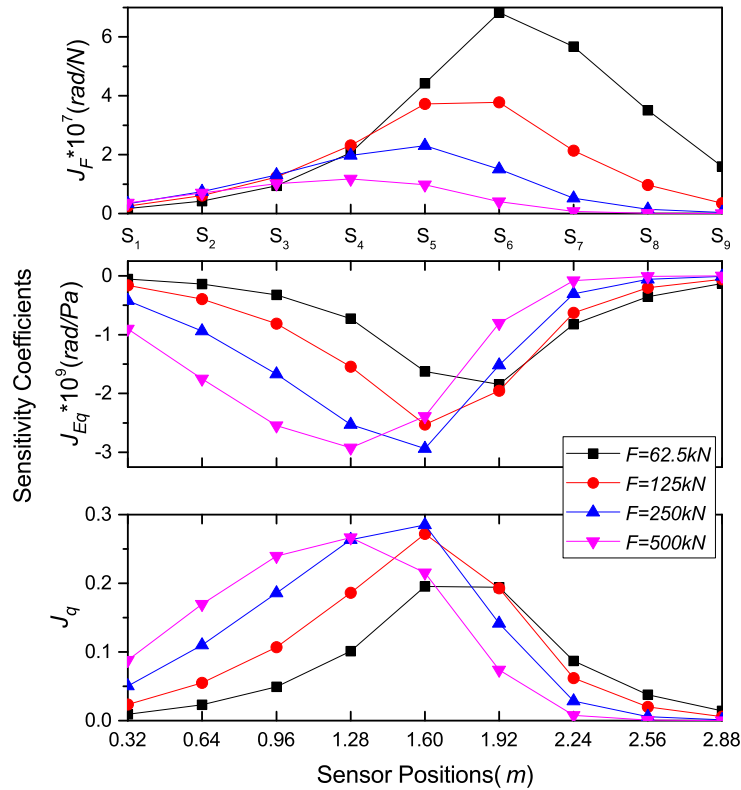


Figure 4.13: Top tension influence on the sensitivity coefficients ($\phi_L=10^\circ$).

Table 4.4: Top tension influence on the mean and standard deviation values of estimated top tension and material parameters ($\phi_L=10^\circ$) with 4 sensors (A3)

Load	62.5 kN	125 kN	250 kN	500 kN
\bar{F}_e^{NLE} (kN)	63.0	124.9	250.4	500.8
$\sigma_{F,e}$ (kN)	2.7	3.4	7.1	23.1
$\bar{E}_{q,e}^{NLE}$ (MPa)	20.68	20.12	20.23	20.31
$\sigma_{E_{q,e}}$ (MPa)	2.25	1.29	1.39	2.96
\bar{q}_e^{NLE}	0.4758	0.4729	0.4734	0.4728
$\sigma_{q,e}$	0.0122	0.0080	0.0096	0.0277

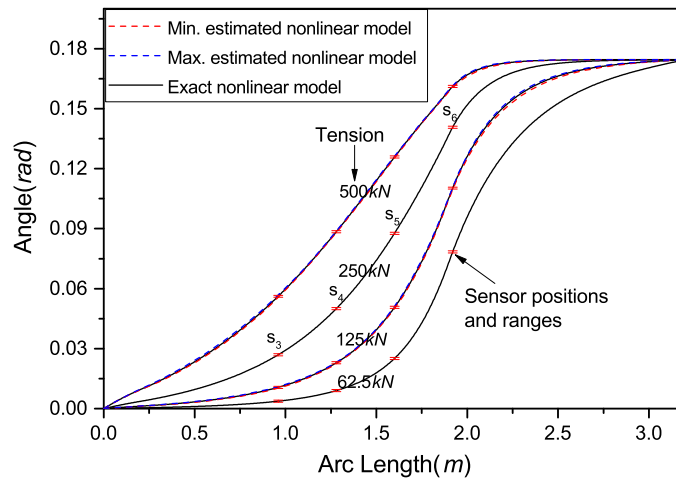


Figure 4.14: Angle distribution of nonlinear elastic model, sensors range and inverse method calculation envelope (simulated sensor data + nonlinear elastic model) with 4 sensors (A3) for two loading conditions ($F = 125, 500$ kN, $\phi_L=10^\circ$).

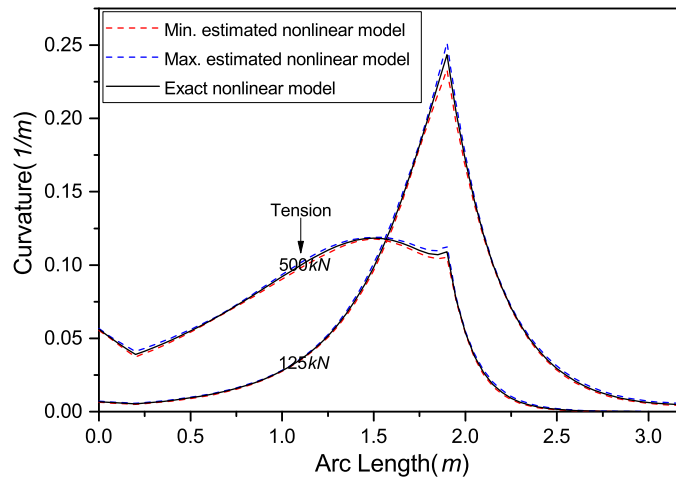


Figure 4.15: Curvature distribution of nonlinear elastic model and inverse method calculation envelope (simulated sensor data + nonlinear elastic model) with 4 sensors (A3) for two loading conditions ($F = 125, 500$ kN, $\phi_L=10^\circ$).

Tip angle parametric assessment with 4 sensors (arrangement A3)

The sensor arrangement A3 with 4 sensors is now employed to investigate the effect of a range of boundary end angles ($2, 3, 4, 5, 6, 8, 10, \dots, 28, 30^\circ$, $F = 125$ kN) on the inverse parameters estimation. The tip angle effect on the sensitivity coefficients is presented in Fig. 4.16. A gradual distribution decrease can be observed by reducing the tip angle, with a higher gradient in the middle position, for both top tension and material parameters coefficients.

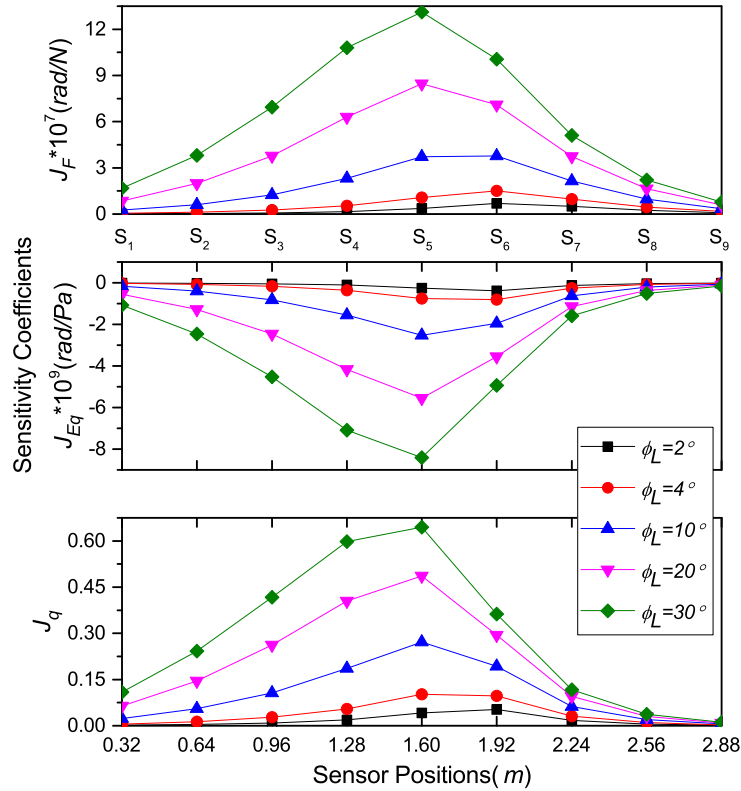


Figure 4.16: Tip angle influence ($\phi_L = 2, 4, 10, 20, 30^\circ$) on the sensitivity coefficients ($F = 125$ kN).

The influence that the tip angle has on angle and curvature envelope distributions are respectively presented in Figs. 4.17 and 4.18 for two loading cases ($\phi_L = 2, 30^\circ$, $F = 125$ kN). The sensor error range resulting from the Monte Carlo simulation with 200 values of e_i is also presented in Fig. 4.17. A significant distribution variation is observed for the smallest value of tip angle adopted ($\phi_L = 2^\circ$), with the highest difference occurring in the maximum curvature position. For the angle $\phi_L = 30^\circ$, a very good correlation is obtained.

The tip angle effect on the mean and standard deviation values of estimated top tension and material parameters are presented in Figs. 4.19, 4.20 and 4.21 for F_e^{NLE} , $E_{q,e}^{NLE}$ and q_e^{NLE} , respectively. A large increase in the standard deviation values for all parameters can be observed for tip angles below 10° . It is concluded that the estimations using 4 sensors are good for large tip angles, but imprecise for small

angles. Two approaches can be adopted to improve the inverse method accuracy: a) increase the number of sensors or b) decrease the number of unknown parameters. Both investigations are carried out in the next sections for small tip angle values.

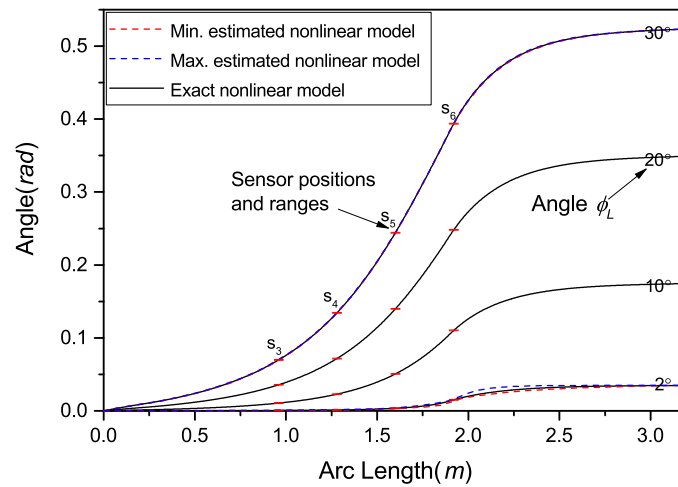


Figure 4.17: Angle distribution of nonlinear elastic model, sensors range and inverse method calculation envelope (simulated sensor data + nonlinear elastic model) with 4 sensors (A3) for two loading conditions ($\phi_L=2, 30^\circ$, $F = 125$ kN).

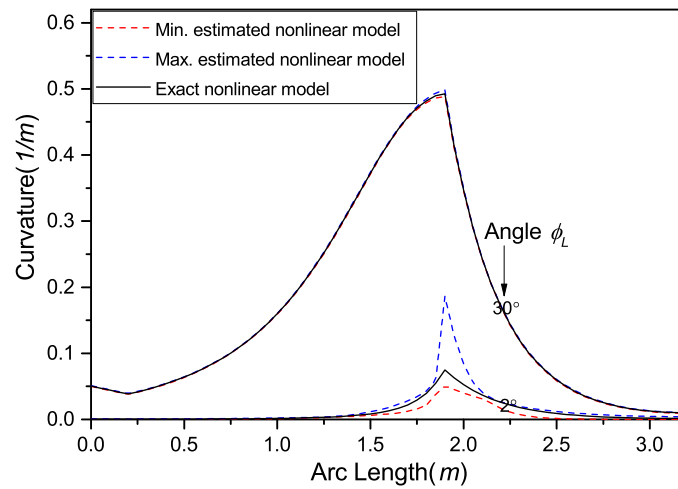


Figure 4.18: Curvature distribution of nonlinear elastic model and inverse method calculation envelope (simulated sensor data + nonlinear elastic model) with 4 sensors (A3) for two loading conditions ($\phi_L=2, 30^\circ$, $F = 125$ kN).

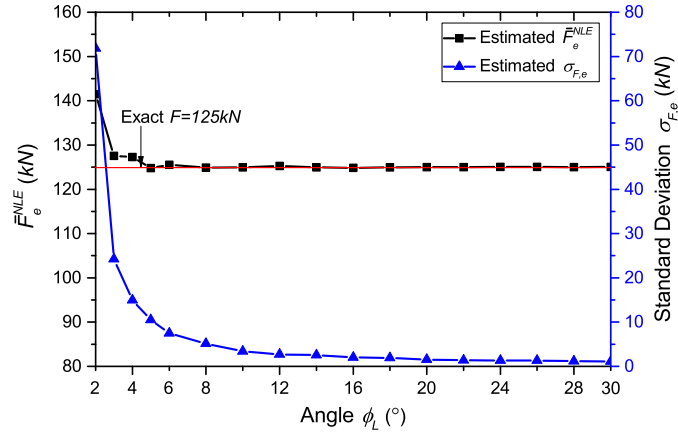


Figure 4.19: Tip angle influence on the mean and standard deviation values of the estimated top tension F_e^{NLE} ($F = 125$ kN) with 4 sensors (A3).

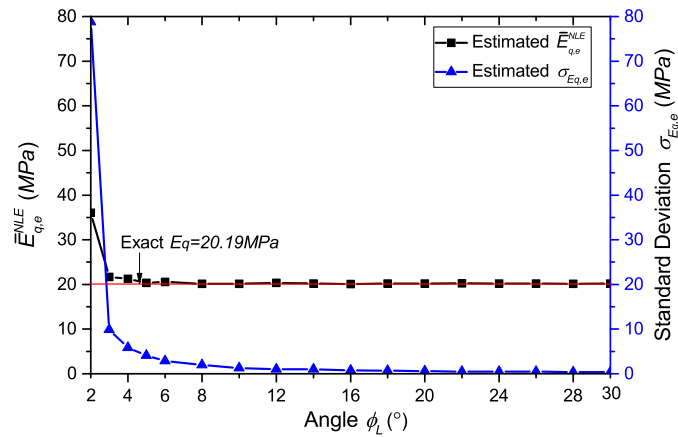


Figure 4.20: Tip angle influence on the mean and standard deviation values of the estimated material parameter $E_{q,e}^{NLE}$ ($F = 125$ kN) with 4 sensors (A3).

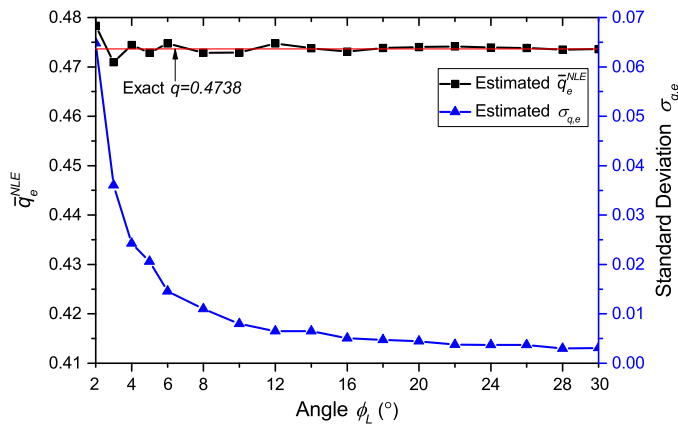


Figure 4.21: Tip angle influence on the mean and standard deviation values of the estimated material parameter q_e^{NLE} ($F = 125$ kN) with 4 sensors (A3).

Tip angle parametric assessment with 9 sensors (arrangement A5)

In this section, the number of sensors is increased from 4 to 9 sensors, employing the arrangement A5. Small tip angles ($\phi_L=2^\circ, 3^\circ, 4^\circ$ and 5°) are investigated with a fixed top tension of 125 kN. Table 4.5 presents a comparison of the top tension and material parameters mean and standard deviation for the arrangements A3 (4 sensors) and A5 (9 sensors). It can be observed that, by increasing the number of sensors from 4 to 9, the correlation between estimated and “exact” values is considerably improved with smaller standard deviations.

Table 4.5: Number of sensors influence - Comparison of top tension and material parameters mean and standard deviation for arrangements A3 and A5 ($\phi_L=2^\circ, 3^\circ, 4^\circ$ and $5^\circ, F = 125$ kN)

Angle ϕ_L Arrangement	2°		3°		4°		5°	
	A3	A5	A3	A5	A3	A5	A3	A5
\bar{F}_e^{NLE} (kN)	141.5	125.4	127.5	125.2	127.3	125.0	124.8	125.1
$\sigma_{F,e}$ (kN)	71.8	6.2	24.2	4.2	14.9	3.3	10.5	2.8
$\bar{E}_{q,e}^{NLE}$ (MPa)	36.07	20.61	21.69	20.47	21.27	20.34	20.37	20.36
$\sigma_{E_{q,e}}$ (MPa)	78.77	4.99	9.86	3.44	5.81	2.22	4.11	1.99
\bar{q}_e^{NLE}	0.4783	0.4723	0.4709	0.4737	0.4744	0.4739	0.4728	0.4742
$\sigma_{q,e}$	0.0648	0.0289	0.0361	0.0209	0.0243	0.0141	0.0206	0.0133

Tip angle parametric assessment with 4 sensors (arrangement A3) and known material properties

Instead of increasing the number of sensors to improve the inverse method accuracy, the number of unknowns can be decreased by assuming that the polyurethane material properties are known. This can be achieved by applying the inverse method to calculate the hyperelastic material parameters in a period where the largest operational loading conditions are expected. Then, for continuous monitoring at milder loading conditions, the top tension could be separately estimated with increased accuracy.

The sensor arrangement A3 with 4 sensors is now investigated with quite small tip angle values and $F = 125$ kN. Table 4.6 shows the estimated top tension mean and standard deviation values for the following angles: $\phi_L=0.5^\circ, 1^\circ, 1.5^\circ$ and 2° . Good mean correlations are observed even for the smallest tip angle adopted. The standard deviation, however, increases for decreasing tip angle values, going from 2.2 kN at $\phi_L=2^\circ$ to 15.9 kN at $\phi_L=0.5^\circ$. For the same loading condition ($\phi_L=2^\circ, F = 125$ kN), a very large difference between the standard deviation of the top tension value is

observed when comparing the results with 4 sensors for unknown ($\sigma_{F,e} = 71.8$ kN, Table 4.5) and known ($\sigma_{F,e} = 2.2$ kN, Table 4.6) polyurethane material properties, confirming the accuracy increase with known material properties.

Table 4.6: Small tip angle influence on the mean and standard deviation values of estimated top tension with known material parameters ($F = 125$ kN) and 4 sensors (A3)

Angle ϕ_L	0.5°	1°	1.5°	2°
\bar{F}_e^{NLE} (kN)	125.2	124.6	125.1	125.0
$\sigma_{F,e}$ (kN)	15.9	5.9	3.6	2.2

4.4 Conclusions

A monitoring approach has been proposed aiming at decreasing the uncertainties associated to bend stiffener mechanical response and the effective top tension employed for flexible riser lifetime (re)assessment. It is composed of gyrometers installed along riser/bend stiffener length and combined with an inverse problem methodology based on the Levenberg-Marquardt algorithm and a direct riser/bend stiffener model. A case study is carried out with numerically simulated sensor data and a top connection nonlinear elastic large deflection beam model, leading to the following main conclusions:

- i). the selection of the direct riser/bend stiffener model is an important aspect of the proposed methodology and should represent the actual response as accurately as possible;
- ii). the sensor arrangement directly affects the inverse parameter estimation and the sensitivity matrix may be employed to qualitatively support its positioning along system length;
- iii). the methodology accuracy decreases for small top connection tip angles. Two approaches can be adopted for improvement: a) increase the number of sensors or b) decrease the number of unknowns;
- iv). the number of unknowns may be decreased by calculating the material parameters in a short period, where the largest operational loading conditions are expected, followed by long term continuous effective top tension calculation at milder conditions.

Chapter 5

Parameter Estimation in Riser/Bend Stiffener System with Optical Measurements

In this chapter, an inverse problem analysis is applied in a bending-tension test system of the riser/bend stiffener combined with a direct finite element model and optical configuration measurements to simultaneously estimate the top tension and material parameters of the bend stiffener. A full-scale bending-tension test of the riser/bend stiffener system is conducted with unknown material parameters of polyurethane. During the test, the configuration of the riser/bend stiffener sample is measured by an optical image-based technique. Instead of the simplified riser/bend stiffener analytical model employed in Chapter 4, a finite element model is developed to represent the full-scale bending-tension test, which can capture the gap between riser and bend stiffener and the insert part of bend stiffener, and also simulate the loading method of bending-tension test. Section 5.1 describes the test setup of the riser/bend stiffener system and the optical technique for the configuration measurement. The finite element model for the riser/bend stiffener test is presented in section 5.2. The inverse analysis methodology based on Levenberg-Marquardt algorithm is presented in section 5.3. Finally, parameters estimation with optical measurements for the riser/bend stiffener system is investigated in section 5.4.

5.1 Bending-tension test of riser/bend stiffener with optical measurements

5.1.1 Bending-tension test of riser/bend stiffener

A full-scale bending-tension test of the riser/bend stiffener system is conducted on the vertical bending rig at the Ocean Structures Laboratory (NEO), COPPE/UFRJ. The bending rig with a length of 14 m consists of a bottom bending table, a top hydraulic cylinder tractor, and rig truss structures, as shown in Fig. 5.1. A 6" riser/bend stiffener sample is installed upside down on the vertical rig. The extended top end fitting of the riser and the top end of the bend stiffener are placed on the bending table by extended connection structures, and the tip end fitting of the riser is connected to the top tractor. The bending table fixed on the vertical rig exerts a bending moment to the riser/bend stiffener sample by changing its rotation angle, which is controlled by two side synchronous hydraulic actuators in a same plane. An approximate length related to the rotation angle is imposed on the hydraulic actuators simultaneously monitored by LVDTs. The top fixed tractor applies a tension load on the tip end fitting of the riser, which is allowed to rotate in the bending plane to compensate the system bending angle. For the given loading condition (1200 kN, -15°) with internal pressure of 10 MPa, five sets of repeated tests are conducted, with each test containing ten rotation cycles with a low frequency.

The configuration of the riser/bend stiffener bending-tension test in the vertical rig is schematically shown in Fig. 5.1b. A global coordinate system is adopted, with the coordinate origin (0, 0) at the rotation center of bending table. The geometrical parameters of the riser/bend stiffener sample on the vertical rig are illustrated in Fig. 5.1. The distance between the rotation center and rig top is 13.87 m. The length of the riser sample is 11.834 m. The extended lengths of the riser top end and the bend stiffener top end are $h_1=0.625$ m and $h_2=2.486$ m respectively, measured from the rotation center of the bending table. The total length of the hydraulic cylinder tractor is 3.82 m, with its piston kept in the middle position. A support rod with a length of 1.14 m is used to connect the riser tip end and the tractor.

5.1.2 Optical technique for configuration measurements of riser/bend stiffener

To measure the configuration of the riser/bend stiffener sample, an image-based technique is proposed in the present work. An optical monitoring system is used to track photoluminescence targets in the riser and bend stiffener areas during the

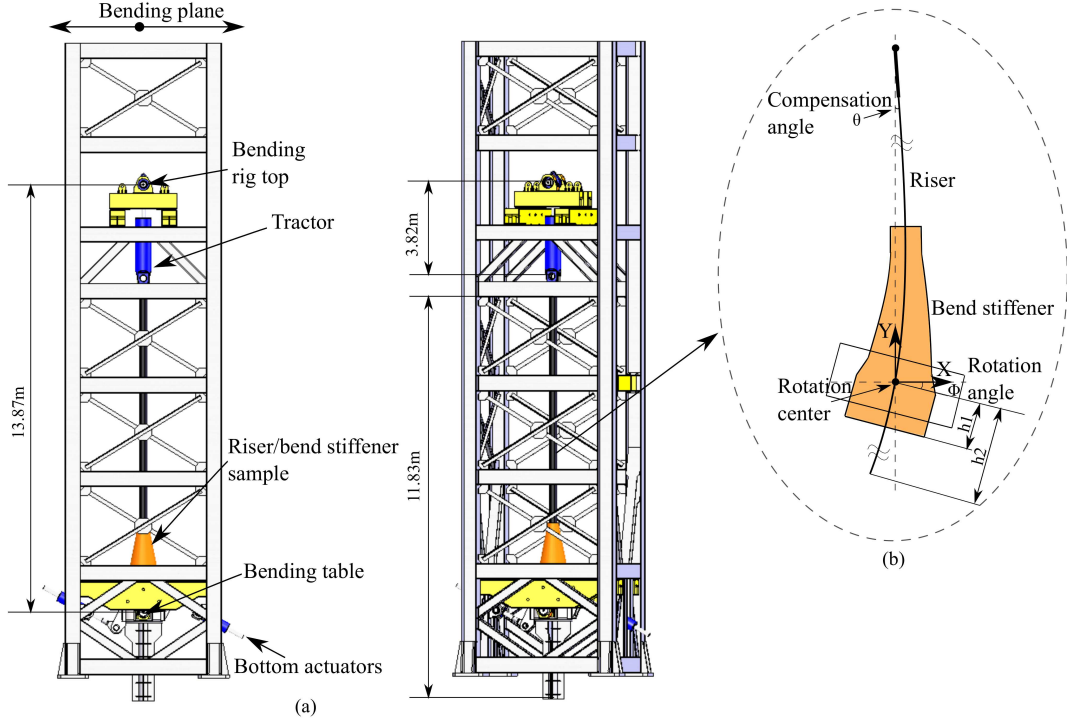


Figure 5.1: The vertical rig for the bending-tension test of riser/bend stiffener (NEO, COPPE/UFRJ).

bending-tension test. The image-based technique is divided into three stages: (i) Image digitization that defines the interested objects and the arrangement of optical monitoring system; (ii) Image processing that includes all the segmentation procedures to retrieve isolated targets from the rest of the scene; (iii) Image analysis that applies morphological operations to retrieve real-unit measurements from the segmented images. After the image analysis, the raw time series of the coordinates of each target on the riser/bend stiffener sample are obtained.

Image digitalization

a) Image acquisition

The photoluminescence colored target used in the test is a circular PANTONE 807 C color marker with 19 mm of diameter. A total number of 21 effective targets are placed along the bend stiffener central axis on the conical surface. Another 17 effective targets are placed along the riser central axis. The targets are equally distributed with a separation of $\sim 50 \pm 2$ mm along the bend stiffener and riser areas. A scheme of numbered target distribution in the bend stiffener and riser areas is presented in Fig. 5.2a. The absolute coordinates of the first targets in the bend stiffener and riser areas in relation to the bending table center are respectively (0, 0.254 m) and (0, 1.705 m).

Two 5 Mpx digital RGB cameras with CMOS sensor and global area sampling,

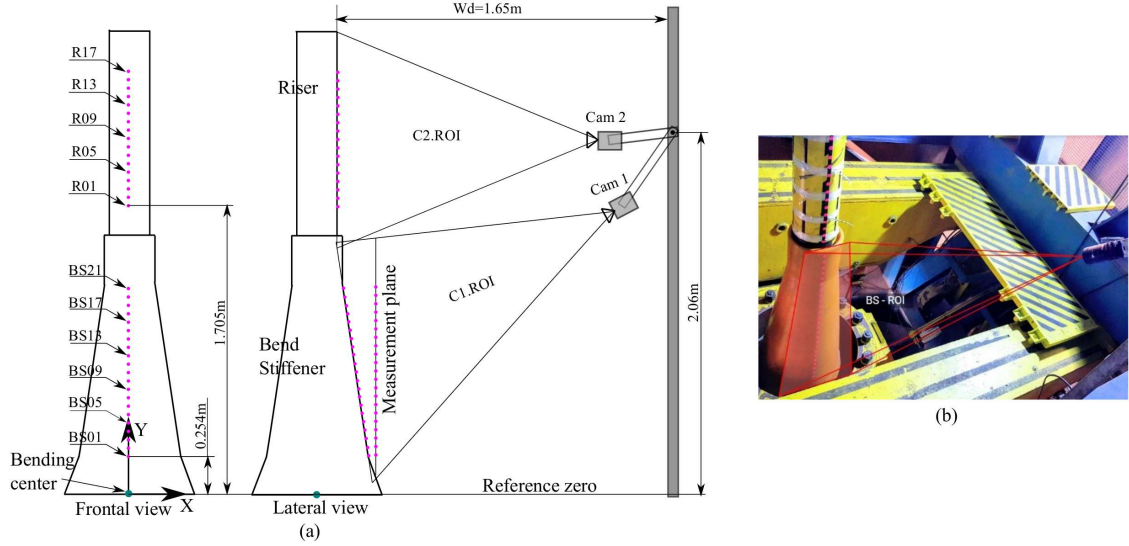


Figure 5.2: (a) Schematic of optical monitoring device arrangement and (b) region of interest of the bend stiffener camera in the scene.

Table 5.1: Optical monitoring system hardware

Items	Descriptions	Quantity
Digital Camera (DC)	5 Mpx resolution, 1/3" CMOS sensor, RGB color, global area sampling	2
Varifocal Lenses	2 mm to 50 mm focal length/C-mount.	2
PC	Core i7 processor, 16 Gb RAM, 2 Tb HDD, 128 Gb SSD, GigE x4 ports for communication	1
Communication wires	Cat5e gigabit	100
Connectors	RJ45/USB3/Borne	30
DC power supply	12 Volts/500 mA	2
Cameras fixation support	Magnetic tripod or gimbal mounting	3
Targets	Photoluminescent targets with UV color range of 300 nm to 400 nm	200

and two COMPUTAR varifocal lenses are used to capture the images of the targets in the bend stiffener and riser areas during the test. The hardware components of the optical monitoring system are listed in Table 5.1. Both cameras are fixed on a vertical structure, as shown in Fig. 5.2a. The vertical rod is placed in front of the central axis of the riser/bend stiffener sample with a working distance of $W_d=1.65$ m. The cameras are arranged with capturing angles in the top-front of sample targets with a perspective distortion due to the interference structures in front of the sample in the scene. Cam1 and Cam2 represent the cameras for the bend stiffener and riser regions of interest respectively. Figure 5.2b shows the full two-dimensional region of interest (ROI) of the bend stiffener camera in the scene. The test illumination in the scene is provided by two 100W LED reflectors light with color temperature of 6000K (blue light) to supply enough luminosities to identify the photoluminescence targets.

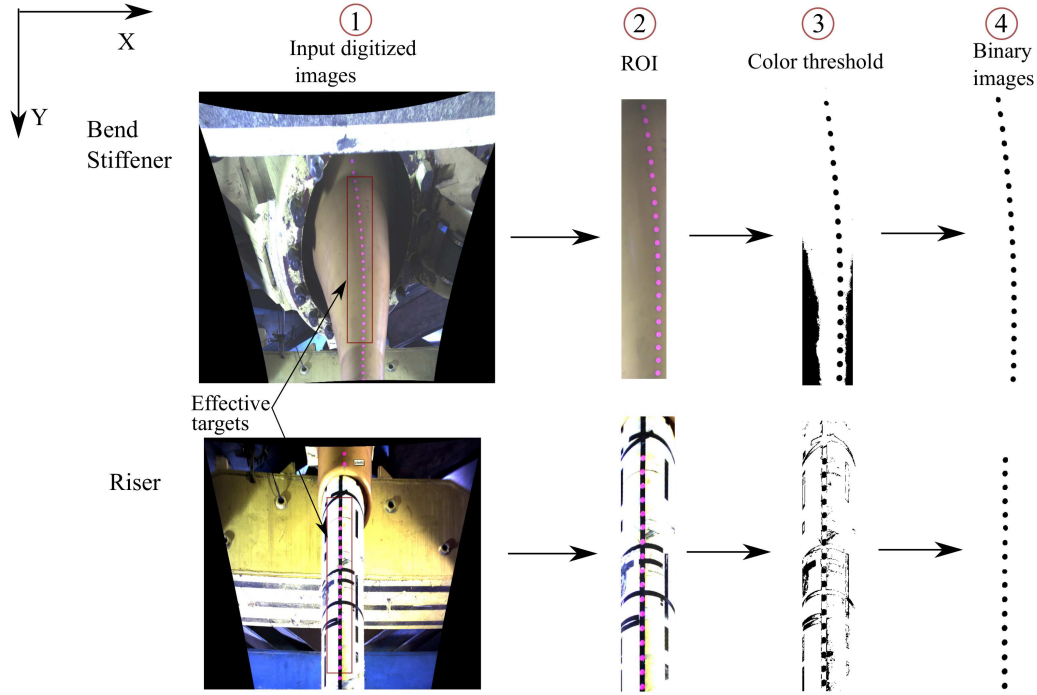


Figure 5.3: Image processing for bend stiffener and riser targets.

b) Lens correction and Image calibration

Firstly, lens correction and calibration of the acquired images are performed by using a series of images of a circle pattern table that are captured to cover the entire area of interest. Secondly, the camera/lens coefficients are determined. Finally, the digitized images are rectified and then undistorted by using a perspective correction. These steps are performed by using the IMAQ libraries provided by the Vision Assistant software (National Instruments, 2014) [70].

Image processing

The undistorted stacks of riser and bend stiffener images are processed by using the open-source software ImageJ [66] separately for five tests. Figure 5.3 presents the image processing of the bend stiffener and riser targets. The image processing procedure is as follows: (i) import the stacks of bend stiffener images of each ten cycle test in ImageJ, for example 120 images in Test 1; (ii) set the image global scale of 1.515 pix/mm related to the reference value of the diameter of target $D_t = 19$ mm; (iii) select a region of interest containing all the targets in the image stacks, and then chop the images by the selected region; (iv) employ color threshold to filter the targets in the image; (v) apply Otsu's method [71] to transform the filtered channel images into binary stack images with low level noise. The same processing approach is used to the riser original images with a image global scale 2.15 pix/mm.

Image analysis

The processed stacks of binary images are analyzed through morphological operations of the free-orientation metrics class (e.g., area and centroid position) at specified regions of interest. The considered method, named area fraction, describes the density of pixels, with an intensity value of 1 or 0 (black or white respectively) within a region of interest. In general, the time variation of the area fraction of the target particles (density of black color pixels) inside ROIs is used to determine time series of targets coordinates.

5.1.3 Data analysis of optical measurements

The relative coordinates of the targets on the riser/bend stiffener sample are recorded in the bending plane by the optical monitoring system. A cubic interpolation is applied on the coordinates of the targets during ten cycle test after the image analysis. Simultaneously, a calibrated rotary position sensor (RVIT15-60) with response frequency of 0.5 Hz is placed on the rotation axis of the bending table to monitor the rotation angle during the test. As the bending table rotation is controlled by two side synchronous hydraulic actuators, there is a small difference between the operational and given loading conditions. For example, the rotation angles are within a range of $(0.83^\circ, -15.33^\circ)$ during the Test 1. The time series of rotation angle and coordinates (X, Y) are synchronized based on the simultaneous maximum rotation angle and largest displacement.

All target coordinates are calculated in the global coordinate system by the relative coordinates plus the first target values in the bend stiffener and riser regions respectively. The coordinates of the targets at the zero rotation position are calculated by the coordinate interpolation functions. To reduce the system error by the target deviation, the configurations $X_{central}$ of riser/bend stiffener central axis in the maximum rotation is considered to be the relative coordinates of target configurations in maximum rotation related to the zero rotation configurations $X_{central}^i = X_{max}^i - X_0^i$, where X_{max}^i and X_0^i are interpolated coordinates of targets in maximum and zero rotations respectively. The optical measurements of 21 targets on the bend stiffener central axis and 17 targets on the riser central axis and the mean values of measurements in each position $(X_{mean,i}, Y_{mean,i})$ for five tests are presented in Fig. 5.4. The rotation angle, tension and internal pressure of the riser at the maximum rotation for the five tests are given in Table 5.2.

The error of the optical measurements is identified during the image digitalization and processing stages. The image digitalization error could be caused by the optical monitoring system setup and lens distortion of the acquisition device. For the image processing, the error is generated by losing pixels during the image digitalization.

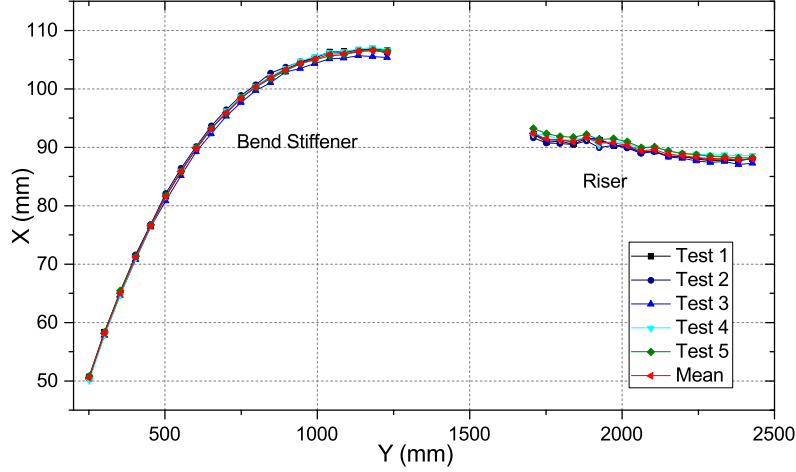


Figure 5.4: 21 and 17 target measurements on the bend stiffener and riser central axes respectively and mean values of measurements in each position for five tests.

Table 5.2: Rotation angle, tension and internal pressure of riser at the maximum rotation for five tests

	Max. Rotation ($^{\circ}$)	Tension (kN)	Internal pressure (MPa)
Test-1	15.33	1286	9.66
Test-2	15.37	1290	9.56
Test-3	15.34	1284	9.66
Test-4	15.33	1287	9.58
Test-5	15.34	1283	9.73

5.2 Finite element model of riser/bend stiffener test

A finite element model (FEM) is employed to represent the bending-tension test of the riser/bend stiffener system. To ensure the analysis accuracy with a reduced computational time, the FEM model is constructed with following simplifications:

- The flexible riser is represented by a beam bending model with large deflection, as the armour wire stresses are not considered in the present work;
- The bending table is represented by a reference point at its rotation center;
- The riser and bend stiffener top ends are rigidly connected to the reference point directly;
- A metallic protection cylinder is placed outside of the bend stiffener top end and tied with the polyurethane, instead of the connection of the flange and bolt inserts with polyurethane;
- The gravity effect of riser is represented by an effective density.

5.2.1 Finite element model

The FEM model for the riser/bend stiffener test is implemented by using the software Abaqus [72], as shown in Fig. 5.5. The riser is represented by beam elements (B31) in space, tied with contact surface elements (SFM3D4R) without stiffness. A general beam section is adopted to define the linear bending, axial and torsional behavior of the riser. Two end fittings of the riser are assumed to be metallic rods with an equivalent diameter of 0.2 m. The bend stiffener is represented by solid elements (C3D8R), including the polyurethane and top metallic connection parts. The metallic part of bend stiffener is tied with the polyurethane part. The bend stiffener and riser top ends are both rigidly connected to the reference point at the rotation center of the bending table by employing multi-point constraint (MPC) beams. The metallic support rod with a diameter of 0.1 m is represented by beam elements (B31), tied to the tip end of riser and the hydraulic tractor. A translator is applied to represent the axial hydraulic tractor. The translator provides a slot constraint between two nodes and aligns their local directions. The interaction between the riser and the bend stiffener is implemented by surface-to-surface contacts with “*Hard*” contact and zero friction coefficient. The reference point of the bending table and the translator top are both fixed in space except the rotation degree of freedom in the bending plane.

The material of metallic rods for the riser end fitting and support structure is defined by Young’s modulus 210 GPa and Poisson’s ratio 0.3. A reference point rotation angle and a translator tension force are applied for the bending-tension test. As the bending-tension test is conducted on the vertical rig, the gravity of the riser/bend stiffener system is considered by its component densities, as shown in Table 5.3. The gravity constant is 9.8 m/s².

Table 5.3: Component densities ρ of riser/bend stiffener system

	Metal part	Polyurethane	Riser
ρ (kg/m ³)	7850	1150.4	4612

5.2.2 Hyperelastic behavior of polyurethane

There are a number of hyperelastic material models in the literature, proposed to model isotropic elastomers, such as: Arruda-Boyce, Marlow, Mooney-Rivlin, neo-Hookean, Ogden, Polynomial, Yeoh, among others, which were derived from strain energy potentials. In the present work, Marlow and first order Polynomial forms of strain energy potentials are considered to represent the hyperelastic response of

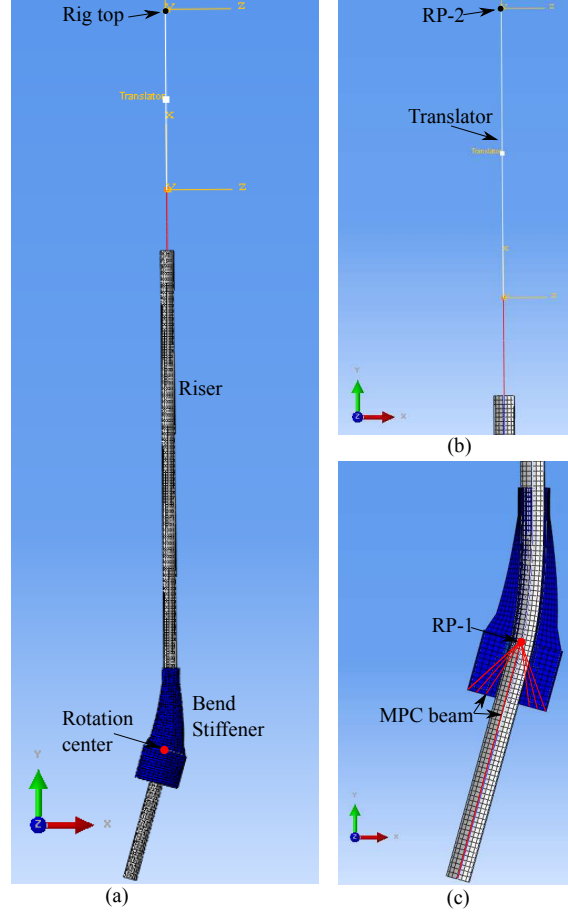


Figure 5.5: Simplified finite element model for the bending-tension test of the riser/bend stiffener system (Mesh 0.05 m).

the bend stiffener polyurethane. In Abaqus, the material coefficients C10 and C01 can be used to define first order Polynomial form of hyperelastic model with a small compressibility coefficient D1. Meanwhile, the Marlow form of the strain energy potential must be defined with test data. A power function is employed to represent the hyperelastic response of polyurethane,

$$\sigma(\epsilon) = \text{sign}(\epsilon)E_q|\epsilon|^q, \quad (5.1)$$

where σ and ϵ are nominal stress and strain respectively, E_q and q are material coefficients, and $\text{sign}(\epsilon)$ is the sign function. Equation (5.1) with two material parameters E_q and q is used to generate the stress-strain data for the direct FEM model with Marlow hyperelastic model as an input. The Poisson's ratio is 0.45 in the hyperelastic model. Table 5.4 summarize the material coefficients of two hyperelastic models for bend stiffener polyurethane in this work.

Table 5.4: Material coefficients of the hyperelastic models of polyurethane

Models	Material coefficients
Marlow	(E_q, q) represents the test data
Polynomial ($N=1$)	C10, C01

5.2.3 Mesh sensitivity analysis

Mesh convergence of riser/bend stiffener FEM model is analyzed for two load conditions (1200 kN, 15°) and (1500 kN, 15°) with mesh sizes 0.02 m and 0.05 m for both beam and solid elements. An industry used material of polyurethane is considered for the bend stiffener for the mesh analyses, as shown in Fig. 3.3. Table 5.5 shows the total element numbers of the FEM models and computational time. The corresponding configurations of the FEM models for two load conditions are presented in Fig. 5.6, with no significant difference observed. The FEM model with mesh size 0.05 m is chosen in the following analysis, considering its less computational time.

Table 5.5: Mesh sensitivity analysis for the FEM model of the riser/bend stiffener system

Mesh sizes	Number of elements	Computational time(s)	
		(1200 kN, 15°)	(1500 kN, 15°)
0.02 m	105197	2804.5	2872.7
0.05 m	15520	351.3	363

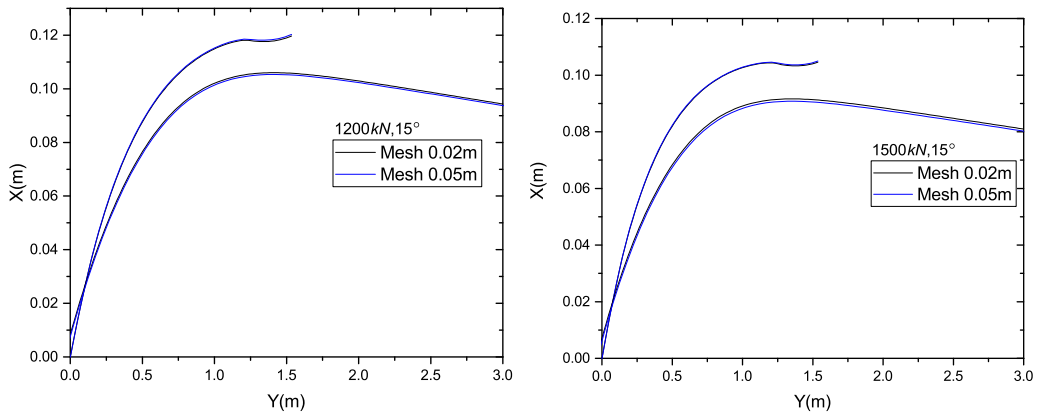


Figure 5.6: Configurations of the FEM models of the riser/bend stiffener with two mesh sizes for loading conditions (a) (1200 kN, 15°) and (b) (1500 kN, 15°).

5.3 Inverse problem methodology

During the riser/bend stiffener bending-tension test, material parameters of the bend stiffener are unknown, which are greatly affected by the operational conditions. In the present work, an inverse problem methodology is employed to numerically estimate the hyperelastic response of polyurethane and the effective top tension, based on the direct FEM model of the riser/bend stiffener and the configuration measurements $(X_{m1}, X_{m2}, \dots, X_{mN})$, with N being the number of targets.

5.3.1 Levenberg-Marquardt algorithm

The Levenberg-Marquardt (L-M) algorithm based on a damped least-square minimization approach is applied in the inverse analysis, as described in Eq. (4.9) in Chapter 4. P_1, P_2, \dots, P_M represent the unknown material parameters and top tension in the riser/bend stiffener system, and M is the number of unknown parameters. The summation of the squared residuals of the numerically estimated configuration $X_i(P_1, P_2, \dots, P_M)$ and measurements X_{mi} , $i = 1, 2, \dots, N$, at N positions yields,

$$R(P_1, P_2, \dots, P_M) = \sum_{i=1}^N (X_{mi} - X_i(P_1, P_2, \dots, P_M))^2. \quad (5.2)$$

The equation can be expressed in vectorial form,

$$R(\mathbf{P}) = [\mathbf{X}_m - \mathbf{X}(\mathbf{P})]^T [\mathbf{X}_m - \mathbf{X}(\mathbf{P})], \quad (5.3)$$

where $\mathbf{P}^T = [P_1, P_2, \dots, P_M]$ is the vector of unknown parameters, and \mathbf{X}_m , $\mathbf{X}(\mathbf{P})$ are the vectors of measurements and estimated configurations respectively. By the least-square approach, the overall solution (P_1, P_2, \dots, P_M) minimizes the summation of the squared residuals $R(P_1, P_2, \dots, P_M)$ which best matches the estimated configuration and measurements. The L-M algorithm is given by,

$$\mathbf{P}^{k+1} = \mathbf{P}^k + [(\mathbf{J}^k)^T \mathbf{J}^k + \mu^k \mathbf{\Omega}^k]^{-1} (\mathbf{J}^k)^T [\mathbf{X}_m - \mathbf{X}(\mathbf{P}^k)], \quad (5.4)$$

where \mathbf{J} is the Jacobian matrix, $\mathbf{\Omega}^k = \text{diag}[(\mathbf{J}^k)^T \mathbf{J}^k]$ is a diagonal matrix, μ is the damping factor, and k is the iterative index number.

The L-M algorithm for riser/bend stiffener system is implemented by the Python programming [73] with the Abaqus scripting interface [72]. A direct model function $X_{FEM}(P_1, P_2, \dots, P_M)$ is defined to update the variables (P_1, P_2, \dots, P_M) in the FEM model of the riser/bend stiffener, and then execute calculation of FEM model in Abaqus package and output the corresponding calculated configuration. A cubic interpolation is applied on the coordinates of the central axis nodes of the bend

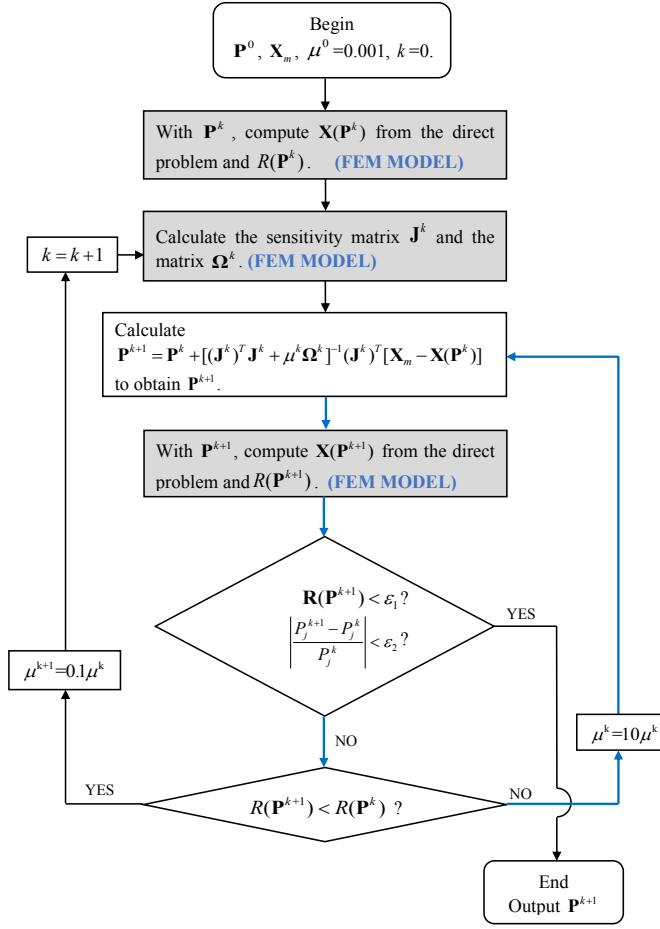


Figure 5.7: Flowchart of L-M algorithm for the parameter estimation in the riser/bend stiffener system with optical measurements.

stiffener in the FEM model, and the estimated configurations (X_1, X_2, \dots, X_N) are calculated in the measured vertical positions $(Y_{m1}, Y_{m2}, \dots, Y_{mN})$ of all the targets based on the interpolation function. The elements in the Jacobian matrix are defined by $J_{ij} = \partial X_i / \partial P_j$, $i = 1, 2, \dots, N$ and $j = 1, 2, \dots, M$, which are related to the numbers of measurements and unknown parameters. The sensitivity coefficients in the Jacobian matrix can then be numerically calculated by finite difference method,

$$J_{ij}^k \cong \frac{X_{FEM,i}(P_1, P_2, \dots, P_j + \beta P_j, \dots, P_M) - X_{FEM,i}(P_1, P_2, \dots, P_j, \dots, P_M)}{\beta P_j}, \quad (5.5)$$

$$i = 1, 2, \dots, N \quad \text{and} \quad j = 1, 2, \dots, M$$

where the step difference coefficient is given by $\beta = 10^{-4}$.

The flowchart of L-M algorithm for parameter estimation in the bending-tension test of the riser/bend stiffener system is presented in Fig. 5.7. The initial unknown parameters \mathbf{P}^0 can be any set of reasonable values, and the initial damping factor

is set to be $\mu^0 = 0.001$. The following stopping criteria are employed to terminate the iteration in the L-M algorithm,

$$R(\mathbf{P}^{k+1}) < \epsilon_1, \quad (5.6a)$$

$$\left| \frac{P_j^{k+1} - P_j^k}{P_j^k} \right| < \epsilon_2 \quad \text{and} \quad j = 1, 2, \dots, M \quad (5.6b)$$

where ϵ_1 and ϵ_2 are tolerances of residuals and estimated parameters respectively. Here, the termination tolerances are set to be $\epsilon_1 = 10^{-6}$ and $\epsilon_2 = 10^{-8}$. The maximum number of iterations is chosen to be 50 in the loop, which is found to be sufficient for the present problem. At each iterative step k , the direct FEM model of the riser/bend stiffener is calculated at least $2+M$ times, $\mathbf{X}(\mathbf{P}^k)$, $X(P_1^k, P_2^k, \dots, P_j^k + \beta P_j^k, \dots, P_M^k)$, $\mathbf{X}(\mathbf{P}^{k+1})$. During the subpath for each iteration, \mathbf{P}^k , $\mathbf{X}(\mathbf{P}^k)$, $R(\mathbf{P}^k)$ are kept with same values, while only $\mathbf{X}(\mathbf{P}^{k+1})$ is recalculated by the direct model, related to the variations of damping factor μ^k .

5.3.2 Inverse analysis for the riser/bend stiffener system

To verify the feasibility of inverse analysis methodology for bending-tension test of the riser/bend stiffener system, a preliminary assessment is carried out with numerically simulated measurements based on the direct FEM models. The configuration measurements of 8 targets, BS11, BS12, \dots , BS18, of the riser/bend stiffener system are used in the inverse analysis to simultaneously estimate the top tension ($P_1 = F$) and material parameters in nonlinear elastic equation (5.1) ($P_2 = E_q$, $P_3 = q$). Simulated measurement errors are generated by a random number generator with Gaussian distribution multiplying a noise level of the configuration measurements of exact parameters. The measured configuration in each point is simulated by adding the random error to the exact configuration value as follows,

$$X_i^M = X_i^{Exact} + X_i^{Exact} a_i^{Random} \frac{Q}{100}, \quad (5.7)$$

and $i = 11, 12, \dots, 18$

where X_i^{Exact} is the exact configuration at i th point, $Q\%$ is the noise level related to the exact configurations, and a_i^{Random} are random numbers with Gaussian distribution between -1 and 1. The configuration measurements of 8 targets are generated by the FEM model with exact parameters ($F=1200$ kN, $E_q=15$ MPa, $q=0.7$) adding 8 noise levels of 0%, 0.2%, 0.5%, 1%, 1.5%, 2%, 2.5% and 3% respectively, as shown in Fig. 5.8.

As the simulated measurements are applied in the preliminary inverse analysis, a larger termination tolerance of residuals $\epsilon_1 = 10^{-5}$ is chosen to analyze the mea-

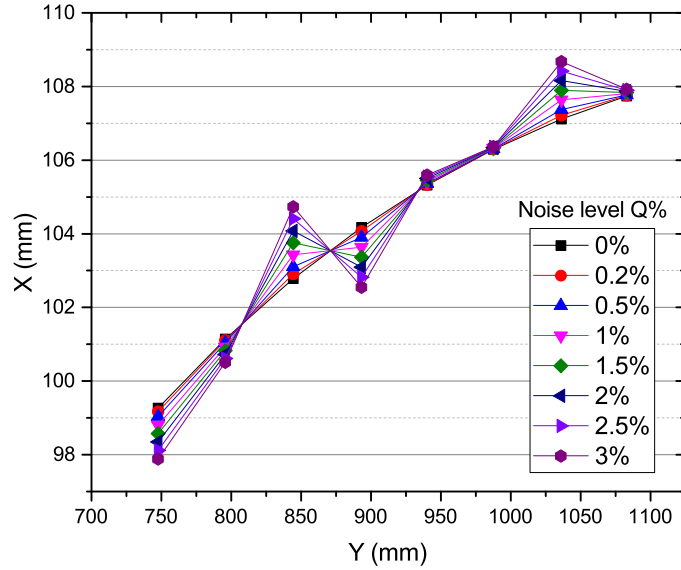


Figure 5.8: The simulated measurements of 8 targets in the bend stiffener region with 8 noise levels.

Table 5.6: The estimated parameters ($F_e, E_{q,e}, q_e$) of the riser/bend stiffener system for the simulated measurements with 8 noise levels for exact parameters (1200 kN, 15 MPa, 0.7)

Noise levels	Estimated force		Estimated material		Residuals		Iterations	
	F_e - LM (kN)	Error	$E_{q,e}$ - LM (MPa)	Error	q_e - LM	Error		
0	1200	0.002%	15.00	0.0046%	0.700	0.0007%	4.5×10^{-15}	16
0.2%	1123	6.4%	14.48	3.4%	0.714	2.0%	0.042	3
0.5%	1038	13.4%	14.11	5.9%	0.737	5.3%	0.261	47
1.0%	1044	12.9%	14.16	5.5%	0.736	5.1%	1.10	9
1.5%	928	22.6%	13.44	10.3%	0.766	9.4%	2.43	26
2.0%	1032	14.0%	14.34	4.3%	0.744	6.4%	4.62	15
2.5%	889	25.9%	13.98	6.7%	0.797	13.9%	6.97	19
3.0%	791	34.0%	12.81	14.5%	0.817	16.7%	9.86	24

surement error effect. Table 5.6 shows the estimated parameters ($F_e, E_{q,e}, q_e$), final summations of squared residuals and numbers of iteration for the eight measurement noise level cases. It can be seen that the estimated parameters ($F_e, E_{q,e}, q_e$) show an excellent agreement with the exact (F, E_q, q) with the final residual close to zero when the simulated measurements are without error. The estimated parameters deviate significantly from the exact values if 1% or larger random experimental errors are present. Larger final summations of squared residuals are obtained with higher measurement noise levels.

5.4 Parameter estimation with optical measurements

Parameter estimation with optical configuration measurements is employed in the bending-tension test of the riser/bend stiffener system, based on the L-M algorithm combined with the direct riser/bend stiffener FEM model. Fig. 5.4 presents the measured configurations of 21 targets and 17 targets along the bend stiffener and riser central axes respectively, and mean values of measurements in each position for five tests. The measurements of 8 targets close to the bend stiffener tip end, BS11, BS12, . . . , BS18, shown in Fig. 5.9, are used to estimate the top tension and polyurethane hyperelastic response in the inverse analysis. The remaining measurements in bend stiffener and riser regions can be employed to validate the estimated configurations of the bend stiffener and riser. In the following inverse analyses of the riser/bend stiffener system, the hyperelastic response of polyurethane is estimated firstly in Section 5.4.1; simultaneous estimation of material parameters and top tension is then presented in Section 5.4.2; and finally, a proposed multiple parameter estimation of material parameters and constrained top tension is investigated in Section 5.4.3.

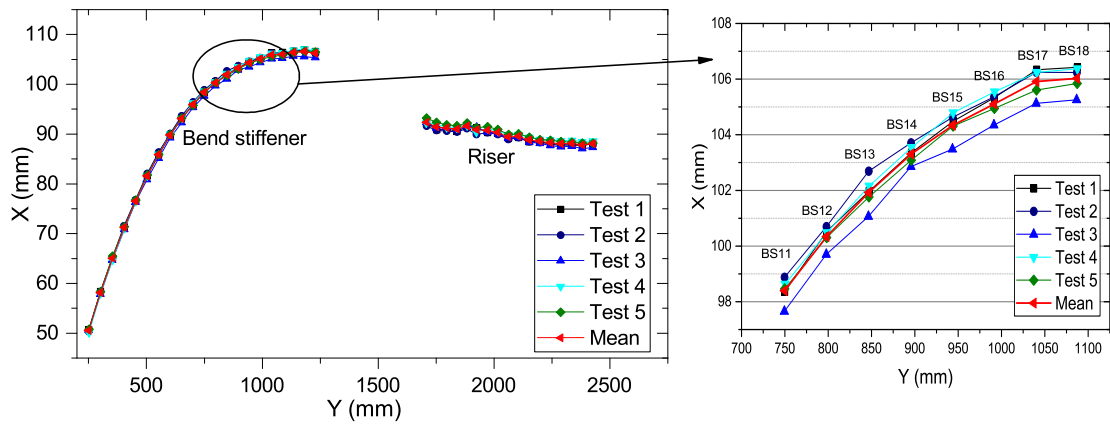


Figure 5.9: Configuration measurements of 8 targets on the bend stiffener central axis and mean values of measurements in each position for five tests.

5.4.1 Estimation of material parameters

During the bending-tension test of the riser/bend stiffener system, the hyperelastic response of bend stiffener polyurethane is unknown, which are greatly affected by the ambient temperature and humidity. The average temperature and humidity are around 29.5°C and 70% respectively for the five repetition tests. Material parameters of the bend stiffener are estimated firstly by the inverse analysis in this work. The

measurements of 8 targets, shown in Fig. 5.9, are used to numerically estimate the material coefficients (E_q, q) in nonlinear elastic equation (5.1). The estimated parameters $(E_{q,e}, q_e)$, the final summations of squared residuals and numbers of iteration are presented in Table 5.7 respectively for five tests and mean data. The nominal strain-stress relations given by estimated material parameters $(E_{q,e}, q_e)$ are shown in Fig. 5.10. A maximum strain of 6% is observed in the FEM models with estimated material parameters. Meanwhile, the estimation of first order Polynomial hyperelastic model ($N=1$) is implemented with the mean measurements of 8 targets. The estimated coefficients are $C10=27575439$ and $C01=-20036524$, and the strain-stress relation is presented in Fig. 5.10 in comparison with the nonlinear elastic model $(E_{q,e}, q_e)$.

Table 5.7: The estimated material parameters $(E_{q,e}, q_e)$ of bend stiffener polyurethane

	Estimated material		Residuals	
	$E_{q,e}$ - LM (MPa)	q_e - LM	$R(F, E_q, q)$ (mm ²)	Iterations
Test 1	14.54	0.653	0.672	4
Test 2	16.19	0.688	0.325	18
Test 3	14.02	0.648	0.561	5
Test 4	13.85	0.635	0.493	6
Test 5	14.93	0.665	0.148	3
Mean	15.49	0.676	0.295	8

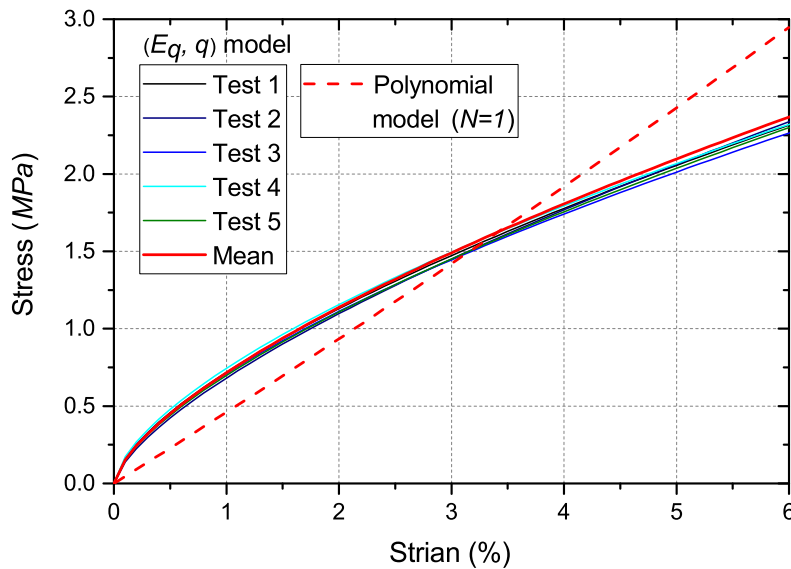


Figure 5.10: Nominal strain-stress relations by estimated material parameters for two hyperelastic models of polyurethane.

Using the measured configurations of 8 targets for five tests and mean data, the bend stiffener material behavior is estimated by two hyperelastic models of

polyurethane. For the nonlinear elastic model $(E_{q,e}, q_e)$, the estimated strain-stress curves are concentrated with small variations between repeated estimations. The estimated Polynomial model ($N=1$) is close to the estimated nonlinear elastic model $(E_{q,e}, q_e)$ in general, while the estimated strain-stress curve presents highly linear elastic behavior. A soft material is obtained for the bend stiffener polyurethane in the present work comparing to the nominal strain-stress relation with the laboratory temperature 24°C in Fig. 3.3 [18], which could be caused by the high ambient temperature and humidity during the bending-tension test. For all the subsequent analyses, the nonlinear elastic model (E_q, q) is employed in the inverse parameter estimation.

5.4.2 Estimation of material parameters and top tension

In this section, the configuration measurements of 8 targets, BS11, BS12, . . . , BS18, as presented in Fig. 5.9, are applied in the inverse analysis of the riser/bend stiffener system to simultaneously estimate the top tension and material parameters of polyurethane (F, E_q, q) . The measured tension forces are used to verify the multiple parameter estimation for the riser/bend stiffener system. Table 5.8 presents the estimated parameters $(F_e, E_{q,e}, q_e)$, the final summations of squared residuals and numbers of iteration for five tests and the mean data. It can be seen that the estimated forces are close to the measured forces with 4% and 2.8% errors respectively for Test 1 and Test 4. The estimated forces are larger than the measured forces with larger values of estimated material parameter $E_{q,e}$ for Test 2, Test 3, Test 5 and the mean data. The proposed inverse problem methodology is reliable for estimation of the top tension and bend stiffener material parameters when the measurements error is small, for example Test 1 and Test 4. With large measurement error, simultaneous estimation of material parameters and loading condition may lead to a large deviation.

Table 5.8: Estimated parameters $(F_e, E_{q,e}, q_e)$ of riser/bend stiffener system

	Measurements		Estimated tension		Estimated material		Residuals	
	Rotation (°)	F (kN)	F_e - LM (kN)	Error	$E_{q,e}$ - LM (MPa)	q_e - LM	$R(F, E_q, q)$ (mm ²)	Iterations
Test 1	15.33	1286	1234	4.0%	15.04	0.697	0.192	12
Test 2	15.37	1290	1491	15.6%	16.95	0.664	0.520	6
Test 3	15.34	1284	1432	11.5%	17.56	0.699	0.296	12
Test 4	15.33	1287	1323	2.8%	15.60	0.683	0.267	7
Test 5	15.34	1283	1427	11.2%	16.05	0.666	0.263	8
Mean	15.34	1286	1530	18.9%	18.32	0.693	0.163	8

5.4.3 Estimation of material parameters and constrained top tension

When the range of the top tension is known in a field application, the constraint conditions of the unknown top tension can be incorporated in the inverse analysis. The multiple parameter estimation of material parameters and constrained top tension is proposed to reduce the effects of the measurement errors in the inverse analysis of riser/bend stiffener system. The configuration measurements of 8 targets, BS11, BS12, . . . , BS18, as presented in Fig. 5.9, are used in the inverse analysis of riser/bend stiffener system for five tests and mean data, and the remaining measurements in bend stiffener and riser regions are applied to verify the estimated configurations of bend stiffener and riser. In the L-M algorithm of inverse analysis, the termination tolerances are modified to be (i) $\epsilon_1 = 10^{-6}$, and (ii) $\epsilon_2 = 10^{-8}$ or $F_e > 1300$ kN or $F_e < 1000$ kN. L-M algorithm guarantees the summation of squared residuals keep decreasing, $R(\mathbf{P}^{k+1}) < R(\mathbf{P}^k)$, in the negative gradient direction during the whole iterative process. When the tolerance $\epsilon_1 = 10^{-6}$ m² is obtained, the summation of the squared residuals is considered small enough close to the minimum solution. The following iterative parameter estimations will advance to the minimization of the summation of the squared residuals. If the estimated force is outside of constraint range $1000 \text{ kN} \leq F_e \leq 1300 \text{ kN}$, the iterations will be terminated, and the last estimated parameters are considered to be estimation solution with smallest summation of the squared residuals. Otherwise, the iterations will advance to the stopping tolerance $\epsilon_2 = 10^{-8}$ with the minimum summation of the squared residuals.

Table 5.9: Estimated material parameters and constrained tension ($F_e, E_{q,e}, q_e$) of riser/bend stiffener system

	Measurements		Estimated tension		Estimated material		Residuals	
	Rotation (°)	F (kN)	F_e - LM (kN)	Error	$E_{q,e}$ - LM (MPa)	q_e - LM	$R(F, E_{q,e}, q_e)$ (mm ²)	Iterations
Test 1	15.33	1286	1234	4.0%	15.04	0.697	0.192	12
Test 2	15.37	1290	1225	5.0%	14.16	0.679	0.870	3
Test 3	15.34	1284	1296	0.9%	15.22	0.690	0.393	8
Test 4	15.33	1287	1242	3.5%	14.80	0.687	0.379	3
Test 5	15.34	1283	1185	7.6%	13.68	0.684	0.479	3
Mean	15.34	1286	1296	0.8%	15.06	0.679	0.360	6

The estimated parameters ($F_e, E_{q,e}, q_e$), the final summations of squared residuals and numbers of iteration for five tests are presented in Table 5.9. The final summations of squared residuals of five tests and mean data for merely material estimation, tension and material estimation, and constrained tension and material

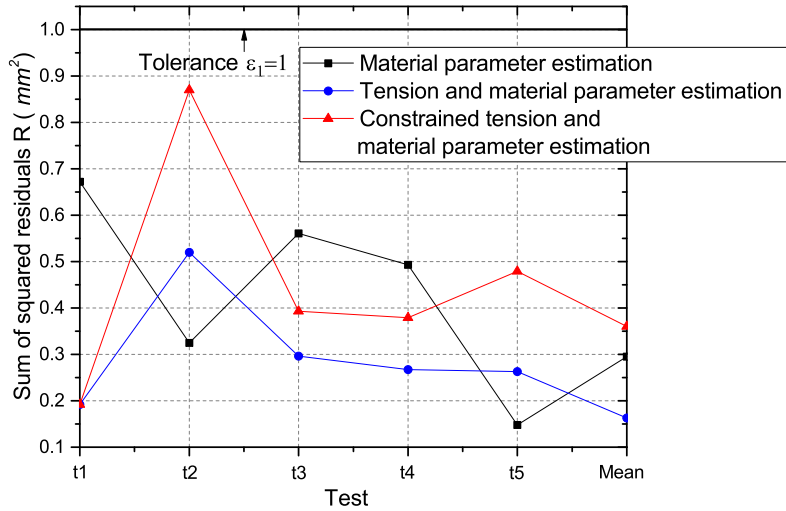


Figure 5.11: Final summation of squared residuals of five tests and mean data for three types of parameter estimations.

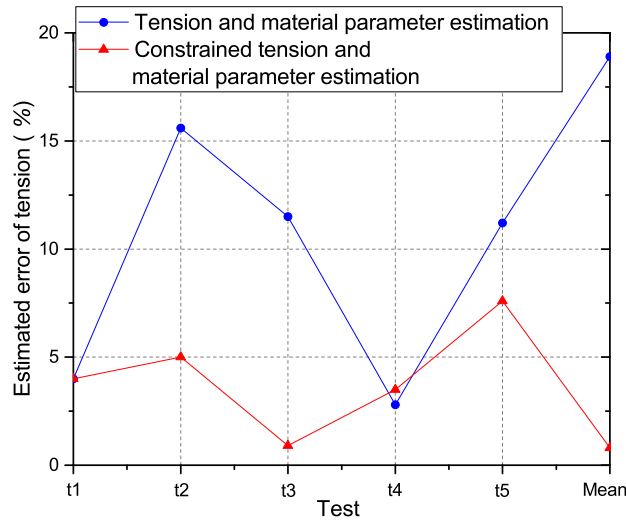


Figure 5.12: Estimated error of tension of five tests and mean data for two types of parameter estimations.

estimation are shown in Fig. 5.11. The estimated errors of tensions of five tests and mean data for the tension and material estimation and the constrained tension and material estimation are given in Fig. 5.12. After a number of iterations, the estimations are in the radius of convergence constrained by $1000 \text{ kN} \leq F_e \leq 1300 \text{ kN}$, and the summations of squared residuals are reduced below than $\epsilon_1 = 10^{-6}$. It can be seen that the constraint on the range of the top tension improves significantly the precision of the estimation of the top tension force over the unconstrained simultaneous estimation of the three parameters. The nominal strain-stress relations given by estimated material parameters ($E_{q,e}, q_e$) of bend stiffener for five tests and mean data are shown in Fig. 5.13. The estimated material strain-stress curves from constrained force and material estimation are closed to the estimated material in

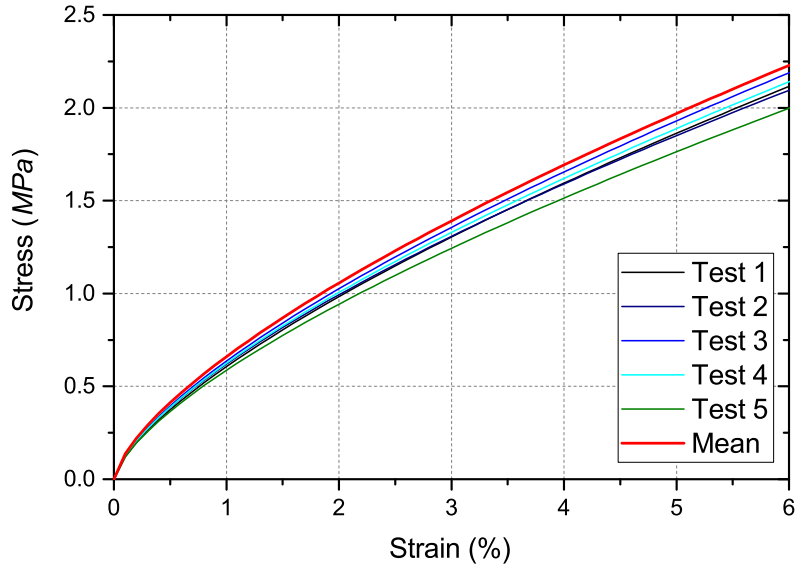


Figure 5.13: Nominal strain-stress relation by estimated material parameters of bend stiffener in the material and constrained tension estimation case.

Section 5.4.1, while two material parameter estimation are more concentrated than three parameter estimation of constrained tension and material for the repeated estimations of five tests and mean data.

The configurations for bend stiffener and riser at the maximum rotation are calculated by the FEM model, once the estimated tension and material parameters ($F_e, E_{q,e}, q_e$) are obtained. The estimated configurations of bend stiffener in FEM model for five tests and mean data are shown in Fig. 5.14. The configurations of the measurements and the results by the FEM model with estimated parameters agree well. There are small deviations between configurations of measurements and FEM models in the initial target positions of bend stiffener for all five tests and mean data, which may be caused by the system error of optical system.

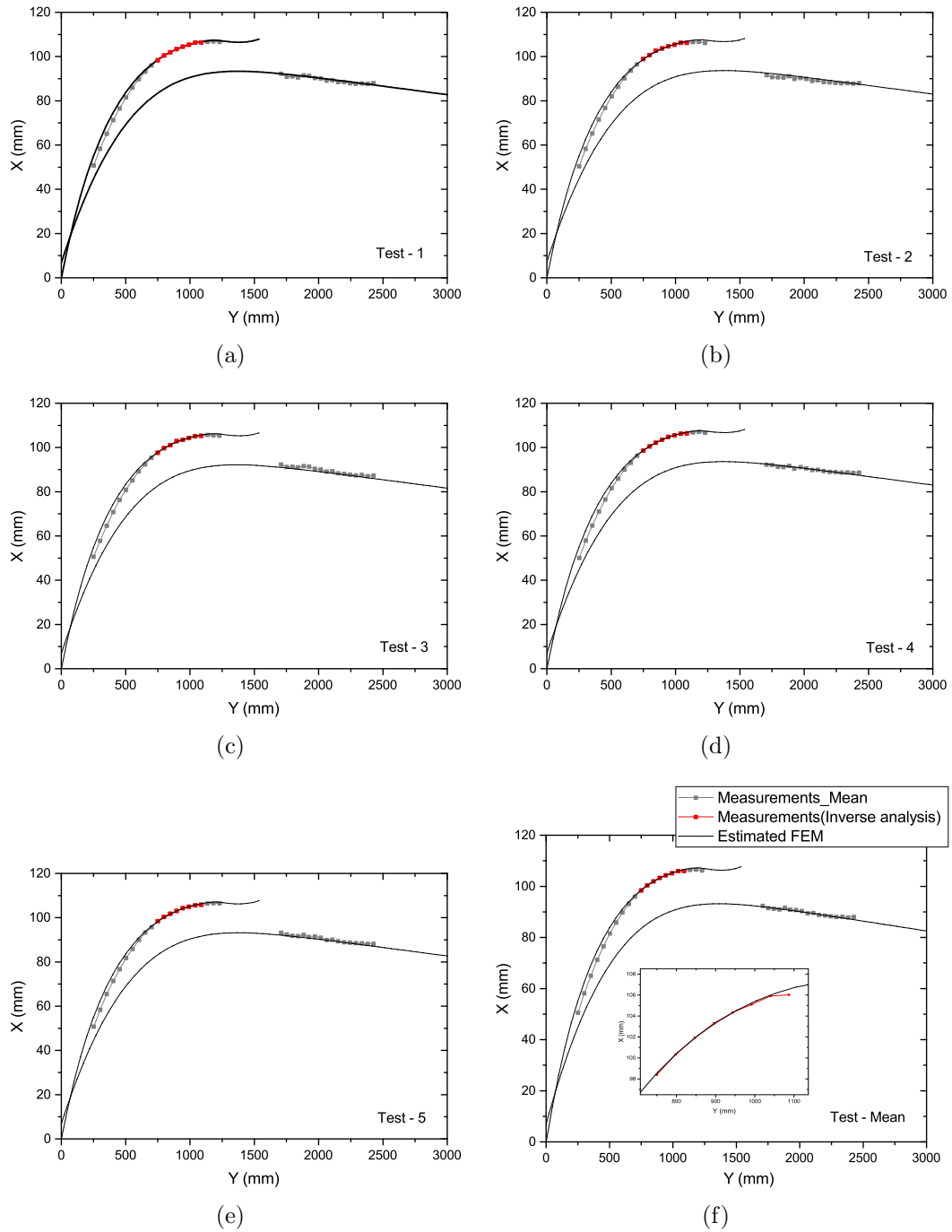


Figure 5.14: Configurations of riser and bend stiffener of measurements and FEM model for five tests and mean data.

5.4.4 Riser curvature distribution

After the configuration of riser/bend stiffener system is obtained, the curvature distributions of riser and bend stiffener can be calculated for the bending-tension test. The plane curve of bend stiffener configuration can be represented by an interpolated function $y = f(x)$. The curvature at a point (x, y) can be expressed in terms of the first and second derivatives of the function $f(x)$,

$$\kappa = \frac{f''(x)}{[1 + (f'(x))^2]^{3/2}}. \quad (5.8)$$

The curvature of the riser is directly output from the FEM model by beam element analysis. The curvature distribution of the bend stiffener is numerically calculated by post-processing the bend stiffener configuration curve data. Figure 5.15 shows the curvature distributions of the riser and bend stiffener calculated from FEM model and optical configuration measurements for Test 1. A interpolation of 3 order is used with the configuration data for the curvature calculation of bend stiffener in FEM model. For the optical configuration measurements on the riser and bend stiffener axes, a cubic function is applied to fit the measurements firstly, and then calculate curvature based on the fitted function. There is significant difference between the riser and bend stiffener curvatures along the arc length. The riser bends inside of the bend stiffener with a lower curvature distribution.

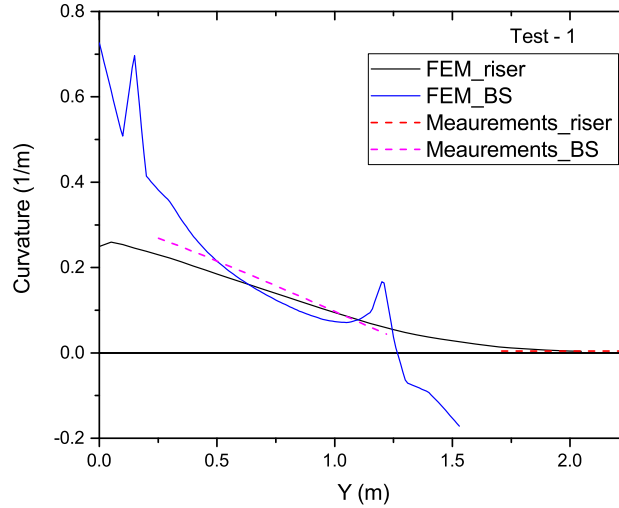


Figure 5.15: Curvature distributions of riser and bend stiffener.

5.5 Conclusions

A full-scale bending-tension test of riser/bend stiffener system is presented for a given loading conditions with five sets of repeated tests. The configurations of the

riser/bend stiffener sample are measured by a proposed optical image-based technique. The photoluminescent color targets are placed in the riser and bend stiffener regions of interest, which are tracked by the image digitization system and followed by image process and analysis. After data synchronization and analysis, five configurations of the riser/bend stiffener targets are obtained for the repeated tests. A finite element model is developed to represent the riser/bend stiffener bending-tension test with the top tension applied in the translator element and the rotation angle employed in a reference point representing the bending table center, and the ends of riser and bend stiffener in the same side both rigidly connected to the reference point. Mesh convergence analysis shows that the 0.05 m mesh is adequate for the present problem. An inverse analysis using Levenberg-Marquardt approach is applied in the riser/bend stiffener system with a direct finite element model and optical configuration measurements to simultaneously estimate loading condition and material parameters. A preliminary analysis of the parameter estimation methodology for the riser/bend stiffener bending-tension system is employed by the simulated measurements with 8 noise levels from the finite element model with exact parameters. Finally, the obtained five sets of experimental configuration measurements of 8 targets are applied to estimate: i) the unknown material response and ii) simultaneous tension and material parameters in the riser/bend stiffener system. The following conclusions are obtained:

- i). The precision of parameter estimation is strongly affected by the level of experimental errors in the measured configuration data. If there is no experimental error, the tension and material properties can be estimated with very high precision. If 1% or larger random experimental errors are present, the estimated parameters deviate significantly from the exact values.
- ii). There are only slight differences between the material properties estimated by using the two hyperelastic models for polyurethane, as the estimated strain-stress curve by the first order Polynomial hyperelastic model presents highly linear elastic behavior. Nonetheless, the nonlinear elastic model yielded estimated strain-stress curves with smaller variations between repeated estimations.
- iii). When estimating simultaneously the top tension and two material property parameters, the constraint on the range of the top tension improves significantly the precision of the estimation of the top tension force over the unconstrained simultaneous estimation of the three parameters. There are very small variations between repeated estimated forces obtained by the constrained estimation approach, which indicates that the proposed inverse analysis methodology

with constrained top tension is reliable for the estimation of the tension and material parameters in the riser/bend stiffener top system.

- iv). The riser bends inside of the bend stiffener with a smaller curvature distribution, as shown by the curvature distributions of the riser and bend stiffener calculated using the estimated parameters in the riser/bend stiffener system.

Chapter 6

Conclusion and Suggestions

This thesis has mainly worked on the modeling and parameter estimation in flexible riser-bend stiffener top connection, which allows a more realistic analysis of the riser top response and can help reducing the lifetime (re)assessment uncertainties. The original contributions, main conclusions and suggestions for future work are presented in this chapter.

6.1 Main original contributions

The main original contributions in this thesis are summarized as follows:

1. A large deflection beam model was developed to represent the riser-bend stiffener top connection with I-tube interface, considering that the bellmouth transition area with the polymeric sleeve is represented by a straight rigid surface followed by a curved section. The beam model incorporates the riser bilinear bending behavior and bend stiffener polyurethane nonlinear elastic symmetric response.
2. Three systems of coupled differential equations for the riser-bend stiffener top connection with I-tube interface combined with the corresponding multipoint boundary conditions were presented. And the obtained multipoint boundary value problem of riser top connection were numerically solved by an proposed iterative procedure.
3. A monitoring approach has been proposed aiming at decreasing the uncertainties associated to bend stiffener mechanical response and the effective top tension employed for further flexible riser lifetime (re)assessment. It is composed of gyrometers installed along bend stiffener/riser length and combined with an inverse problem methodology based on the Levenberg-Marquardt algorithm and a direct analytical model of riser/bend stiffener.

4. A full-scale bending-tension test of the riser/bend stiffener system were presented. An image-based experimental monitoring technique was employed in the bending-tension test to measure the sample configurations, which consists of the image acquisition, processing and analysis, and the data synchronization and analysis.
5. An inverse analysis using Levenberg-Marquardt algorithm was applied in the full-scale bending-tension test of riser/bend stiffener system with a direct finite element model and optical configuration measurements to simultaneously estimate measured tension and unknown material parameters. The curvature distribution of riser was then calculated by the finite element model with the estimated modeling parameters.

The analytical model of the riser-bend stiffener top connection with I-tube interface allows a more realistic assessment of the flexible riser top connection response, contributing to a better understanding of the complex riser interaction with the bend stiffener and I-tube, which can also be employed for preliminary design. The proposed monitoring approach combined with inverse problem methodology can effectively reduce flexible riser lifetime (re)assessment uncertainties. For the riser/bend stiffener bending-tension test with optical configuration measurements, the riser curvature distribution inside of bend stiffener can be calculated in the finite element model after the estimations of polyurethane material parameters. Simultaneous parameter estimation of loading condition and material parameters in the riser/bend stiffener bending-tension test is aimed at providing a feasibility evidence to the field application.

6.2 Main conclusions

The riser-bend stiffener top connection with I-tube interface was analyzed by a large deflection analytical beam bending model. The I-tube bellmouth transition region was considered with a straight rigid surface followed by a curved section. The riser follows a nonlinear bending behavior described by a bilinear moment vs curvature function and the bend stiffener polyurethane material exhibits nonlinear elastic symmetric response represented by a power law function. It was assumed that there is no gap between the riser and the bend stiffener and the riser is fixed in the end-fitting position. The mathematical formulation of the statically indeterminate system results in three systems of coupled differential equations combined with the corresponding multipoint boundary conditions to be numerically solved by an iterative procedure. A case study was carried out with a 7" flexible riser protected by a bend stiffener connected to an inclined I-tube bellmouth. The system is

subjected to extreme loading conditions and the influence of the sleeve shape and I-tube length on the riser curvature distribution, including the end-fitting position, and contact forces between the riser/sleeve and riser/bend stiffener sections were assessed. The following conclusions were obtained:

- The curvature distribution in the bend stiffener region is not affected by the sleeve geometry;
- The end-fitting curvature is affected by both parameters, where, i) as the sleeve radius R_{AB} increases, the initial curvature k_0 decreases and, ii) as the I-tube length L_1 is increased, the initial curvature decreases;
- The sleeve radius not only controls the initial contact angle and curvature distribution in the contact region, but also that, below a given radius, the riser does not interact with the curved section but directly contact the straight sleeve region, which leads to a peak in the riser curvature;
- The contact force between the riser and the sleeve is highly affected by its radius but is not influenced by the I-tube length.

The proposed monitoring approach composed by gyrometers installed along flexible riser/bend stiffener system length combined with an inverse problem methodology has been numerically investigated to estimate the polyurethane hyperelastic response and effective top tension. The riser/bend stiffener system was modeled using a large deflection beam bending model and the parameters were estimated using a damped least-square minimization approach with the Levenberg-Marquardt algorithm. For the preliminary feasibility investigation, the gyrometer experimental data was numerically estimated through Monte Carlo simulations. A case study was carried out to investigate the influences of the number of sensors, sensors arrangement, loading conditions and top connection model on the inverse parameter estimations, leading to the following main conclusions:

- The selection of a top connection model to represent the riser/bend stiffener system is an important aspect of the proposed methodology and should represent the actual response as accurately as possible;
- The sensor arrangement directly affects the inverse parameter estimation and the sensitivity matrix may be employed to qualitatively support its positioning along system length;
- The methodology accuracy decreases for small top connection tip angles. Two approaches can be adopted for improvement: a) increase the number of sensors or b) decrease the number of unknowns;

- The number of unknowns may be decreased by calculating the material parameters in a short period, where the largest operational loading conditions are expected, followed by long term continuous effective top tension calculation at milder conditions.

A riser/bend stiffener system bending test was conducted with unknown polyurethane material parameters. During the bending test, the configuration of riser/bend stiffener sample was measured by a proposed optical image-based technique. A finite element model was developed to represent the riser/bend stiffener bending test. The inverse problem analysis using Levenberg-Marquardt approach has been applied in the riser/bend stiffener bending test system with a direct finite element model and optical configuration measurements to simultaneously estimate loading condition and material parameters. A preliminary analysis of the parameter estimation methodology for the riser/bend stiffener bending-tension system is employed by the simulated measurements with 8 noise levels from the finite element model with exact parameters. Finally, the obtained five sets of experimental configuration measurements of 8 targets are applied to estimate: i) the unknown material response and ii) simultaneous tension and material parameters in the riser/bend stiffener system. The following conclusions are obtained:

- The precision of parameter estimation is strongly affected by the level of experimental errors in the measured configuration data. If there is no experimental error, the tension and material properties can be estimated with very high precision. If 1% or larger random experimental errors are present, the estimated parameters deviate significantly from the exact values;
- There are only slight differences between the material properties estimated by using the two hyperelastic models for polyurethane, as the estimated strain-stress curve by the first order Polynomial hyperelastic model presents highly linear elastic behavior. Nonetheless, the nonlinear elastic model yielded estimated strain-stress curves with smaller variations between repeated estimations;
- When estimating simultaneously the top tension and two material property parameters, the constraint on the range of the top tension improves significantly the precision of the estimation of the top tension force over the unconstrained simultaneous estimation of the three parameters. There are very small variations between repeated estimated forces obtained by the constrained estimation approach, which indicates that the proposed inverse analysis methodology with constrained top tension is reliable for the estimation of the tension and material parameters in the riser/bend stiffener system;

- The riser bends inside of the bend stiffener with a smaller curvature distribution, as shown by the curvature distributions of the riser and bend stiffener calculated using the estimated parameters in the riser/bend stiffener system.

6.3 Suggestions for Future work

Some suggestions for future work are as follows:

- i). The experimental uncertainties of optical measurements should be studied in detail, and the actual noise level of the measured data should be presented then;
- ii). The gyrometer may be installed along riser/bend stiffener sample in the laboratory bending test to measure the rotation angles instead of configurations. The parameter estimation based on the direct finite element model and measured rotation angles may be applied for the riser/bend stiffener system to verify the proposed gyrometer monitoring approach preliminarily;
- iii). The riser hysteresis behavior of nonlinear curvature and moment relationship may be estimated by the proposed inverse problem methodology in the riser/bend stiffener system with the measured configurations or rotation angles;
- iv). An inverse analysis to estimate the stochastic loading conditions with the field gyrometer rotation data may be implemented;
- v). The estimated top tension and curvature distribution may be used as input into a local cross-sectional analytical or numerical model to calculate the armour wire stresses. The fatigue lifetime (re)assessment may be then implemented by cycle counting the resulting irregular stress based on the Rainflow technique with an appropriate $S - N$ curve.

Bibliography

- [1] NEWPORT, A., HAHEIM, S., MARTINEAU, E. “Espirito Santo: Operational Feedback on the Use of Steel Risers on a Turret Moored FPSO”. In: *Offshore Technology Conference*, Houston, Texas, 2014. OTC-25354-MS.
- [2] API 17B. *Recommended practice for flexible pipe*. latest ed. Washington, American Petroleum Institute, 2014.
- [3] CLEVELARIO, J., SHELDRAKE, T., PIRES, F., FALCAO, G., SOUZA, I., AQUINO, F. “Flexible Riser Outer Sheath Full Scale Wearing Simulation and Evaluation”. In: *Offshore Technology Conference*, Houston, Texas, 2009. OTC-20099-MS.
- [4] MUREN, J., EIDE, J., ENGELBRETH, K. I., CHRISTENSEN, H., NILSEN-AAS, C. “Lifetime Extension of Flexible Risers Based On Field Experiences”. In: *Offshore Technology Conference*, Houston, Texas, 2016. OTC-26998-MS.
- [5] TECHNIPFMC. *A broad range of flexible pipe systems with advanced integrated solutions*. In: Report, TechnipFMC, 2019. Disponível em: <<http://www.technipfmc.com>>.
- [6] AXELSSON, G., SKJERVE, H. “Flexible Riser Carcass Collapse Analyses: Sensitivity on Radial Gaps and Bending”. In: *Proceedings of the 33th International Conference on Offshore Mechanics and Arctic Engineering*, v. 6A, New York, 2014. OMAE2014-23922.
- [7] SECHER, P., BECTARTE, F., FELIX-HENRY, A. “Lateral Buckling of Armor Wires in Flexible Pipes: Reaching 3000m Water Depth”. In: *Proceedings of the 30th International Conference on Offshore Mechanics and Arctic Engineering*, v. 4, pp. 421–428, New York, 2011. American Society of Mechanical Engineers. OMAE2011-49447.
- [8] MARINHO, M. G., CAMERINI, C. S., SANTOS, J. M., PIRES, G. P. “Surface monitoring techniques for a continuous flexible riser integrity assessment”.

- In: *Offshore Technology Conference*, Houston, Texas, 2007. OTC-18946-MS.
- [9] SIMONSEN, A. *Inspection and Monitoring Techniques for Un-bonded Flexible Risers and Pipelines*. MS dissertation, University of Stavanger, Norway, 2014.
- [10] ZHU, L., TAN, Z. “End Fitting Effect on Tensile Armor Stress Evaluation in Bent Flexible Pipe”. In: *Proceedings of the 33th International Conference on Offshore Mechanics and Arctic Engineering*, v. 6A, New York, 2014. OMAE2014-23928.
- [11] MIYAZAKI, M. N. R., DE SOUSA, J. R. M., ELLWANGER, G. B. “A Three-dimensional FE Approach for Stress Analysis of Tensile Armor inside End Fittings”. In: *Proceedings of the 38th International Conference on Offshore Mechanics and Arctic Engineering*, New York, 2019. MAE2019-95506.
- [12] FROMAGE, L., FOURNIER, J.-R., RAND ALWYN MCLEARY, P. D. “From Schiehallion to Quad 204 FPSO; Turret Mooring System experience and enhancements.” In: *Society of Petroleum Engineers*, Aberdeen, UK, 2013. SPE-166560-MS.
- [13] LONGO, C., NETO, S., PAULA, M., LOPES, F., GODINHO, C. “Albacora Leste Field - Subsea Production System Development”. In: *Offshore Technology Conference*, Houston, Texas, 2006. OTC-18044-MS.
- [14] API 17L1. *Specification for flexible pipe ancillary equipment*. latest ed. Washington, American Petroleum Institute, 2014.
- [15] API 17L2. *Recommended practice for flexible pipe ancillary components*. latest ed. Washington, American Petroleum Institute, 2014.
- [16] VAZ, M. A., LEMOS, C. A. D., CAIRE, M. “A non-linear analysis formulation for bend stiffeners”, *Journal of Ship Research*, v. 51, n. 3, pp. 250–258, 2007.
- [17] HE, Y., CAIRE, M., VAZ, M. “An inverse problem methodology for multiple parameter estimation in bend stiffeners”, *Applied Ocean Research*, v. 83, pp. 37–47, 2019.
- [18] CAIRE, M., VAZ, M., COSTA, M. “Bend stiffener nonlinear viscoelastic time domain formulation”, *Marine Structures*, v. 49, pp. 206 – 223, 2016.

- [19] CAIRE, M., VAZ, M. A. “A nonlinear viscoelastic bend stiffener steady-state formulation”, *Applied Ocean Research*, v. 66, pp. 32–45, 2017.
- [20] SOUSA, J. R. M., SOUSA, F. J. M., DE SIQUEIRA, M. Q., SAGRILO, L. V. S., DE LEMOS, C. A. D. “A Theoretical Approach to Predict the Fatigue Life of Flexible Pipes”, *Journal of Applied Mathematics*, v. 2012, 2012.
- [21] API 17J. *Specifications for unbonded flexible pipe*. latest ed. Washington, American Petroleum Institute, 2014.
- [22] DNV-OS-F201. *Dynamic Risers*. Det Norske Veritas, 2010.
- [23] SMITH, R. “Bending stiffeners for extreme and fatigue loading of unbonded flexible risers”. In: *Proceedings of the 27th International Conference on Offshore Mechanics and Arctic Engineering*, v. 3, pp. 405–413, New York, 2008. American Society of Mechanical Engineers. OMAE2008-57464.
- [24] BOEF, W., OUT, J. “Analysis of a flexible riser top connection with bend restrictor”. In: *Offshore Technology Conference*, pp. 131–142, Houston, Texas, 1990. OTC-6436-MS.
- [25] LANE, M., MCNAMARA, J., GIBSON, R., TYRER, A. “Bend stiffeners for flexible risers”. In: *Offshore Technology Conference*, Houston, Texas, 1995. OTC-7730-MS.
- [26] CAIRE, M., VAZ, M., LEMOS, C. “The effect of flexible pipe non-linear bending stiffness behavior on bend stiffener analysis”. In: *Proceedings of the 26th International Conference on Offshore Mechanics and Arctic Engineering*, v. 3, pp. 103–109, New York, 2007. American Society of Mechanical Engineers. OMAE2007-29108.
- [27] TANAKA, R., SILVEIRA, L., NOVAES, J., BARROS, E., MARTINS, C. “Bending Stiffener Design Through Structural Optimization”. In: *Proceedings of the 28th International Conference on Offshore Mechanics and Arctic Engineering*, v. 3, pp. 411–418, New York, 2009. American Society of Mechanical Engineers. OMAE2009-79505.
- [28] SODAHL, N., OTTESEN, T. “Bend stiffener design for umbilicals”. In: *Proceedings of the 30th International Conference on Offshore Mechanics and Arctic Engineering*, v. 4, pp. 449–460, New York, 2011. American Society of Mechanical Engineers. OMAE2011-49461.

- [29] DROBYSHEVSKI, Y. “Investigation into non-linear bending of elastic bars with application to design of bend stiffeners”, *Marine Structures*, v. 31, pp. 102–130, 2013.
- [30] MENICONI, L., LOPES, T. “Fatigue analysis of bend stiffeners”. In: *Proceedings of the 20th International Conference on Offshore Mechanics and Arctic Engineering*, v. 3, New York, 2001. American Society of Mechanical Engineers.
- [31] DEMANZE, F., HANONGE, D., CHALUMEAU, A., LECLERC, O. “Fatigue life analysis of polyurethane bending stiffeners”. In: *Proceedings of the 24th International Conference on Offshore Mechanics and Arctic Engineering*, v. 3, pp. 261–267, New York, 2005. American Society of Mechanical Engineers. OMAE2005-67506.
- [32] PERDRIZET, T., LEROY, J., BARBIN, N., LE-CORRE, V., CHARLIAC, D., ESTRIER, P. “Stresses in armour layers of flexible pipes: comparison of Abaqus models”. In: *2011 SIMULIA Customer Conference*, Barcelona, Spain, 2011.
- [33] ELOSTA, H., GAVOUYERE, T., GARNIER, P. “Flexible risers lifetime extension: riser in-service monitoring and advanced analysis techniques”. In: *Proceedings of the 36th International Conference on Offshore Mechanics and Arctic Engineering*, v. 5A, New York, 2017. American Society of Mechanical Engineers. OMAE2017-62700.
- [34] ANDERSEN, M., BERG, A., SAEVIK, S. “Development of an optical monitoring system for flexible risers”. In: *Offshore Technology Conference*, Houston, Texas, 2001. OTC-13201-MS.
- [35] WEPPENAAR, N., KRISTIENSEN, M. “Present and future possibilities in optical condition monitoring of flexible pipes”. In: *Offshore Technology Conference*, Houston, Texas, 2008. OTC-19427-MS.
- [36] MORIKAWA, S. R. K., CAMERINI, C. S., BRAGA, A. M., LLERENA, R. A. “Real time continuous structural integrity monitoring of flexible risers with optical fiber sensorss”. In: *Offshore Technology Conference*, Houston, Texas, 2010. OTC-20863-MS.
- [37] MORIKAWA, S. R. K., BRAGA, A. M. B., CAMERINI, C. S., KATO, C. C., LLERENA, R. A., CAMERINI, M., SIMOES, T. B. “New advances in flexible riser monitoring techniques using optical fiber sensors”. In: *Proceedings of the 31th International Conference on Offshore Mechanics*

and *Arctic Engineering*, v. 3, pp. 793–798, New York, 2012. American Society of Mechanical Engineers. OMAE2012-83952.

- [38] GASPARETTO, V. *Method of evaluating the fatigue life of flexible risers by monitoring the tensile armor wires strain*. MS dissertation, Federal University of Rio de Janeiro, Rio de Janeiro, Brazil, 2017.
- [39] LYONS, G. J., VANDIVER, J. K., LARSEN, C. M., ASHCOMBE, G. T. “Vortex induced vibrations measured in service in the Foinaven dynamic umbilical, and lessons from prediction”, *Journal of Fluids and Structures*, v. 17, n. 8, pp. 1079–1094, 2003.
- [40] LYONS, G. J., BROWN, D. T., COOK, H. H., WALLS, B., BARNAY, G. “The foinaven umbilical performance monitoring system - a new approach”. In: *Offshore Technology Conference*, Houston, Texas, 1998. OTC-8883-MS.
- [41] TRARIEUX, F., LYONS, G. J., VAZ, M. A., PATEL, M. H., GARNHAM, S. “Investigation of the influence of waves and vessel motions on the VIV response of flexible risers and umbilicals from a fatigue damage perspective”. In: *Proceedings of the 25th International Conference on Offshore Mechanics and Arctic Engineering*, v. 4, pp. 475–486, New York, 2006. American Society of Mechanical Engineers. OMAE2006-92010.
- [42] ROBERTS, R., GARNHAM, S., D’ALL, B. “Fatigue monitoring of flexible risers using novel shape-sensing technology”. In: *Offshore Technology Conference*, Houston, Texas, 2007. OTC-19051-MS.
- [43] 4SUBSEA. *Wireless access to accelerometer and gyroscope*. In: Report, 4subsea, 2017. Disponível em: <<http://www.4subsea.com>>.
- [44] 2H OFFSHORE. *Chevron Tahiti’s riser and flowline monitoring system was designed and supplied by 2H Offshore in 2009*. In: Report, 2H Offshore, 2009. Disponível em: <<https://2hoffshore.com/>>.
- [45] PULSE. *INTEGRIPod NXT - Next Generation Subsea Motion and Data Logging Sensor Platform*. In: Report, Pulse Structural Monitoring, 2019. Disponível em: <<https://www.pulse-monitoring.com/>>.
- [46] LEVENBERG, K. “A method for the solution of certain nonlinear problems in least-squares”, *Quarterly of Applied Mathematics*, v. 2, pp. 164–168, 1944.

- [47] MARQUARDT, D. W. “An algorithm for least-squares estimation of nonlinear parameters”, *Journal of the Society for Industrial and Applied Mathematics*, v. 11, n. 2, pp. 431–441, 1963.
- [48] BECK, J. V., ARNOLD, K. J. *Parameter Estimation in Engineering and Science*. New York, Wiley, 1977.
- [49] OZISIK, M., ORLANDE, H. *Inverse heat transfer: fundamentals and applications*. New York, Taylor Francis, 2000.
- [50] MOLIMARD, J., RICHE, R., VAUTRIN, A., LEE, J. R. “Identification of the four orthotropic plate stiffnesses using a single open-hole tensile test”, *Experimental Mechanics*, v. 45, n. 5, pp. 404–411, out. 2005.
- [51] FU, G., GU, J., LOURENCO, M. I., DUAN, M., ESTEFEN, S. F. “Parameter determination of double-ellipsoidal heat source model and its application in the multi-pass welding process”, *Ships and Offshore Structures*, v. 10, n. 2, pp. 204–217, 2015.
- [52] SEON, G., MAKEEV, A., CLINE, J., SHONKWILER, B. “Assessing 3D shear stress-strain properties of composites using Digital Image Correlation and finite element analysis based optimization”, *Composites Science and Technology*, v. 117, pp. 371–378, set. 2015.
- [53] HUANG, L. X., YANG, M., ZHOU, X. J., YAO, Q., WANG, L. “Material parameter identification in functionally graded structures using isoparametric graded finite element model”, *Science and Engineering of Composite Materials*, v. 23, n. 6, pp. 685–698, nov. 2016.
- [54] KAZEMI, Z., HEMATIYAN, M., SHIAH, Y. “Load identification for viscoplastic materials with some unknown material parameters”, *International Journal of Mechanical Sciences*, v. 153–154, pp. 164–177, 2019.
- [55] TAN, Z., QUIGGIN, P., SHELDRAKE, T. “Time Domain Simulation of the 3D Bending Hysteresis Behaviour of an Unbonded Flexible Riser”. In: *Proceedings of the 26th International Conference on Offshore Mechanics and Arctic Engineering*, v. 3, New York, 2007. OMAE2007-29315.
- [56] SAEVIK, S. “Theoretical and experimental studies of stresses in flexible pipes”, *Computers and Structures*, v. 89, pp. 2273–2291, 2011.
- [57] SOUSA, J. R. M., MAGLUTA, C., ROITMAN, N., CAMPELLO, G. C. “Bending Analysis of a Flexible Pipe With Broken Tensile Armor Wires”. In:

Proceedings of the 34th International Conference on Offshore Mechanics and Arctic Engineering, v. 5A, New York, 2015. OMAE2015-41436.

- [58] LEROY, J., PERDRIZET, T., CORRE, V., ESTRIER, P. “Stress Assessment in Armour Layers of Flexible Risers”. In: *Proceedings of the 29th International Conference on Offshore Mechanics and Arctic Engineering*, v. 5AB, New York, 2010. OMAE2010-20932.
- [59] LEROY, J., ESTRIER, P. “Calculation of Stresses and Slips in Helical Layers of Dynamically Bent Flexible Pipes”, *Oil and Gas Science and Technology Rev. IFP*, v. 59, n. 6, pp. 545–554, 2001.
- [60] RAMESH, C. J., RANGACHER, K., BRIAN, G. S. *Machine Vision*. McGraw-Hill Education, 1995.
- [61] SIRISHA, K., SELOKAR, N., SAINI, M., PALTA, P., MANIK, R., CHAUHAN, M., SINGLA, S. “Cryopreservation of Zona-Free Cloned Buffalo (*Bubalus Bubalis*) Embryos: Slow Freezing vs Open-Pulled Straw Vitrification”, *Reproduction in Domestic Animals*, v. 48, pp. 538–544, 2013.
- [62] ZHANG, Y. “A survey on evaluation methods for image segmentation”, *Pattern Recognition*, v. 29, n. 8, pp. 538–544, 1996.
- [63] GROVE, C., JERRAM, D. A. “jPOR: An ImageJ macro to quantify total optical porosity from blue-stained thin sections”, *Computers Geosciences*, v. 37, n. 11, pp. 1850–1859, 2011.
- [64] HERNÁNDEZ, I. D., HERNÁNDEZ-FONTES, J. V., VITOLA, M. A., SILVA, M. C., ESPERANÇA, P. T. “Water elevation measurements using binary image analysis for 2D hydrodynamic experiments”, *Ocean Engineering*, v. 157, pp. 1335–1346, 2018.
- [65] OPENCV. *Camera calibration - opencv 3 documentation*. In: Report, OpenCV, 2019. Disponível em: <https://docs.opencv.org/3.0-beta/doc/py_tutorials/py_calib3d/py_calibration/py_calibration.html>.
- [66] IMAGEJ. *ImageJ-An open platform for scientific image analysis*. 2019. Disponível em: <<https://imagej.net/Welcome>>.
- [67] HERNÁNDEZ, I. D., VAZ, M. A., CYRINO, J. C. R., ALVAREZ, N. M. R. “Three-dimensional image-based approach for imperfect structures surface modeling”, *Journal of the Brazilian Society of Mechanical Sciences and Engineering*, v. 41, n. 371, pp. 1–21, 2019.

- [68] WOLFRAM RESEARCH. *Wolfram Mathematica*. 10.0 ed. Champaign, Illinois, Wolfram, 2015.
- [69] HE, Y., LU, H., VAZ, M., CAIRE, M. “Flexible riser top connection analysis with I-tube interface and bending hysteresis effect”. In: *Proceedings of the 38th International Conference on Offshore Mechanics and Arctic Engineering*, v. 4, New York, 2019. OMAE2019-95826.
- [70] DAVERN, A. M. *National Instruments*. In: Report, National Instruments, 2019. Disponível em: <<https://www.ni.com/en-us.html>>.
- [71] OTSU, N. “A Threshold Selection Method from Gray-Level Histograms”, *IEEE Transactions on Systems, Man, and Cybernetics*, v. 9, n. 1, pp. 62–66, jan. 1979.
- [72] HIBBIT, D., KARLSSON, B., SORENSEN, P. *ABAQUS Theory Manual*. 6.14 ed. Providence, RI., ABAQUS, 2014.
- [73] VAN ROSSUM, G. *Python 3.7.4 documentation*. In: Report, Python, 2019. Disponível em: <<https://www.python.org/doc/>>.